FACULDADE DE ENGENHARIA DA UNIVERSIDADE DO PORTO

Projeto de Up-Down Converter e Antena para Comunicações Wi-Fi Sub-Aquáticas

Project of an Up-Down Converter and Antenna for Underwater Wi-Fi Communications

José Ricardo Quaresma Reis Pereira

Master in Electrical and Computers Engineering

Supervisor: Professor Henrique Manuel de Castro Faria Salgado

July 27, 2018

Abstract

Radio-waves are strongly attenuated in the underwater environment. However, as the attenuation increases with frequency, the use of lower frequencies may allow to obtain higher range communications. The possibility of using commercial Wi-Fi cards is extremely attractive due to the low cost and due to its large compatibility with IP protocol, allowing the use of Internet in an underwater environment. There are several scenarios of application, some of which stand out the environmental monitoring and aquaculture surveillance, sea ports as well as the oil, gas and raw materials industry.

This work concerns the development of an up-down converter system and an antenna that allows the use of commercial Wi-Fi cards in an underwater communication with higher ranges. The system developed downconverts the RF signal from the Wi-Fi card ($\sim$ 2.4GHz) to an IF frequency of around 100MHz. This signal is the one that propagates through the underwater medium. On the receiver side, this signal is upconverted to the Wi-Fi band again and the communication is established in this way. The circuit design uses an oscillator/PLL, a mixer, and it includes a chain of amplification with automatic switching. The project includes the specification and design of the PCB to be implemented in a real-case use.

Keywords: Antenna Design, Printed Circuit Board Design, RF Design, Underwater Communications, Wi-Fi.

Acknowledgments

Este longo caminho só foi possível com o apoio, a energia e a força de várias pessoas, às quais, mesmo correndo o risco de cometer alguma imperdoável omissão, não posso deixar de agradecer. Aproveito então para agradecer

ao Professor Doutor Henrique Salgado por todo o conhecimento que me transmitiu, por ter assumido a responsabilidade de orientar a minha tese de mestrado e por todo o apoio, motivação e confiança demonstrada.

ao Doutor Luís Pessoa pela disponibilidade e ajuda, tanto teórica como experimental, e pela confiança demonstrada pelo meu trabalho ao longo destes meses.

ao INESC TEC pela disponibilização dos recursos indispensáveis à realização deste trabalho de mestrado.

à FEUP por me ter ensinado tanto e por me ter proporcionado todos os meios para crescer profissionalmente.

à Unidade de Robótica e Sistemas Inteligentes (ROBIS) do INESC TEC no ISEP pela disponibilização das suas instalações para a realização de testes.

aos meus colegas de trabalho Diogo Moreira, Erick Lima, Fábio Pacheco, Hugo Santos, Joana Tavares, Oluyomi Aboderin pelo excelente ambiente de trabalho proporcionado, pelo conhecimento partilhado e pelas pausas para café e refeições que renovaram forças.

aos meus colegas de mestrado, em especial ao pessoal da Maratona das Tascas pela amizade, e por me terem feito sentir em casa.

aos meus amigos, que tão importantes são em tornar a minha vida mais animada e feliz.

a ti Joana, por toda a força que me deste e continuas a dar em ir mais longe, por seres a pessoa especial que és, e por me ensinares todos os dias a ser uma pessoa melhor.

a toda a minha família e sobretudo aos meus pais. Vocês que são os grandes pilares da minha vida, que pagaram a minha educação profissional, e me deram educação pessoal. A vocês, sem dúvida, dou o meu maior agradecimento.

"We explore because we are human, and we long to know"

Stephen Hawking

Contents

List of Figures

List of Tables

Abbreviations and Symbols

AC	*Alternating Current*
AUV	*Autonomous Underwater Vehicle*
balun	*Balanced-to-unbalanced*
CPWG	*Coplanar Waveguide with Lower Ground Plane*
DC	*Direct Current*
EM	*Electromagnetic*
EMC	*Electromagnetic Compatibility*
EMI	*Electromagnetic Interference*
ESR	*Equivalent Series Resistance*
EVM	*Error Vector Magnitude*
FEM	*Finite Element Method*
FSL	*Free Space Losses*
GB	*Gain Block*
IC	*Integrated Circuit Oscillator*
IF	*Intermediate Frequency*
IEEE	*Institute of Electrical and Electronics Engineer*
ISI	*Inter-Symbol Interference*
LDO	*Low Drop Out*
LNA	*Low Noise Amplifier*
LO	*Local Oscillator*
LoS	*Line of Sight*
Mbps	*Megabits per second*
OFDM	*Orthogonal Frequency-Division Multiplexing*
PAPR	*Peak-to-Average Power Ratio*
PCB	*Printed Circuit Board*
PLL	*Phase Locked Loop*
QAM	*Quadrature Amplitude Modulation*
RF	*Radio Frequency*
RMS	*Root Mean Square*
SMA	*SubMiniature version A*
SNR	*Signal-to-Noise Ratio*
SRF	*Self Resonant Frequency*
TCXO	*Temperature Compensated Crystal Oscillator*
TEM	*Transverse Electromagnetic*
VNA	*Vector Network Analyzer*

α	Attenuation constant
β	Phase constant (wavenumber)

γ	Propagation constant
ε	Permittivity
ε_0	Vacuum permittivity
ε_r	Relative permittivity
η	Intrinsic impedance
λ	Wavelength
μ	Permeability
μ_0	Vacuum permeability
μ_r	Relative permeability
σ	Conductivity
ω	Angular frequency
Z_{in}	Input impedance
Z_o	Characteristic impedance

Chapter 1

Introduction

Life underwater has attracted scientists' minds and dreamers' imagination for thousands of years. In 1572, Luis de Camões wrote his epic poetry *Os Lusíadas* about the way sea Gods were trying to prevent Portuguese armada to reach India. Three centuries later, Jules Verne in his masterpiece *Twenty Thousand Leagues Under the Sea*, wrote about the devil sea creature that lived in the deep blue sea attacking ships. The truth is, we still don't know many of the mysteries and richness that are hidden within those depths, waiting to be explored.

One of those richnesses, that is starting to enthusiasm researchers around the world, is the amount of raw materials that is laying in underwater mines. Despite the efforts to develop recycling technologies, European Union has a huge dependency on raw materials [3], spending around 30 billion dollars per year since 2005 importing them. In [3] it can be seen that metal ores has been the most traded product in this group and responsible for the largest trade deficit. These materials have a huge importance in EU's economy and in our lives as sectors like construction, chemicals, automotive, aerospace, machinery and equipment industry which have a combined value that exceeds 1 billion € and are responsible for the employment of more than 30 million people that depend on raw material [4]. They are also necessary to make almost everything we use in our daily life, like phones and computers that run our lives, science and evolution. Even the green technology that promises to reduce emissions and oil dependency has a huge need for materials, like tellurium for solar panels and lithium for electric vehicles batteries [5].

The trend is for an increase need for these materials, and since most of the land has been actively mined over the last centuries, most of its mineral deposits, especially the easy-to-access

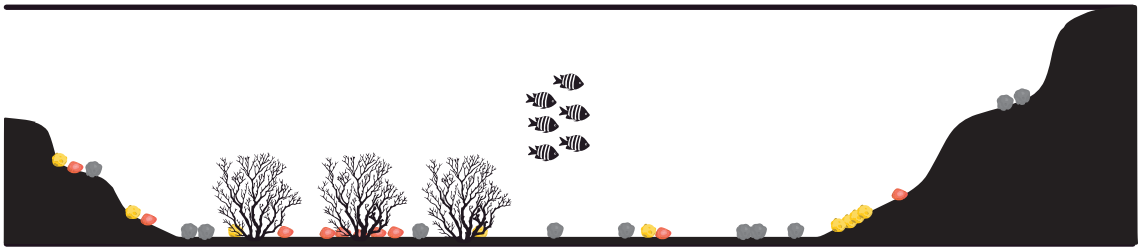

Figure 1.1: Illustration of the unexplored richness of underwater ground.

ones, are depleted. As an example, mining in Andes, that is responsible for 40% of the worlds supply in copper, would need to remove 50 tons of barren rock to get to a 20 million ton ore deposit with only 0.5% copper in it [5], while there are plenty copper deposits with higher percentage of copper sitting right on the seafloor. This progressive increase in money waste is making mining companies around the globe looking forward to search the untouched resources on the ocean floor, like copper, zinc, cobalt, manganese, titanium, gold and many other minerals [5]. Of course that this is also subject to a lot of controversy, people have a bad view of mining due to environmental harm and plausibly feel that this will also occur in water. So if this is a inevitable step, it has to be done in the right way.

1.1 Motivation

In order to explore and boost the innovation capacity of the raw materials sector, European Union has included this subject in Horizon 2020 programme in the section "Climate action, environment, resource efficiency and raw materials" and has launched project ¡VAMOS! to enable access to the high grade EU reserves of deeper seated minerals in a safe, clean and low visibility way. INESC TEC, Portugal, which has been doing research in this area in the last years, is part of the team that is leading this project and the subject of this thesis is in fact part of this project.

Figure 1.2: Partnership between INESC TEC and European Union project ¡VAMOS! .

¡VAMOS! is developing a novel solution based on robotic technologies to extract and pre-process ores found in underwater mines. This will help EU to safeguard access to important minerals and make EU back on the playing field in terms of trading this kind of materials. The project will also make sure that the solutions are environmentally, economically and socially acceptable. The project consists on the development of an underwater mining machine, with associated launch and recovery equipment, that is remotely controlled and supported by an assistance autonomous underwater vehicle (AUV) providing localized mapping and mining operations support [6].

One of the critical parts is then to create a solid and reliable underwater link with high bandwidth and low latency. This will enable a good communication with the mining machine that requires a safe distance communication (at least 5 meters), delicate and complex moves with low latency and the ability to transfer real-time video, among other requirements. One attractive way of establishing this communication link is by means of using commercial Wi-Fi cards, due to the low cost and the fact that they are largely compatible with the IP Protocol allowing the use of Internet in the underwater environment. The issue is that these cards operate at the traditional Wi-Fi bands and at these frequencies the attenuation is very high (Section 2.3). A way to overcome

this problem is by down-converting the signal from the Wi-Fi card to a lower frequency and up-converting again at the receiver side, enabling the communication to be establish at the traditional Wi-Fi channels even though the waves propagate through the medium at lower frequencies. This operation is done through an Up/Down Converter.

1.2 Objectives

The aim of this work is to design an underwater RF communication system that uses commercial Wi-Fi cards that operate at 2.4 GHz and improve their range of communication by using an up-down converter as illustrated in Figure 1.3. To accomplish these objectives, this work was divided in three parts.

The first part of this work is to measure the channel properties of both seawater and freshwater and design an antenna that operates in the frequency band of interest and has the right characteristics to operate in the underwater medium.

The second part of this work is to design an Up/Down Converter with a chain of amplification in the transmission and reception with automatic switching. The Up/Down Converter converts the signals that operate in the 2.4 GHz channels to the lower frequencies used by the antenna. This allows the communication to be established at longer distances and increase the robustness of the system. The Up/Down Converter must be reconfigurable in the sense that it should allow to select the desired frequency that best matches the transmission medium. As the system will be used in a real use-case, it must be compact and easy to use. This means that all the different modules of the Up/Down converter must be implemented in a single PCB, with only two port connectors: one for the antenna and another for the Wi-Fi card.

The third part is to integrate and validate the complete system, perform field measurements, and analyze the experimental results.

The success of this work demands a careful study of the state of art on RF design and an electromagnetic analysis on some of the modules of the overall system. This means that different software programs are required during this work: the design and simulation of the antenna is assisted by the software FEKO; the design and simulation of the PCB is assisted by the software ADS; and the implementation of the PCB will is performed in Altium Designer.

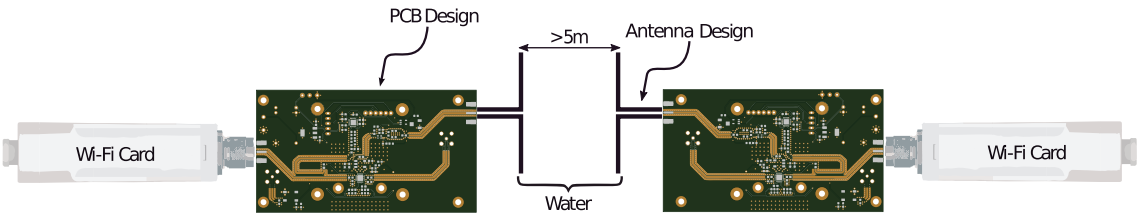

Figure 1.3: Illustration of the system to be implemented.

1.3 Structure of the Document

This report is divided in six chapters. In this first one an introduction to the topic is presented, including the description of the motivation and objectives of the work.

The second chapter presents the state of the art in this field of research. It includes a survey on underwater communications; an analysis on the electric properties of the water; the propagation models of the RF waves for water environment; and an analysis on the state of art of antennas and PCB design concerning the envisaged applications. Measurements techniques relevant for this work are also addressed in this chapter.

The third chapter presents the development and implementation of the antenna used to establish the underwater communication.

The fourth chapter starts with the proposed system level design of the Up/Down Converter board. Then, the design and implementation of the different individual blocks that are used in the final board are described. The chapter ends with the description and characterization of the designed Up/Down Converter.

The fifth chapter presents the system characterization and the results obtained in a real underwater medium. The chapter ends with a comparison between an old existing version of an Up-Down Converter for the same band and the one designed for this master's project.

Finally, the sixth chapter presents the summary and conclusions of the work performed, including suggestions for future work.

Chapter 2

State of Art

This chapter presents an introduction to the theme of this dissertation, which is underwater wireless communications. In the first section the different types of underwater communication systems are described. The second section presents the electrical properties of fresh water and salt water. The third section presents an analysis on the propagation models of electromagnetic waves for the underwater medium. The fourth section presents the literature review on antenna design, while the fifth section presents the literature review on RF Design. Finally, the sixth section presents the basic principles of operation of a mixer, which is the heart of the Up/Down Converter.

2.1 Underwater Wireless Communications

There are limitations on the use of physical connections in underwater communications, mostly because of the mobility and maneuverability of underwater operations. Thus, there is a high interest in underwater wireless communications. This section presents the most common methods of underwater wireless communication, referring their advantages and limitations.

2.1.1 Acoustic Communications

Underwater acoustic communications is the standard technology at this moment because it allows the longest range of communication, in the order of dozens of kilometers. The reason behind this long coverage distance lays on the relatively low attenuation of acoustic waves (information carriers) as they propagate through the underwater medium. In an acoustic communication, the information is contained in the differences in pressure propagating longitudinally through a medium. These mechanical waves reach a receiver that is capable of converting these pressure patterns to an electric current.

The velocity of propagation of the wave then depends on how fast the pressure wave propagates through the medium. The major characteristic that defines the average velocity of acoustic waves is the elasticity and density of the medium and can be measured by using Newton-Laplace Equation. That equation shows that a medium like water is more dense than air but much less compressible,

making the velocity of the sound in water near 1500 m/s which is more than four times the velocity of the sound in air.

But even though acoustic waves allow long distance communications and travel faster in water than in air, they still do it at an actual low velocity when compared with electromagnetic (EM) waves, making them unable to be used in some applications where a low latency is required.

Two other major limitations exist in acoustic waves: frequency dependent attenuation, and time varying multipath propagation. As the attenuation increases with frequency, this technology is generally not suitable for frequencies above 1 MHz meaning that it has a very limited bandwidth. On the other hand, the multipath phenomenon is aggravated by the fact that acoustic waves cannot perform smooth transitions through air/water interface [7] which leads to reflections. An illustration of this effect is shown in Figure 2.1. This phenomenon usually produces high delay spreads which can result in a inter-symbol interference (ISI) imposing a several limitation on the data-rate [8] [9].

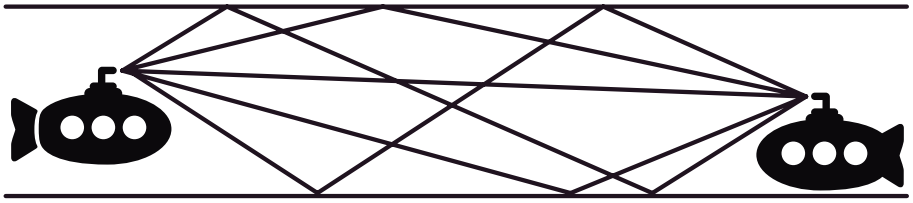

Figure 2.1: Illustration of the multipath effect in underwater acoustic systems.

So it is clear that, despite the good range characteristic of acoustic communications, the high latency and reduced bandwidth makes it unsuitable for high data rate communications.

2.1.2 Optical Communications

Underwater Optical wireless communications, on the other hand, has drawn a lot of attention from academia and researchers in the last years as they provide high data rates with low power consumption. The transmitter is usually a LED or a LD and transmits EM waves at very high frequencies, typically in the blue-green range of the visible spectrum where the attenuation is the lowest. Despite the very high frequencies, the attenuation in these waves is not as high as in the case of Radio Frequency waves because at theses frequencies the water behaves as a dielectric and not as a conductor [10].

Despite the good throughput that optical systems can offer, their carrier waves are highly affected by particles. The reason for this is that photons change direction when colliding with particles due to scattering which leads to a reduction in the intensity of the received signal; and dispersion [11, 10].

Optical waves then, only perform well in clear water, because otherwise the wave is affected by turbidity, particles and marine fouling. Moreover, a line of sight (LoS) and a tight alignment is required which is an extremely challenging task to accomplish in an underwater environment as illustrated in Figure 2.2. Another major phenomenon that reduces the intensity of the beam

is absorption. Usually it occurs due to inorganic material such as water molecules and dissolved salts, and also duo to organic substances like phytoplankton [12]. On top of that there is also a strong disturbance caused by the Sun causing noise to the communication.

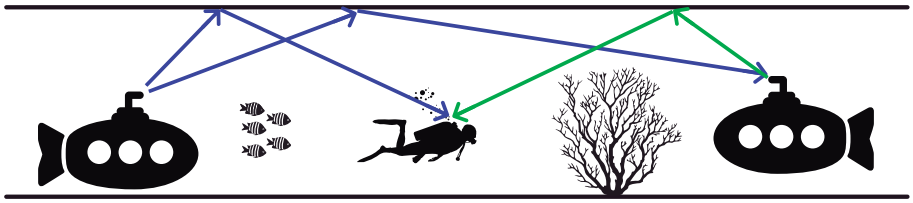

Figure 2.2: Illustration of some challenges in underwater optical systems.

It is possible to conclude that, despite optical communications being a good alternative to overcome acoustic limited bandwidth, it requires a high understanding of a very complex physio-chemical and biological system that is freshwater or seawater, and this leads to costly and complex systems to design that are more likely to fail under different harsh circumstances.

2.1.3 Radio Frequency Communications

Underwater EM wave communications has been pursued since the 1950s, where researchers were trying to use radio waves for the implementation of submarine communications. This idea was discarded because of the limited communication range due to the high conductivity in seawater [13]. More recently, due to the recent advances in electronics and antenna design, this technology has again being pursued since in specific underwater application scenarios it is advantageous to acoustic and optical.

Radio Frequency (RF) communications uses EM waves in the RF range as carriers of information. The velocity of RF waves in water is more than 4 orders of magnitude faster than acoustic waves, making the channel latency and Doppler effects greatly reduced, despite that the latter needs to be properly assessed [11]. Moreover, the use of the RF band gives this technology high bandwidths to operate and enable real time high data rate transfer (text, images and video) as seen in the optical case. These waves are also less sensitive to environment characteristics, such as ambient noise, turbidity, temperature changes and marine fouling, than acoustic and optical technologies. Also, there are no reports that this technology can harm marine life. This turns RF systems much more suitable and solid for applications like environmental monitoring and aquaculture surveillance, underwater mining systems (illustrated in Figure 2.3) as well as the oil and gas industry [7].

Another advantage of underwater RF communications is that the size of the antennas decreases in comparison to the ones that operate in air. This happens due the high permittivity of water as discussed later in Section 2.3.

The major limitation of this technology is the high attenuation due to the conductivity of water which turns it unsuitable for large communication distances. For example, seawater has a typical conductivity of 4 S/m which makes RF propagation to work poorly in this medium as

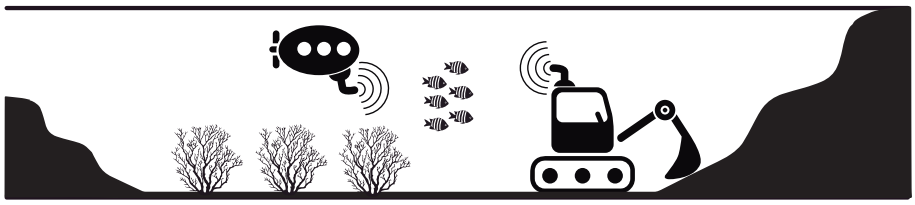

Figure 2.3: Illustration of an underwater RF system for mining applications.

demonstrated in [7, 14, 15, 16]). On the other hand, fresh water has a typical conductivity of only 0.01 S/m (around 400 times less than the typical conductivity of seawater) which means the EM wave propagation in fresh water is less attenuated than in seawater. In Section 2.3 a detailed analysis on how these parameters affect the propagation loss of EM waves will be discussed.

Thus, despite the advantages of RF systems on the application of interest, RF waves are heavily affected by propagation loss which places severe constraints on propagation distances and data rates. An understanding of the electric parameters of the water propagation models for underwater medium is essential to properly design underwater mobile systems with low power consumption.

2.1.4 Comparison of Underwater Communication Technologies

After a careful analysis on the different underwater wireless communication technologies, a summary about the benefits and limitations of each one is presented in Table 2.1.

Table 2.1: Comparison of underwater wireless communication technologies.

	Benefits	**Limitations**
RF	• High bandwidths. • Immune to acoustic noise. • Works in non-line-of-sight. • Unaffected by multi-path. • Unaffected by sediments and aeration.	• Dependency on frequency, conductivity and permittivity - low range
Optical	• Very high bandwidth. • Low cost and energy efficient.	• Requires a tight alignment of nodes. • Need a line-of-sight. • Subject to marine fouling, turbidity and particles - low range
Acoustic	• Very high range. • Low cost.	• Very limited bandwidth. • Impact on marine life • Latency in communications • Susceptible to channel gradients

2.2 Water Properties

The propagation of EM waves in water is different from that on air. The reason lays on the different electrical properties of water that have a negative impact on the signal propagation. In order to establish a accurate model for the propagation on this medium, these properties have to be discussed. In the next subsections, different water properties such as the conductivity, permittivity, permeability and finally the intrinsic impedance for both seawater and fresh water will be presented and discussed.

2.2.1 Conductivity

The conductivity of the medium highly affects the propagation of a signal. Media with no conductivity are known as isolators where there are no conduction electrons. As the conductivity of the medium increases, so does the attenuation the wave suffers [14]. Pure water has a very low conductivity, but water in general has dissolved ions that increases its conductivity.

Usually a conductivity of 4 S/m is used as a standard value for seawater [13, 17, 14] yet it changes with salinity and temperature. For instance, in the Red Sea the conductivity is 8 S/m whereas in the Artic it is only 2 S/m [15]. On the other hand, the conductivity of fresh water usually goes from 0.01 S/m to 0.05 S/m [14] the latter being the typical value used in simulations. The conductivity in fresh water is then near two orders lower than the conductivity in seawater.

2.2.2 Permittivity and Permeability

The permittivity of a medium describes its ability to resist an electric field. Usually media have a higher permittivity than vacuum and their value is represented as:

$$\epsilon = \epsilon_r \epsilon_0 \tag{2.1}$$

being ϵ_r the relative permittivity or dielectric constant of the medium, and ϵ_0 the electrical permittivity of free space.

At low frequencies the relative permittivity of seawater and freshwater is usually approximated to 81 S/m and 0.01 S/m [14] respectively. However, in a conductive medium its value is mathematically expressed as a complex quantity depending on factors such as temperature, salinity and frequency of the EM wave. In the literature there are some models that describe the complex relative permittivity of seawater and fresh water for some frequency bands. Debye model has proven to be a good model to describe this value for frequencies up to 100 GHz [18]. For example in [15] it is presented the variation of the real and imaginary parts of the relative permittivity of seawater with frequency at different temperatures using the Debye Model, while in [19] the Debye Model is used to describe the propagation loss of EM waves in fresh water.

Thus, to accurately describe the propagation of a wave on a conductive medium, a complex value of permittivity has to be considered. In Section 2.3 the Debye Model will be used to describe the propagation of EM in seawater and freshwater.

On the other hand the permeability of a medium is defined as the ability of that medium to store magnetic energy. As water is a non-magnetic medium, it has the same permeability as vacuum ($\mu_r = 1 \Rightarrow \mu = \mu_0$) and this value is valid for both seawater and fresh water [14, 17].

2.2.3 Intrinsic Impedance

The intrinsic impedance of a medium describes the ratio between electric field strength (**E**) and magnetic field strength (**H**). For a transverse-electric-magnetic (TEM) wave traveling through a homogeneous medium, the wave impedance is everywhere equal to the intrinsic impedance of the medium and its value is given by [14]:

$$\eta = \frac{\mathbf{E}}{\mathbf{H}} = \sqrt{\frac{j\omega\mu}{\sigma + j\omega\,\epsilon}} \tag{2.2}$$

where ω is the angular frequency, μ is the permeability, σ is the conductivity, and ϵ is the permittivity.

The intrinsic impedance of air is approximately the same as vacuum which is $120\pi\ \Omega$. On the other hand, as demonstrated before, for the water medium the permittivity is a complex value which makes the intrinsic impedance complex-valued also. This means that the electric and magnetic fields of a TEM wave propagate through the medium with a phase difference. In [15] it is presented the phase and magnitude of the intrinsic impedance of seawater for frequencies up to 10 GHz, showing that the magnitude of the intrinsic impedance is relatively small when compared to the intrinsic impedance of air (by a factor of about 1/9). In [19] it is presented the transmission loss for freshwater for frequencies up to 1 GHz. It is worth to say that these papers use the Debye Model to present their results, and that the parameters they use are valid for specific values of temperature, salinity and frequency.

2.3 Propagation Models for the Underwater Medium

Accurate and reliable channel characterization is critical for a proper implementation of any wireless communication system as it provides important information about the operating mode and capacity of that system. On underwater systems, this characterization is even more critical as the nature of this medium provides extra challenges as showed in Section 2.1. Despite several works concerning wireless communications over the air, there is no direct relation between water environment and the air environment as showed in Section 2.2. In this chapter a detailed model on RF propagation in seawater and freshwater is discussed.

Going through Maxweel Equations we get the homogeneous wave equations for $\widetilde{\mathrm{E}}$ and $\widetilde{\mathrm{H}}$ [14],

$$\nabla^2\widetilde{\mathrm{E}} - \gamma^2\widetilde{\mathrm{E}} = 0 \tag{2.3}$$

$$\nabla^2\widetilde{\mathrm{H}} - \gamma^2\widetilde{\mathrm{H}} = 0 \tag{2.4}$$

with

$$\gamma^2 = -\omega^2 \mu \, \epsilon_c \tag{2.5}$$

In Section 2.2.2 it was demonstrated that permittivity of water is complex valued and depends on factors such as temperature, salinity and frequency of the EM wave. This dependency is mathematically modeled using a complex relative permittivity given by

$$\epsilon_c \, (f) = \epsilon_0 \epsilon_r \, (f) = \epsilon_0 \, (\, \epsilon_r^{'} - j \, \epsilon_r^{''}) \tag{2.6}$$

Equation 2.5 then becomes

$$\gamma^2 = -\omega^2 \mu \;\; \epsilon_0 \, (\, \epsilon_r^{'} - j \, \epsilon_r^{''}) \tag{2.7}$$

Since γ is complex-valued, it can be written has

$$\gamma = \alpha + j\beta \tag{2.8}$$

where α is attenuation coefficient of the medium and β is the phase constant. Replacing equation 2.8 in equation 2.7 and going through the math the two following solutions for α and β are found,

$$\alpha = \omega \left\{ \frac{\mu \, \epsilon_r^{'} \epsilon_0}{2} \left[\sqrt{1 + \left(\frac{\epsilon_r^{''}}{\epsilon_r^{'}} \right)^2} - 1 \right] \right\}^{1/2} \text{Np/m} \tag{2.9}$$

$$\beta = \omega \left\{ \frac{\mu \, \epsilon_r^{'} \epsilon_0}{2} \left[\sqrt{1 + \left(\frac{\epsilon_r^{''}}{\epsilon_r^{'}} \right)^2} + 1 \right] \right\}^{1/2} \text{rad/m} \tag{2.10}$$

In literature there are a few models that describe the complex relative permittivity. One that has proven to be very accurate is Debye's model and it is described by [20],

$$\epsilon_r \, (f) = \epsilon_\infty + \frac{\epsilon_s - \epsilon_\infty}{1 + j2\pi f \tau} - j \frac{\sigma}{2\pi f \, \epsilon_0} = \epsilon_r^{'} - j \, \epsilon_r^{''} \tag{2.11}$$

where ϵ_s and ϵ_∞ are the real relative permittivity at low and high frequencies, respectively, f is the frequency of the EM wave, τ is the relaxation time (the time taken by water molecules to return to their random distribution when the oscillating electric field is removed), σ is the conductivity of water and ϵ_0 is the dielectric permittivity of free space. While ϵ_∞ can be considered constant and equal to 4.9 [20], parameters like ϵ_s, τ and σ depend on temperature and salinity of water. In [20] an accurate model is presented for these parameters. It is demonstrated that ϵ_s can be written as

$$\epsilon_s \, (T, S) = \epsilon_s \, (T) a(S, T) \tag{2.12}$$

with

$$\epsilon_s(T) = 87.134 - 1.949 \times 10^{-1} T - 1.276 \times 10^{-2} T^2 + 2.491 \times 10^{-4} T^3 \quad (2.13)$$

$$a(S,T) = 1.000 + 1.613 \times 10^{-5} ST - 3.656 \times 10^{-3} S + 3.210 \times 10^{-5} S^2 - 4.232 \times 10^{-7} S^3 \quad (2.14)$$

τ, it is also a function of temperature and salinity and is given by

$$\tau(T,S) = \tau(T,0) b(S,T) \quad (2.15)$$

with

$$\tau(T,0) = 1.768 \times 10^{-11} - 6.086 \times 10^{-13} T + 1.104 \times 10^{-14} T^2 - 8.111 \times 10^{-17} T^3 \quad (2.16)$$

$$b(s,T) = 1.000 + 2.282 \times 10^{-5} ST - 7.638 \times 10^{-4} S - 7.760 \times 10^{-6} S^2 + 1.105 \times 10^{-8} S^3 \quad (2.17)$$

After finding these values, and replacing them in equation 2.11 to calculate the complex relative permittivity, α and β can be obtained from equations 2.9 and 2.10 respectively. Using those values we can easily obtain different parameters of EM waves in water, such as: propagation loss, wavelength, and velocity of propagation.

The propagation loss for different distances is defined as

$$L(\text{dB}) = \alpha \times \frac{20}{\ln(10)} \times D \quad (2.18)$$

where D is the distance the EM wave propagates and the constant factor is used to convert from Np/m to dB/m.

The wavelength for different frequencies is given by

$$\lambda(\text{m}) = \frac{2\pi}{\beta} \quad (2.19)$$

and the velocity of propagation by

$$u_p(\text{m/s}) = \frac{\omega}{\beta} \quad (2.20)$$

This knowledge will later be used to characterize the propagation of EM waves with frequencies up to 10 GHz for different values of conductivity.

Table 2.2: Debye parameters of water [2].

ϵ_s	ϵ_∞	τ (ps)
80	4.22	9.14

Figure 2.4 presents the attenuation of an EM wave in water as a function of its frequency for different values of conductivity using equation 2.9 and 2.11. It is observed that the conductivity is a very important parameter that defines the overall relation between propagation and attenuation of EM waves confirming that sea water ($\sigma \sim 4$ S/m) is a very harsh environment for the propagation of RF waves, but in fresh water case ($\sigma \sim 0.01$ S/m) the attenuation is low enough so that communications can be established over a couple of meters using frequencies up to dozens of MHz.

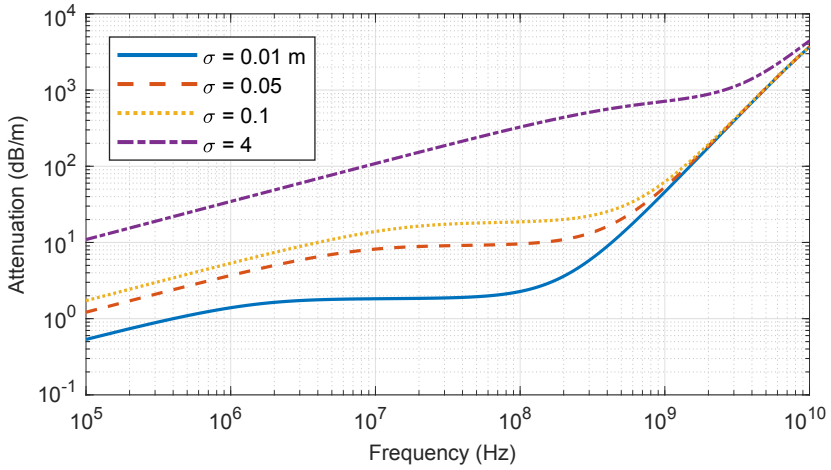

Figure 2.4: Attenuation an EM wave suffers as a function of frequency while propagating in underwater media with different conductivities.

Figure 2.5 shows a plot of the wavelength of an EM wave in water as a function of frequency for different values of conductivity using equation 2.10 and 2.19. It is seen that an increase in the conductivity tends to decrease the wavelength of a wave. In sea water this effect has to be considered for frequencies lower than 1 GHz, while for fresh water this transition occurs at 10 MHz.

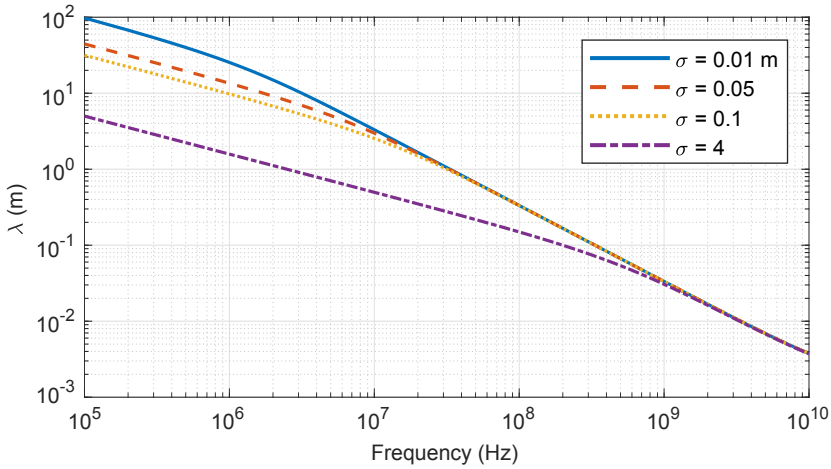

Figure 2.5: Wavelength of an EM wave as a function of frequency while propagating in underwater media with different conductivities.

Figure 2.6 plots the velocity of propagation of an EM wave in water as a function of frequency for different values of conductivity using equation 2.10 and 2.20. The velocity of an EM wave increases gradually until it reaches a limit value of around 3×10^7 m/s; for fresh water this value is reached at a frequency of approximately 10 MHz, whereas for sat water the transition is obtained at 1 GHz.

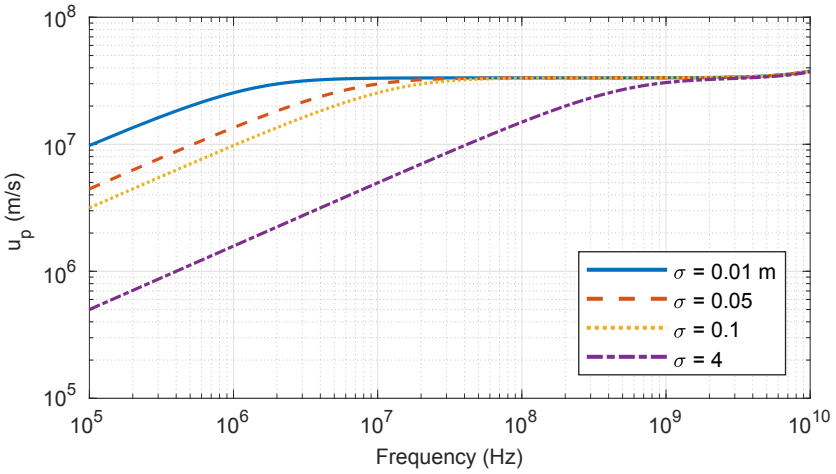

Figure 2.6: Velocity of an EM wave as a function of frequency while propagating in underwater media with different conductivities.

The total power received in an underwater communication system is an important parameter, which is given by by the following equation:

$$P_{rx}(dBm) = P_{tx} + G_{tx} + G_{rx} - L_{FSL} - L_{water} \tag{2.21}$$

where P_{tx} is the transmitted power, G_{tx} and G_{rx} are the gains of the antennas for both transmitter and receiver respectively, L_{FSL} are the free space losses and L_{water} are the losses due to the attenuation of the conductive medium.

2.4 Antennas for Underwater Radio Communications

Antenna design involves an understanding of all the requirements and a fair amount of iterations [21]. In the next subsections some of the antenna fundamental concepts are described, as well as a simple literature review on antennas for underwater applications.

2.4.1 Antenna Parameters

In order to design an antenna for a specific application, several parameters have to be considered. In this section the fundamental antenna parameters are presented, such as radiation pattern, radiation power density, radiation intensity, directivity, efficiency and gain.

2.4.1.1 Radiation Pattern

One of the most important characteristics of an antenna is the radiation pattern. It is defined as a mathematical function or a graphical representation of the radiation of the antenna as a function of space coordinates [22], and is usually determined in the far-field region since it is the region we are usually interested. It is usually represented in logarithmic scale to show in more detail the parts where the pattern is very low, which are called minor lobes.

Since antennas are made to emit and receive power (usually) in some specific directions, this is a very useful and intuitive parameter that shows in which direction the antenna transmits and receives better. Figure 2.7 shows an example of a radiation pattern.

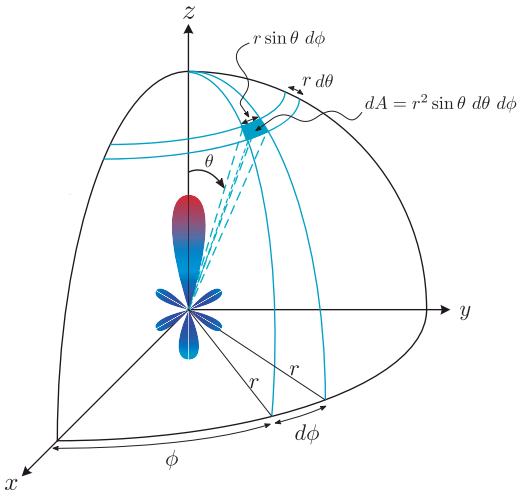

Figure 2.7: Example of a radiation pattern and coordinate system for antenna analysis.

2.4.1.2 Radiation Power Density

The quantity that describes the power associated with an EM wave is the instantaneous Poynting vector and is defined as

$$\mathscr{W} = \mathscr{E} \times \mathscr{H} \tag{2.22}$$

where $\mathscr{W}$ is the instantaneous Poynting vector (W/m^2), $\mathscr{E}$ is the instantaneous electric-field intensity (V/m) and $\mathscr{H}$ is the instantaneous magnetic-field intensity (A/m). The Poynting vector is a power density, meaning that the total power crossing a closed surface can be obtained by integrating the normal component of the Poynting vector over the entire surface:

$$\mathscr{P} = \oiint_S \mathscr{W} \cdot d\mathbf{s} = \oiint_S \mathscr{W} \cdot \hat{\mathbf{n}}\, dA \tag{2.23}$$

where $\mathscr{P}$ is the instantaneous total power (W), $\hat{\mathbf{n}}$ is the unit vector normal to the surface and dA is an infinitesimal area of the closed surface (m^2).

2.4.1.3 Radiation Intensity

Radiation intensity is a far-field parameter and is defined in a given direction as the power radiated from an antenna per unit solid angle. It can be obtained by multiplying the radiation density by the square of the distance:

$$U = r^2 W_{\text{rad}} \tag{2.24}$$

where U is the radiation intensity (W/unit solid angle) and W_{rad} is the radiation density (W/m^2).

To obtain the total radiated power we just have to integrate the radiation intensity over the entire solid angle of a sphere, which is 4π:

$$P_{\text{rad}} = \oiint_{\Omega} U d\Omega = \int_0^{2\pi} \int_0^{\pi} U \ \sin\theta \ d\theta \ d\phi \tag{2.25}$$

where $d\Omega = \sin\theta \ d\theta \ d\phi$ is the element of solid angle.

2.4.1.4 Directivity

Directivity is a fundamental parameter to describe antennas. It measures how "directional" the antenna's radiation pattern is, and is given by the ratio of the radiation intensity in a given direction from the antenna to the averaged radiation intensity over all directions [22]. The latter one is similar to the radiation intensity of a isotropic antenna and given by,

$$U_0 = \frac{P_{\text{rad}}}{4\pi} \tag{2.26}$$

so we can measure directivity as

$$D = \frac{U}{U_0} = \frac{4\pi U}{P_{\text{rad}}} \tag{2.27}$$

Thus, directivity can also be seen as the ratio of the radiation intensity of the nonisotropic source in a given direction over that of an isotropic source.

Even though this parameter can be measured in any direction, it is common to measure it for the direction of maximum radiation intensity, which gives the maximum directivity and is expressed as

$$D_{\text{max}} = \frac{U}{U_0} = \frac{4\pi U_{\text{max}}}{P_{\text{rad}}} \tag{2.28}$$

2.4.1.5 Efficiency

There are many efficiencies associated with the radiation of an antenna and usually arise due to the reflection losses at the input terminals of the antenna and due to conduction and dielectric losses in the structure of the antenna. Thus, the overall efficiency can be written as

$$e_0 = e_r e_c e_d \tag{2.29}$$

where e_0 is the total efficiency, e_r is the reflection efficiency due to mismatch, e_c is the conduction efficiency, and e_d is the dielectric efficiency.

2.4.1.6 Gain

The gain parameter is closely related to the directivity parameter but it takes into account the radiation efficiency of the antenna. Gain is then defined as the ratio between the radiation intensity, in a given direction and the radiation intensity that would be obtained if the power accepted by the antenna were radiated isotropically [22]. In mathematical form:

$$G(\theta,\phi) = 4\pi \frac{U(\theta,\phi)}{P_{in}} \tag{2.30}$$

Since $P_{in} = P_{in}/e_{cd}$, we can express the gain as a function of directivity (Equation 2.27):

$$G(\theta,\phi) = e_{cd} D(\theta,\phi) \tag{2.31}$$

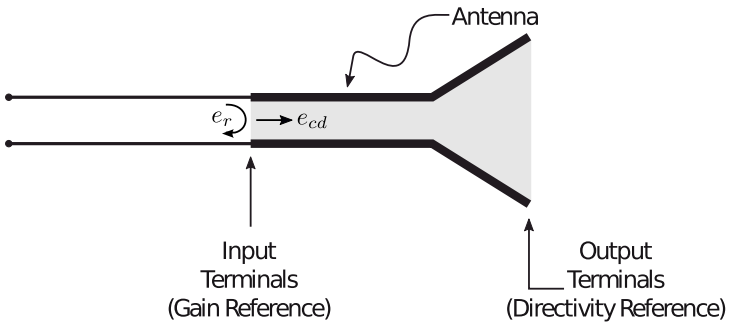

Figure 2.8: Illustration of the reference terminals and losses of an antenna.

Note that the gain does not take into account the mismatch losses of the antenna but only the radiation losses.

2.4.2 Antenna Design

An antenna is basically a conductor which has a length that is a ratio or a multiple of the wavelength of the signal that propagates through it. This condition is usually called resonance as the electrical energy fed to the antenna is radiated into free space. [22]

It was shown in Section 2.3 that RF waves/fields have a very different behavior in a lossy medium (like freshwater or seawater). It was shown that the wavelength decreases due to the high permittivity thus, the size of an antenna designed for underwater medium is smaller compared to a design for air. In the same section it was demonstrated that the attenuation increases as a function of frequency and conductivity, which shows the importance of selecting a low frequency for operation of the antenna for underwater longer communications. Hence, RF communications are very inefficient in seawater. Yet, at frequencies,below 100 MHz, EM waves propagate relatively well in fresh water and so this project aims to design an Up-Down Converter, including the antenna,

targeting these range of frequencies. In [23] it is shown that the most used antennas that operate at these frequencies are the loop antennas and the electric dipoles.

Loop antennas are very simple and cheap, and can be manufactured in different shapes, like rectangular, square and circular, using copper wire. They are similar to magnetic dipoles in the way that their radiation have the same mathematic form of an infinitesimal magnetic dipole, with the fields radiated outwards of the loop plane [22].

The software that was used to design and simulate the underwater antenna was FEKO. A simple antenna design done in this software is shown in figure 2.9. This figure shows a square loop antenna with a finite ground plane used to increase the directivity of the antenna.

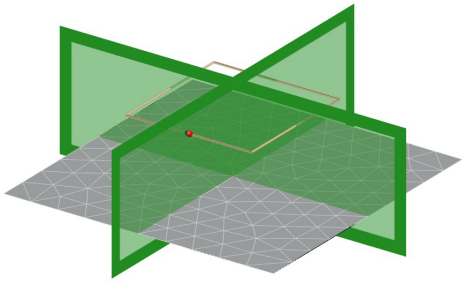

Figure 2.9: Illustration of an antenna design using FEKO software.

2.5 RF Circuit Design

RF circuits are the most common PCB designs in wireless communication systems due to their ability to deal with high frequencies. However, as the frequency increases, the design complexity also increases. To successfully design a PCB that performs well at high frequencies it is essential to understand the basics of RF design, including concepts such as the characteristic impedance, transmission lines, S-parameters, return loss, insertion loss and impedance matching. This section is based on documents about RF layout guidelines such as [24], [25] and [26], and presents the basics of printed circuit board design, exploring what are the main concerns when designing one.

2.5.1 Transmission Lines

Transmission lines are used to carry RF power from a source to a load. To do this task efficiently several types of transmission lines were developed, but for RF frequencies there are two that are very popular: the microstrip line and the coplanar waveguide with lower ground plane (CPWG). They are popular because they are simple, cost effective and there are several tools to calculate their electrical parameters. An illustration of these two different transmission lines is shown in Figure 2.10.

Compared with microstrip lines, CPWG lines usually provide better isolation for RF traces and better EMI performance, provide lower cross-talk between other traces and have lower losses

Figure 2.10: Illustration of the electric fields in a Microstrip Line and in a CPWG Line.

for high frequencies. For all these reasons, CPWG are often chosen as a mean to carry the RF signals between the different nodes of the system [25].

A detailed illustration of this type of line is shown in figure 2.11. There are different factors that define its characteristic impedance, such as its height (h), width of the adjacent ground fill (w_1), width of the trace (w_2), width of the gap between the trace, the adjacent ground fill (w_3), the dielectric constant of the substrate (ε_r), and the stackup used. These factors should be adjusted to ensure that the line has a 50 ohm characteristic impedance, which can be done by using impedance calculators. The value of 50 Ohm is chosen because most of the devices available used in RF circuits are matched for a 50 Ohm impedance.

There are several recommendations that should be taken into account for a good performance of the CPWG line, such as:

- The CPWG should maintain a constant gap between the RF trace and the adjacent ground, and this gap should be lower than the height of the substrate, otherwise the predominant mode would be the microstrip mode.
- The ground beneath the RF trace should be clean and uninterrupted to ensure a proper return path for the RF currents. The length of the RF traces should also be as small as possible since every trace, as well as the substrate beneath it, attenuates the signal in proportion with the distance.
- Bends in the RF trace should be avoided, and if needed, a curve is preferred since it maintains a uniform width. In this case the radius of the curve should be at least 3 times the center conductor width to minimize the change in the characteristic impedance.
- Finally, RF traces should not be placed close or parallel to other traces since it might cause mutual coupling of the signals between traces.

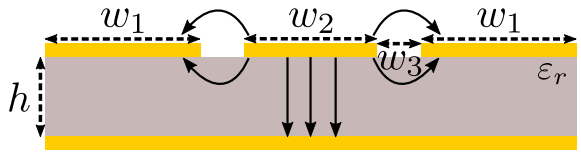

Figure 2.11: Detailed illustration of the CPWG Line.

2.5.2 Impedance Matching

The higher the frequency, the more difficulty it is to do an impedance match meaning that this is a very important topic on RF PCB Design. It is then very important that all the circuits are impedance matched to avoid undesired losses and reflections of the propagating wave signals. It is also very important to keep the lengths of the line small being more critical as the length of the line increases.

Impedance matching has a large theoretical background and it is not the scope of this master thesis work to explain it. For this work, a better impedance match on port x will be seen as a lower $|S_{xx}|$ (subsection 2.5.4). Several tools can be used to perform impedance matching, and the ones used in this work are: ADS, Keysight; HFSS, Ansys; and FEKO, Altair.

2.5.3 Other RF Considerations

In this subsection, important considerations about RF design is mentioned, including the difference between types of PCB stackups, the importance of a having a solid ground plane and vias, the importance of power supply decoupling and the different characteristics of capacitors and inductors used in RF design.

2.5.3.1 PCB Stackup

The stackup of a PCB is highly related with the performance that it can achieve. Usually two different stackups are used in RF designs: a four-layer PCB and a two-layer PCB, both illustrated in Figure 2.12.

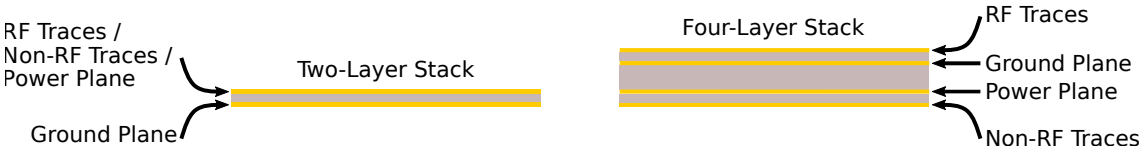

Figure 2.12: Difference between a four-layer stackup and a two-layer stackup.

The use of four-layer boards turns the layout more robust since it offers a complete ground and power plane and a simpler signal routing. Despite that, the price is higher and this can be a problem for price sensitive applications.

A two layer board is harder to design but is cheaper and can achieve also a good performance if the right RF tools and techniques are used. In this case, if it is not possible to have a complete bottom ground plane, it should be as solid as possible mainly beneath the RF traces. A two-layer board should also be as thin as possible since for a fixed characteristic impedance, the width of the line is directly proportional to the substrate height.

2.5.3.2 Ground Plane and Vias

One of the most important parts in a RF design is the ground plane, which is the plane that defines the reference voltage for any other DC or AC signal in the circuit, and the plane that offers the main current return path.

It is then highly recommended to use a wide, solid and continuous ground plane as reference plane, mainly beneath the RF traces since if the return path of a RF signal is broken, the return currents will have to find the next smallest path around the interruption, and it may have a considerable electrical length that adds undesired inductance affecting the performance of the system.

To improve the ground performance, and ensure that all the board has the same reference voltage, ground vias should be liberally used to connect all the ground planes in the PCB. This helps to reduce the parasitic ground inductance and also is very helpful in heat dissipation [26].

Another important usage for the vias is for the components that are shunt connected to the ground. The best ground return path for a component is the ground plane beneath it. In this case vias should be used as close as possible to the component pad to ensure a reduced return path. It is recommended to use at least two vias for each component which helps to reduce the parasitic inductances introduced by the vias. This is also very important for an integrated circuit (IC) ground pad where the maximum number of vias that are allowed by the PCB design rules should be used since it provides both thermal relief for the IC [24], and guarantees that the IC sees the same ground as the rest of the board.

To complete this subsection, Cypress Semiconductor gives also the following recommendations to improve the ground performance [25]:

- Do not have split grounds unless no current loops are formed in the ground for the current in the return path.
- Allow a wide ground plane beneath the RF trace. Narrow ground planes permit parasitic modes of transmission and increase leakage.
- The bottom ground plane, together with the top ground plane and vias between the two ground planes, ensures that all traces are well shielded. This arrangement significantly improves the EMI and EMC performance.

and to ensure a proper usage of the vias:

- Use plenty of vias spaced not more than one-twentieth of the wavelength of the RF signals between ground fillings at the top layer and bottom layer.
- Never share a via with multiple pins or pads.
- Avoid using vias to route the RF trace to a different layer.
- Whenever possible, use vias to form a ground fencing around the RF section to isolate it from the rest of the circuit.

2.5.3.3 Power Supply Decoupling

One important topic on RF design is noise decoupling from the power supply pins off all the modules present in the PCB. Noise on the power supply can increase the phase noise of the frequency synthesizer in a radio system, resulting in a poor signal quality. It can also cause instabilities in the RF output resulting in undesired interference and spurious radiations. In the receiver it limits the sensitivity and the signal to noise ratio (SNR) and increases the packet error of the communication.

In order to prevent that the noise generated at one device reach the others, one or more decoupling capacitors are used and their characteristics needed for a good decoupling are shown in subsection 2.5.3.4. Cypress Semiconductor gives the following recommendation for a improved power pupply decoupling [25]:

- Place the components as close to the supply pin as possible.
- Place the smallest-value capacitor closest to the power supply pin
- The power supply should flow through the decoupling capacitors to the power supply pin of the IC.
- Use separate vias to ground for each decoupling capacitor.

2.5.3.4 Capacitors and Inductors

Capacitors and inductors have a non-ideal behavior that becomes more relevant as the frequency increases and should be taken into account depending on the application for which they are used.

2.5.3.4.1 Capacitors

In the case of the capacitors, the equivalent electrical circuit includes a parasitic resistance (R_p), a parasitic capacitance (C_p) and a parasitic inductance (L_p) as illustrated in Figure 2.13.

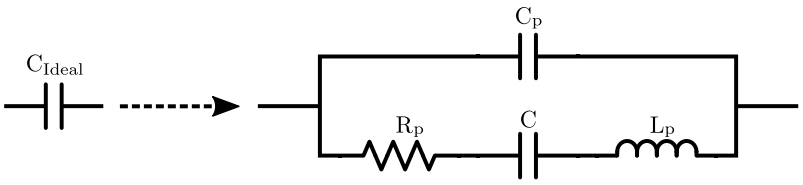

Figure 2.13: Equivalent model of a capacitor.

Its effective impedance is then given,

$$X_{\text{eff}} = \frac{(X_L + X_C + R) \times X_{C_p}}{X_L + X_C + R + X_{C_p}} \tag{2.32}$$

where the reactance due to the capacitance C and due to the parasitic capacitance C_p are given respectively by,

$$X_C = -\frac{1}{2\pi fC} \ , \ X_{C_p} = -\frac{1}{2\pi fC_p} \tag{2.33}$$

and the reactance of the parasitic inductance is given by,

$$X_{L_p} = 2\pi fL. \tag{2.34}$$

The reactance of a capacitance then decreases with an increase in frequency while the reactance of an inductance increases with an increase in frequency. Since C_p is usually very low in relation to C, X_{eff} can then be approximated by,

$$X_{\text{eff}} = X_L + X_C + R \tag{2.35}$$

.

At low frequencies the circuit is then predominantly capacitive being $X_{\text{eff}} \approx X_C$. As the frequency increases, X_C keeps decreasing and X_L keeps increasing, and eventually they will be equal turning $X_{\text{eff}} \approx R$. The frequency where the capacitor is purely resistive is known as the self resonant frequency (SRF) of the capacitor. After the SRF, the capacitor starts to be inductive.

The previous results show that for impedance-matching purposes, the capacitor chosen should have an SRF much higher than the operating frequency since in this case the effective capacitance will be near the nominal value. On the other hand, for decoupling purposes, the SRF should be on the noise frequency to be decoupled, ensuring that the noise sees a low-impedance path to the ground. To note that above the SRF the capacitor behaves like an inductor and therefore will not perform the decoupling or bypass function. For broadband decoupling several decoupling capacitors are needed, each one to filter a specific band of noise frequencies.

Another important parameter of a capacitor is the quality factor (Q factor) which is the ratio of the reactance of the capacitor to its resistance at a given frequency, mathematically given by,

$$Q = \frac{1}{2\pi fCR} \tag{2.36}$$

.

High-Q capacitors have less undesired resistance and should be used on RF circuits otherwise energy can be wasted as heat in the resistance of the capacitor.

To complete this subsection, Cypress Semiconductor gives also the following recommendations for capacitors [25]:

- Only C0G/NP0 capacitors should be used for components of the matching network, ensuring that the matching network does not change across temperatures.

- For decoupling capacitors, the accuracy of the C0G capacitors may not be needed and the X5R or X7R capacitors (depending on the temperature range) could be used. A low ESR capacitors is important for effective decoupling.
- It is recommended to use smaller components (0402 or 0201), as they have less parasitic reactance
- When adding a DC block to an RF trace that is already matched a capacitor with an SRF close to the frequency of operation and a low ESR should be used, as the capacitor's effective reactance becomes zero at SRF and not alter the impedance matching.

2.5.3.4.2 Inductors

The inductors also have a parasitic capacitance and a parasitic resistance as illustrated in Figure 2.14 [25].

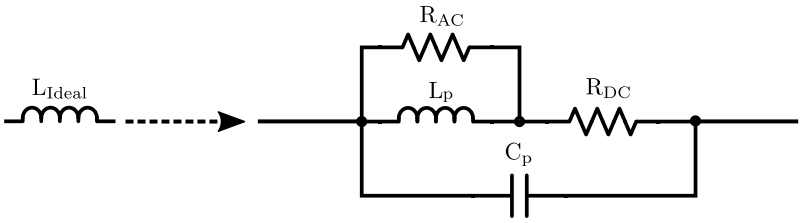

Figure 2.14: Equivalent model of an inductor.

R_{AC} is usually ignored for low frequencies [25] and for the inductors the effective impedance is given by,

$$X_{\text{eff}} = \frac{X_{C_p} \times (X_L + R_{DC})}{X_{C_p} + X_L + R_{DC}}. \tag{2.37}$$

As showed before, the parasitic capacitance has a very high reactance at low frequencies but low impact on the overall impedance since it is parallel to the inductor which has a low reactance for low frequencies. As frequency increases, the reactance due to the capacitor decreases and the reactance due to the inductor increases and eventually will have the same value and that is the SRF of the inductor. R_{DC} is typically very low, which sets the behavior of the inductor as an open circuit (LC circuit) at the SRF.

The inductors used for a matching network must have a SRF much higher than the operating frequency, while the ones used for power supply filtering must have the SRF near the operating frequency.

The Q-Factor for the inductor is mathematically given by,

$$Q = \frac{2\pi f L}{R}, \tag{2.38}$$

.

and in this case it is important to ensure a high Q-Factor at the operating frequency for matching networks since by using inductors with low Q, much of the energy is wasted in the resistance as heat, and a possible good result obtained for the $|S_{11}|$ could be mislead because most of the energy might not pass to the load.

To complete this subsection, Cypress Semiconductor gives also the following recommendations for inductors [25]:

- Inductors should not be placed parallel and close to each other. The mutual inductance between them causes cross-talk. Place inductors or unrelated sections orthogonal to each other.
- Wire-wound inductors have low DC resistance, so they have a high Q and current capacity. Wire-wound inductors are preferred over ceramic inductors for high-value inductors.

2.5.4 S Parameters

Despite the existence of elementary circuit theory methods to describe electronic networks, like Kirchhoff's circuit laws, these methods tend to be more complex when used to describe circuits whose operation wavelength starts to become comparable to its physical dimensions. In these cases, there is an adequate technique that provides a complete description of the network as seen at its N ports, and that way is by measuring the Scattering parameters or as it usually called, the S Parameters. These parameters can be represented by a matrix that relates the voltage incident on the ports to those reflected from the ports [27]. So for a N-port circuit, the scattering matrix will be an $N \times N$ matrix and the relation between these incident and reflected voltage waves for any port is given by,

$$\begin{bmatrix} V_1^- \\ V_2^- \\ \vdots \\ V_N^- \end{bmatrix} = \begin{bmatrix} S_{11} & S_{12} & \cdots & S_{1N} \\ S_{21} & S_{22} & \cdots & S_{2N} \\ \vdots & \cdots & & \\ S_{N1} & S_{N2} & \cdots & S_{NN} \end{bmatrix} \begin{bmatrix} V_1^+ \\ V_2^+ \\ \vdots \\ V_N^+ \end{bmatrix}, \tag{2.39}$$

in which a generic element S_{ij} can be determined by

$$S_{ij} = \left. \frac{V_i^-}{V_j^+} \right|_{V_k^+ = 0 \ \forall \ j \neq k} \tag{2.40}$$

meaning that S_{ij} is found by applying an incident voltage wave on the port j (V_j^+), and measure the amplitude of the reflected wave on port i (V_i^-) when all the other ports are terminated in matched loads to avoid reflections.

As an example, in Figure 2.15 we can see a system with two ports. This is the most simple and usual case. As a 2 port system we have 4 elements in the Scattering Matrix,

$$S = \begin{bmatrix} S_{11} & S_{12} \\ S_{21} & S_{22} \end{bmatrix}, \tag{2.41}$$

so, as explained before, it is possible to measure the four elements in the presented way:

- S_{11} - By injecting a wave on Port 1 (V_1^+), and see how much of it is reflected on the same Port (V_1^-) while the Port 2 is matched. This is also known as the reflection coefficient and gives us a measure of how well Port 1 is matched.
- S_{22} - By injecting a wave on Port 2, we inject a wave on Port 2 (V_2^+), and see how much of it is reflected on the same Port (V_2^-) while Port 1 is matched, which gives the reflection coefficient on port 2 and a measure of how well the port is matched.
- S_{21} - By injecting a wave on Port 1 (V_1^+), and see how much of it reaches Port 2 while this port is matched. This is also know as the direct transmission coefficient and gives us the gain/loss experienced between Port 1 and Port 2.
- S_{12} - By injecting a wave on Port 2 (V_2^+), and see how much of it reaches Port 1 while this port is matched. This is also know as the inverse transmission coefficient and gives us a measure of the isolation between Port 2 and Port 1.

These values are complex, so they have magnitude and phase whist the magnitude is usually represented in dB. These parameters are very important as they can describe the behavior the network.

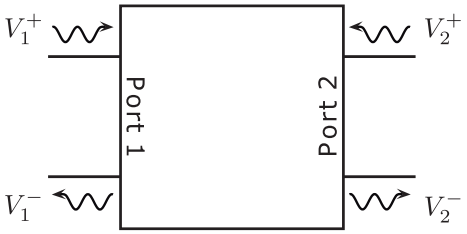

Figure 2.15: Two port network.

The equipment that is used to measure these parameters is the *Vector Network Analyzer*. An illustration of this equipment is presented in figure 2.16.

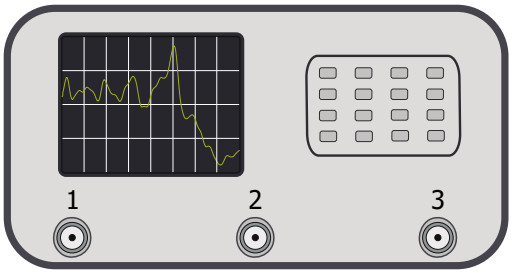

Figure 2.16: Illustration of a VNA - *Vector Network Analyzer*.

2.6 Mixer

A mixer is a three-port device where two of the ports act as input and the other acts as an output. The purpose of the mixer is to use the two input signals to output a signal that is either the sum or difference frequency of the inputs, or in mathematical form,

$$f_{\text{out}} = f_{\text{in}_1} \pm f_{\text{in}_2}. \tag{2.42}$$

The nomenclature for the 3 mixer ports is: LO (Local Oscillator) port, the RF (Radio Frequency) port, and the IF (Intermediate Frequency) port. At the LO port a sinusoidal or square wave signal (depending on the application) is injected to tune the output frequency to the desire frequency, being this port an input port. The other two ports can be interchanged as input or output. If the desire output frequency is lower than the second input frequency, the process is called downconversion,

$$f_{\text{IF}} = |f_{\text{LO}} - f_{\text{RF}}| \tag{2.43}$$

while if the desire output frequency is higher than the second input frequency, the IF is the input and the RF is the output and the process is called upconversion,

$$f_{\text{RF}} = |f_{\text{LO}} + f_{\text{IF}}|. \tag{2.44}$$

An illustration of both these processes is represented in figure 2.17. It is observed that in the upconversion process, there is a high proximity between the sum and difference frequency, which means that both will be available at the RF port. This is also know as a double sideband upconversion and there are mixers who cancel one of these components, called single sideband upconverters.

Usually there is information modulated into the carrier frequency (as seen by the broadened spectrum at RF and IF center frequencies). This information that is carried by one of these signal is translated to the other one on the process of frequency conversion and that is the reason why mixers are the center core in this work.

The main key performance indicators for a mixer are shown in [1], a document where this topic is very well explained, and are summarized in the following subsections.

2.6.1 Conversion Loss

Conversion loss is perhaps the most important mixer parameter and is defined as the amount of power lost in the frequency conversion process, or in mathematical terms,

$$\text{CL (dB)} = \text{P}_{\text{RF}}\text{ (dBm)} - \text{P}_{\text{IF}}\text{ (dBm)}. \tag{2.45}$$

where CL is the conversion loss, P_{RF} is the RF signal power and P_{IF} is the IF signal power. Usually conversion loss ranges between 4.5 to 9 dB depending on the mixer [1]. Wider bandwidth mixers

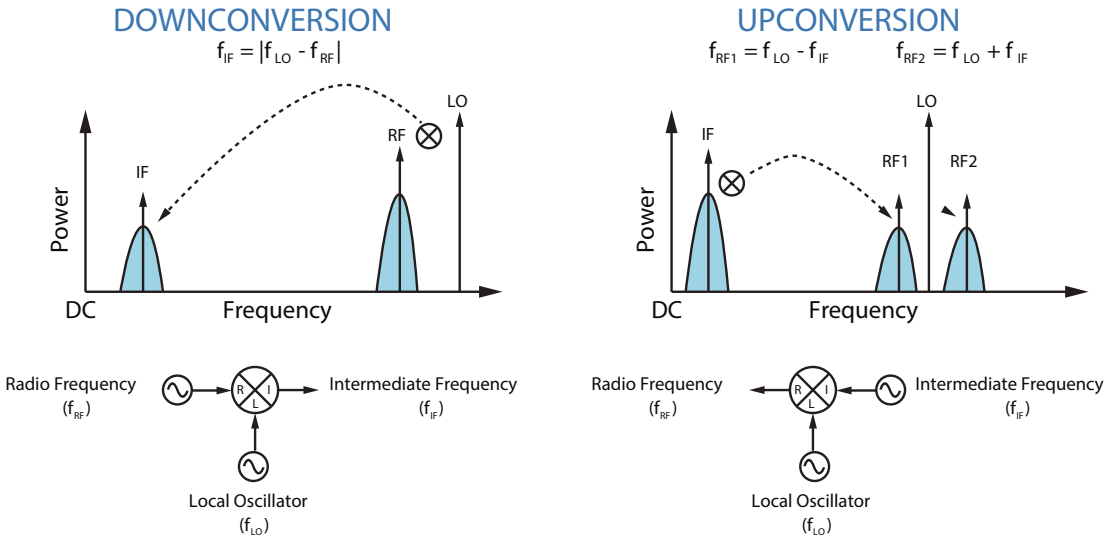

Figure 2.17: Ilustration of a downconversion and an upconversion [1].

also tend to have higher conversion losses due to the difficulty in maintaining circuit balance over the entire bandwidth. Conversion losses correlates closely with other metrics such as isolation or 1 dB compression and usually, for a good mixer design, if the conversion loss is within a narrow specification, all other performance metrics will meet the required specifications, and that is why it is a benchmark mixer metric.

2.6.2 Isolation

Isolation is a measure of the amount of power that leaks from one mixer port to another. The isolation is approximately reciprocal which means that the isolation from port 1 to port 2, should be similar to the isolation from port 2 to port 1. There are then three different isolation parameters: LO-RF, LO-IF, and RF-IF. As an example, the LO-RF is given by,

$$P_{ISO\ (L\text{-}R)}\,(\mathrm{dB}) = P_{in\ (LO)}\,(\mathrm{dBm}) - P_{out\ (RF)}\,(\mathrm{dBm}). \tag{2.46}$$

The other ones can be measure in a similar way.

2.6.3 1 dB Compression Point (P1dB)

If the RF (IF) input power is increased by 1 dB it is expected that IF (RF) output power also increases by 1 dB, meaning that the conversion loss is constant. In practice, the RF output signal will saturate and this relation will not be linear. This parameter is then a measure of the linearity of the mixer and is defined as the input power needed to increase conversion loss by 1 dB from its ideal value.

2.6.4 Noise Figure

The noise figure of a mixer can be approximated by the conversion loss. Since this parameter limits the minimum detectable signal at the receiver, a low power application require a low conversion loss.

2.7 Summary

The previous introduction showed that antenna design and RF design are a very challenging and delicate subject that has several physical effects that if not taken into account might impair or even destroy the functionality and performance of the system. The knowledge presented in this section was used throughout the whole work.

This chapter ends with a photograph of different previous versions of Up/Down Converters for the same frequency bands built at INESC-TEC (Figure 2.18).

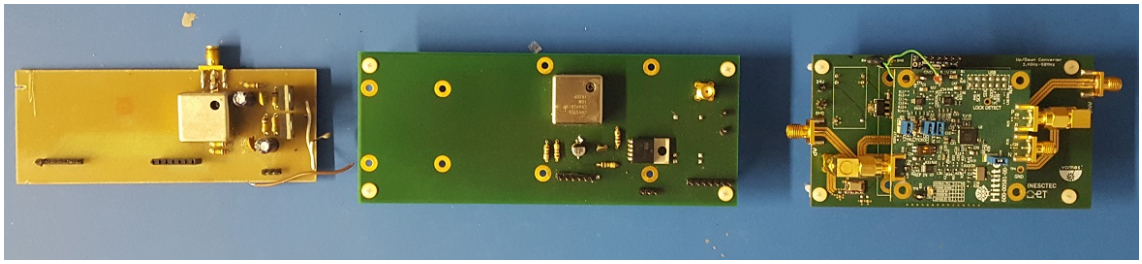

Figure 2.18: Previous versions of Up-Down Converters for the same frequency bands built at INESC-TEC.

Chapter 3

Antenna Design and Implementation

In this chapter it is presented the development and implementation of the antenna used to establish the underwater communication. Initially, it is shown the antenna design using an electromagnetic simulator software called FEKO; then the characterization of the manufactured antenna is presented, ending with the comparative analysis between the results obtained experimentally and in the simulation.

3.1 Antenna Design

The antenna designed for this master thesis needs a bandwidth of at least 20 MHz (maximum bandwidth of the Wi-Fi signal) centered at the carrier frequency of 100 MHz (carrier frequency used for the underwater link, as will be seen later). It should have a high directivity in order to enhance the distance of communication but not too high since the position of the AUV will not be fixed, having been decided to use a value between 5 and 10.

As demonstrated in [28], one antenna that meets all this requirements is the square loop antenna with a reflector. The designed antenna was actually based on the one published in that paper, but instead of designing it for 50 MHz, it was designed for 100 MHz.

The square loop antenna has a square shape and is manufactured using copper wire. The length of each side is equal to $\lambda/4$ being the total length of the antenna equal to λ. The radiation pattern of a square loop is bi-directional in the plane perpendicular to the plane of the loop, but it is possible to turn the overall antenna more directive by using a reflector parallel to the plane of the loop and at a typical distance of $\lambda/4$ [28]. This ensures that part of the radiation that goes in the direction of the reflector is reflected back turning the overall radiation much more directive in one direction. By using the Debye model presented in Section 2.3 it is possible to obtain the electrical length of $\lambda/4$, and its value corresponds to 8.32 cm in an underwater environment with 0.0353 S/m of conductivity (value obtained in INESC TEC's pool as will be seen later). This dimensions were then the key parameters used in FEKO, an electromagnetic simulation software, to begin the design of the antenna.

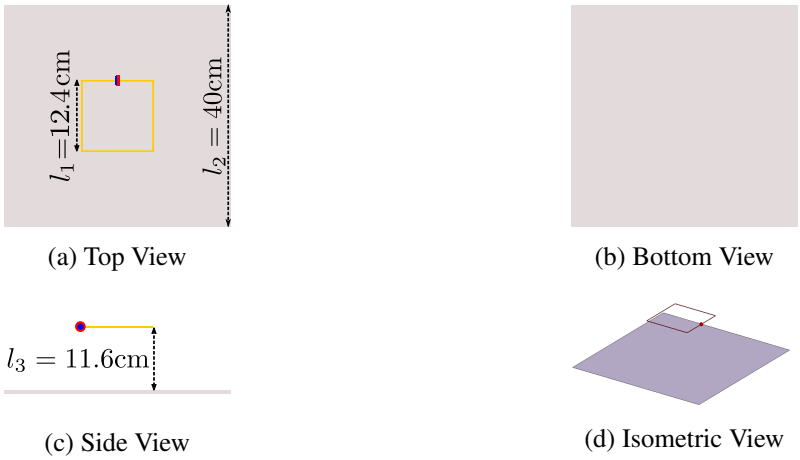

(a) Top View

(b) Bottom View

(c) Side View

(d) Isometric View

Figure 3.1: Different views of the designed Square-Loop Antenna.

Through parametric analysis, and having the goals to minimize the reflection coefficient at 100 MHz, increase the directivity in the direction perpendicular to the loop and to have a real and imaginary parts of the input impedance equal to 50 Ohm and 0 Ohm, respectively, at 100 MHz, it was possible to find the values that best fit those characteristics.

The optimized values for the length of each side of the square loop antenna and reflector were 12.4 cm and 40 cm respectively. The thickness of the wires used to design the antennas is 3 mm and are covered with an insulating material with thickness of 50 μm and ϵ_r=3. The aluminum used for the reflector has 2mm of thickness.

The antennas were then simulated for a fresh water medium with a conductivity of 0.035S/m and a ϵ_r=81. Figure 3.2 shows the obtained results for the reflection coefficient, real and imaginary part of the input impedance, and the polar graph for the E-Plane (left) at $\phi = 0^o$ and H-Plane (right) at $\theta = 0^o$.

The results showed that the first resonant frequency occurs around the expected frequency of 100 MHz with a reflection coefficient of -20.35 dB. The -10 dB bandwidth of the antenna is 127.83 MHz, but it is composed by the first and second resonant frequencies. The bandwidth measured for the first resonance, which is the one that radiates to the perpendicular plane of the loop, is 42 MHz (78 MHz-120 MHz) and was measured by using the reflection coefficient graph and evaluating the radiation pattern for each frequency by steps of 1 MHz. The real and imaginary parts of the input impedance are 50 Ohm and 8 Ohm, respectively, at 100 MHz. The half power beamwidth is 68.23^o which enables the AUV to move considerable in relation to the perpendicular plane of the loop. The antenna has a directivity of 8.4 dBi which allows a higher communication distance than the square loop without reflector. This last result is also confirmed by Figure 3.3, which shows the simulation results for the $|S_{21}|$ parameter as a function of distance for two square loop antennas with reflector, and without reflector. The two curves are shifted from each other for about 7 dB, with shows a 3.5 dB extra Gain from each antenna by using the reflector.

After evaluating all the obtained results it is possible to confirm that the designed antenna meets all the system requirements needed to enhance the performance of the system in terms of

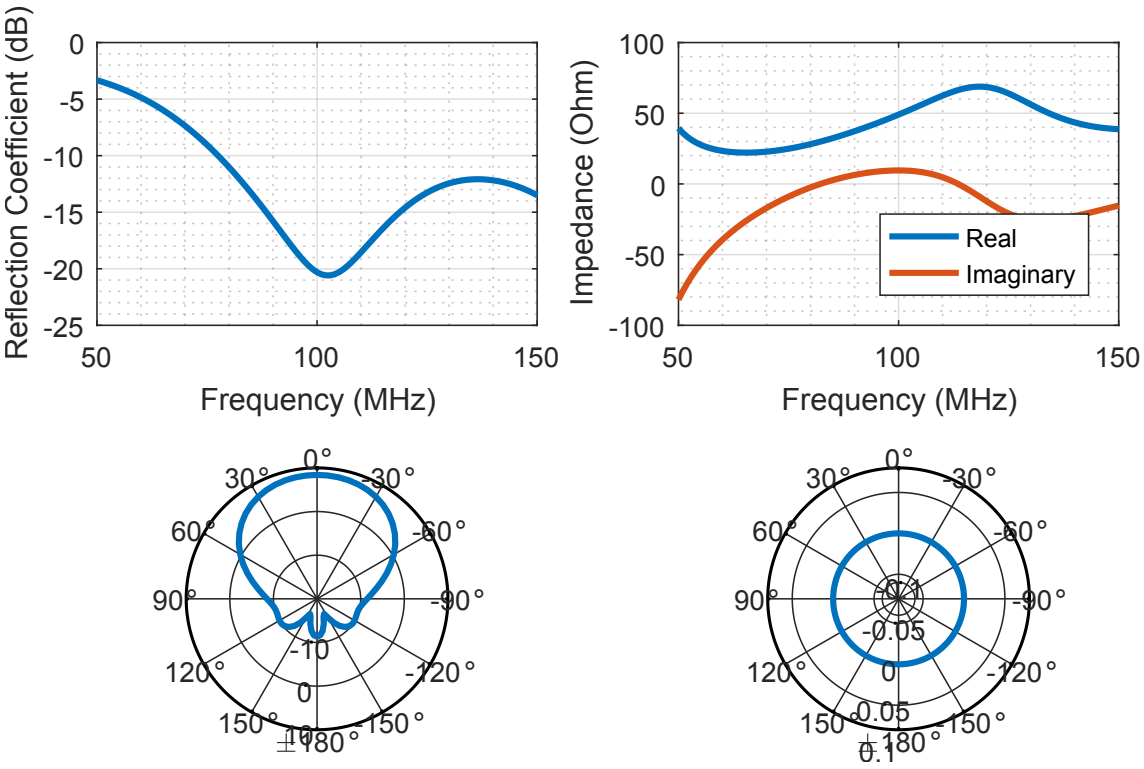

Figure 3.2: Obtained results for the simulation of the square loop antenna with reflector.

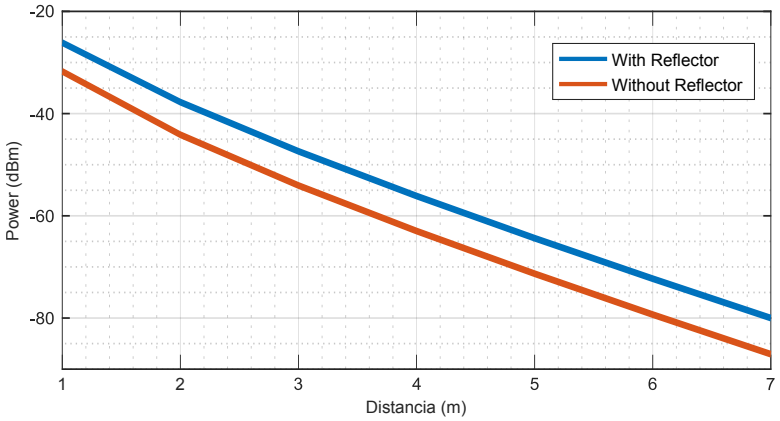

Figure 3.3: Comparison on the magnitude of the electric field between the square loop with and without reflector at a distance of 0.8 m.

distance of communication, data-rate and robustness. For that reason, this was the manufactured antenna.

Since the square loop is a balanced antenna and the coaxial cable is an unbalanced transmission line, a balun (balanced-to-unbalanced) was needed to perform this transition. The balun used was the same used for the Mixer (Section 4.2.8) and the designed PCB board is shown in Figure 3.4a.

This electronic had to be protected from the water. To do this, the whole board was filled with epoxy. Then, four spacers were printed in the 3D printer to force and stabilize the distance

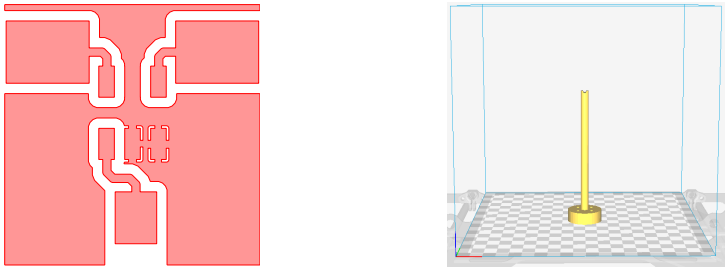

(a) (b)

Figure 3.4: PCB used to connect the coaxial cable to the antenna (a) and spacers used to distance the loop from the reflector (b).

between the square loop and the reflector (Figure 3.4b). The two final built square loops are shown in Figure 3.5.

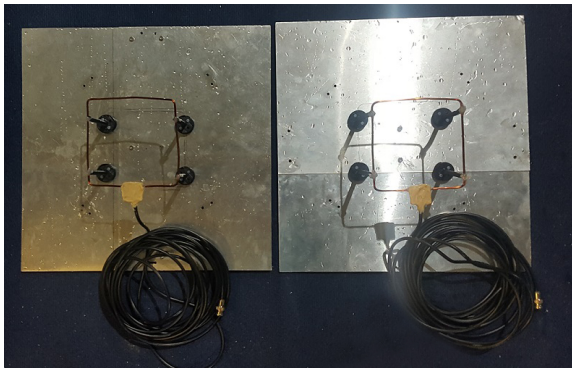

Figure 3.5: Photograph of the square loop antennas built for this work.

3.2 Antenna Characterization

By using a Vector Network Analyzer (VNA) it was possible to measure the $|S_{11}|$. The reference plane of the calibration was at the end of the coaxial cable (length = 5 m, attenuation= 1.55 dB), meaning that the effect of the line is not de-embedded from the measurement. The comparative results between simulation and measurement are shown in Figure 3.6.

It is possible to see that there was a small shift of 8 MHz, that can be explained by two reasons:

- The wire was cut to connect to the pads of the PCB. Since they become smaller, it may have forced a little up-shift in the frequency.
- The bend was made manually and it was not possible to bend it perfectly by 90^o. As the wire takes longer to do the bend, the effective width of the sides of the square loop decreases, which shifts the frequency up.

The solution to this shift is to cut the wire a little longer, and try as much as possible to perform a 90^o bend on the sides of the square loop. Due to inexperience, this two considerations were not

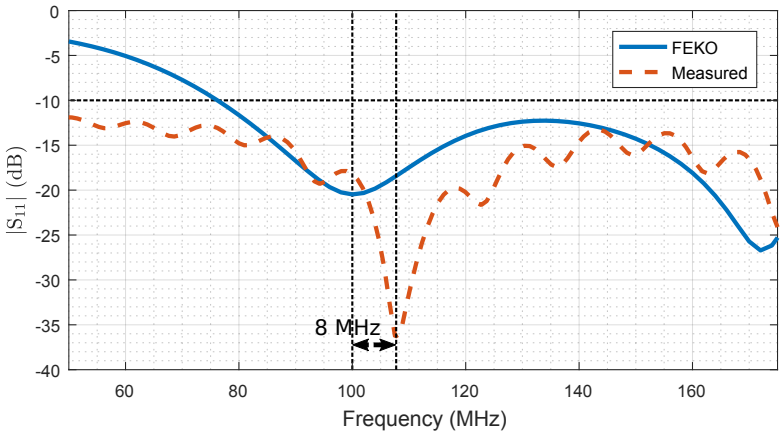

Figure 3.6: Results of the reflection coefficient for the square loop antenna.

taken into account. There is also a small vertical shift that can be explained by the attenuation on the cable and a wavy behavior that can be explained by the different resonances that occur on the coaxial cable.

Despite the resonant frequency of the built antenna is at 108 MHz it still operates very well between 90 MHz and 110 MHz with a return loss higher than 15 dB.

The second measurement was the radiation pattern of the antenna and the setup used to measure it is shown in Figure 3.7. Two plastic pipes were holding the antennas while they were placed front to front. Then one of the antennas was rotated between 0 and 360 degrees in steps of 5.

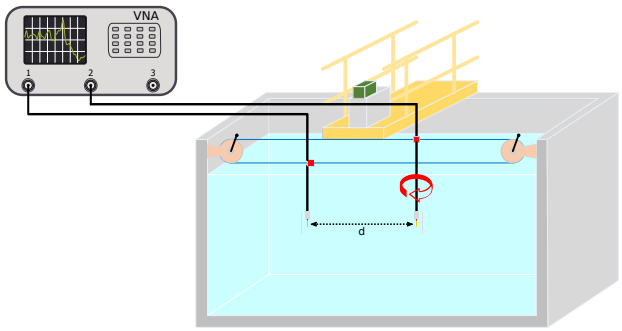

Figure 3.7: Setup used to measure the radiation pattern of the square loop.

The obtained results for the normalized radiation pattern in the E-Plane are shown in Figure 3.8. It is verified that the results were very similar with the ones obtained in the simulation, having the maximum and minimum of directivity at the expected values of θ. Thus this antenna will perform as expected in the final developed system.

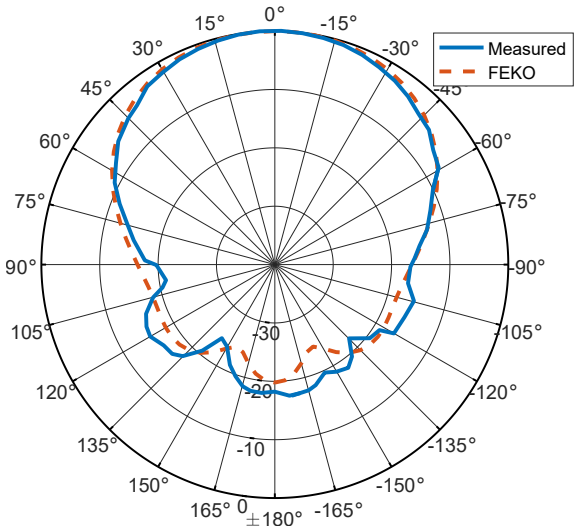

Figure 3.8: Radiation Pattern in the E-Plane of the built square loop antenna.

Chapter 4

Up-Down Converter Design and Implementation

In this chapter it is presented the development and implementation of the Up-Down Converter. Initially, it is shown the proposed methodology for the implementation of the system, showing the system level design and its constraints; then it is shown the component selection and its validation using self designed evaluation boards, ending with the characterization of the performance of the final designed board by doing different tests in a workbench at the laboratory, including the measurement of the S-Parameters and EVM obtained.

4.1 System Level Design

The basic structure of the Up-Down Converter is graphically shown in Figure 4.1.

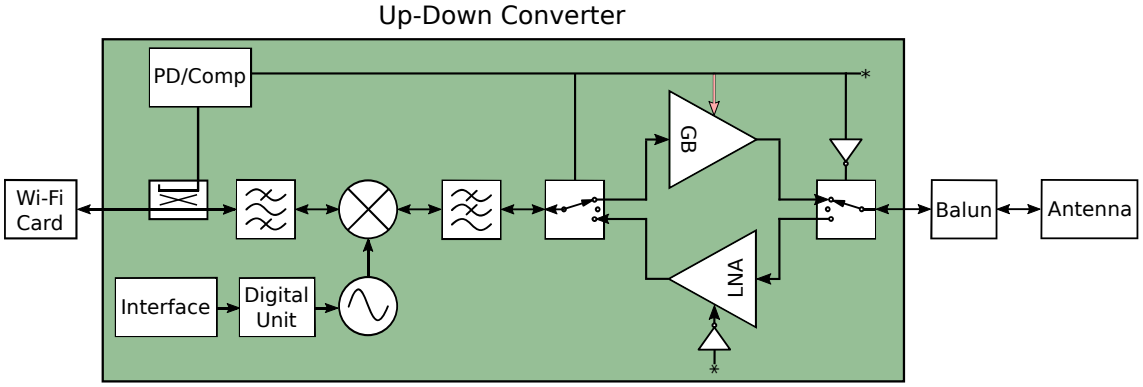

Figure 4.1: System level architecture of the Up-Down Converter.

The system uses a directional coupler to couple some of the power transmitted by the Wi-Fi Card to a power detector. The latter outputs a DC voltage based on the received RMS power that is used as the input of a comparator. The comparator, based on a reference level, outputs a digital signal enabling the control of the two switches and the shutdown pin of the LNA. One inverter is

used to send the right signal to the controller pin of one of the switches and to the enable pin of the LNA.

The passive mixer is used to downconvert the transmitted RF signal from the 2.4 GHz Wi-Fi band to an IF band centered on a 100 MHz carrier or to upconvert the received 100 MHz IF signal to the 2.4 GHz Wi-Fi band. To do this, a local oscillator (LO) is needed, and is provided by a digital controlled Fractional-N PLL. A Java interface was developed to easily set up the LO frequency and to turn on/off the whole system, eliminating the need to constantly reprogram the digital unit.

Two filters are used: a band-pass filter - to filter intermodulation products of the mixer and some noise generated at the Wi-Fi card; and a low-pass filter - to filter both intermodulation products and non-linear distortion that might occur in the amplification chain.

The two switches are used to enable the use of amplifier modules in the transmission (through the use of a Gain Bock) and reception (through the use of an LNA). This will improve the system performance and increase even more the communication distance.

4.1.1 Design Constraints

There are different constrains attached to this system. Some of them, and the ones that seemed more relevant to describe are shown in the next bulleted list:

- **Underwater vehicle** - It is pretended to implement this module in an AUV which means that it will operate in an underwater environment. Because of that, the electronic modules that will be attached to it have to be fully protected from water. Also it must be as small as possible and energy efficient in order to boost the life time before it has to go up to recharge.

- **Heat** - Temperature also affects the performance of the system as it changes its overall Signal-to-Noise Ratio (SNR). Since this is a module that will consume around 6 W, part of this power will be dissipated as heat and the system must have a way to direct this heat to the water.

- **High PAPR** - The Wi-Fi card implements the standard 802.11n which uses OFDM modulation to send information. This modulation has a high peak-to-average power ratio (PAPR) which has an important role in the Gain-Block and mixer's linearity and efficiency.

- **Switching Time** - The standard 802.11n only allows for a limited switching time of 2 μs. The transition between transmitting and receiving in the Up-Down Converter must then be as fast as possible.

- **Cost** - The budget for this project is limited. As so, the money spent in the design process and in the final board manufacture should be as low as possible. To reduce the cost, it was establish that a low cost FR4 substrate should be used and with only two metalization layers. This is a big constrain due to the many sensible integrated circuits that will be part of the final board, like the phase-locked loop. Also, with only two metalization the RF routing

is much more sensible as was discussed in the section *State of Art*. In order to validate the layout and check the performance of each module in this substrate a self-designed evaluation board was designed for each module.

- **Distance of Communication and Bit-Rate** - The last constraint is more of a functional requirement. The required minimum distance of communication between the AUV and the mining machine for them to communicate in a safe way is 5m, and it must provide a minimum data-rate of at least 2 Mbps.

4.2 Component Selection and Characterization

The Up-Down Converter is composed by different RF modules and each of them should be carefully chosen in order for the system to work and for its performance to be as good as possible. In this section it is described the component selection for the whole system and the reasons for each choice. Then, the process of designing the self designed evaluation boards is described for some of the components ending with the characterization and validation of each of them by measuring their performance through different tests. Note that all the PCBs were designed by using the RF techniques studied in Section 2.5 and it is not the scope of this work to describe all those methods. The photograph of all the individual designed and soldered modules is only shown in Section 4.2.18.

4.2.1 Wi-Fi Card

The chosen Wi-Fi card was the Bullet M2 from Ubiquiti Networks. This choice was based on the fact that this module was already been used on different projects in INESC TEC and not only its good performance is already well known in the community, but also because they were already been bought and available to use.

The Bullet M2 is a compact Wi-Fi card that uses the Wi-Fi standard 802.11 b/g/n. It has an average output power that, depending on the used channel, can go up to 28 dBm, and a sensitivity in the reception that can go as low as -96 dBm. It features a signal strength LED meter for antenna alignment, a low-loss integrated N-type RF connector, and a weatherproof design. It also comes with an intuitive interface that enables the user to easily perform different network measurements. In Figure 4.2 it is shown the model of the Bullet M2.

Figure 4.2: Model of the Bullet M2.

4.2.2 Substrate

The used substrate should be inexpensive and provide a mechanical stability to the whole board. High frequency laminates like the RO4003C or the Arlon laminates, despite having a better electrical performance, are expensive and thin, usually requiring an extra layer of another laminate to provide mechanical stiffness. The high cost of these high frequency laminates together with the increased cost of multilayer stack-up boards is something that should be avoided as much as possible.

Another way of reducing cost is by using less copper layers. Despite the evaluation boards provided by the companies that manufacture the chosen modules all have 4 copper layers, it was decided that the final board should only have 2 layers to reduce cost. This imposes a big limitation as seen in chapter *State of Art* since in this type of layouts that contained a relative high number of interconnected modules, a 2-layer designs require much care with the PCB routing.

Despite the poor performance of the low cost FR4 substrate relative to these high frequency laminates and the harshness in a 2-layer RF design when compared with a 4-layer RF design, it is still possible to design a high performance and low cost PCB for this application by using the presented knowledge in RF layout techniques and by using sophisticated electromagnetic simulation software programs that can guide the process of designing the PCB. The substrate chosen for this PCB was FR4 with 1 mm height, which enables a balance between mechanical stiffness and thin width traces.

Figure 4.3: Substrate used for the final Up-Down Converter board.

4.2.3 Transmission Lines

There are two different RF bands that need to be routed in the system: one for a carrier around 100 MHz and another for a carrier around 2.45 GHz. As mentioned in the Chapter 2 the best technology for RF sensible systems is the CPWG line. To design these lines, the first step was to use the tool *Controlled Impedance Line Designer* from ADS, Keysight, to calculate the width of the trace and the gap between the trace and the adjacent ground fills. After having the theoretical values, a layout optimization using Finit Element Method (FEM) simulation was performed to find the actual best dimensions in order to improve the performance of the lines.

Several ground vias were placed to connect the top ground plane to the bottom one. The vias are used in order to have a very low impedance ground at the operating frequency of the line, otherwise it will not act like a ground for the RF signal and start to act more like a stub. Since a stub starts to be a problem as it approaches 1/8 of a wavelength, vias should be used with at least

1/8 of a wavelength apart. The wavelength of a 2.45 GHz signal on a CPWG line can be calculated by using the follow equation,

$$\lambda_{\text{CPWG}} = \frac{c}{f\sqrt{\varepsilon_e}}, \tag{4.1}$$

where ε_e is the effective dielectric constant that was measured by using again the *Controlled Impedance Line Designer* tool, and is equal to 2.8. Having that comes,

$$\lambda_{\text{CPWG}} = \frac{3\times10^8}{2.45\times10^9\times2.8} \approx 44 \text{ mm} \rightarrow \lambda_{\text{CPWG}}/8 = 5.5 \text{ mm}. \tag{4.2}$$

Even though the minimum distance between vias to avoid bad grounding problems is around 5.5 mm, it was decided to put them spaced by just 1 mm for an increased performance.

The layout of the improved CPWG lines for 2.45 GHz and 100 MHz are shown in Figure 4.4 and 4.6 respectively. The arrows at the left and right corners are the edge pin ports used in ADS to measure the S-Parameters. The 2.45 GHz line has a width of 1.5 mm and a gap of 0.61 mm while the 100 MHz line has a width of 1 mm and a gap of 0.25 mm. The simulation was done to a 40 mm length line and the results are shown in Figure 4.5 and Figure 4.7 for the 2.45 GHz line and 100 MHz line respectively.

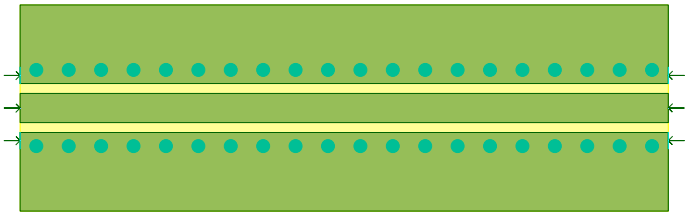

Figure 4.4: Layout of the improved CPWG for 2.5 GHz using ADS from Keysight.

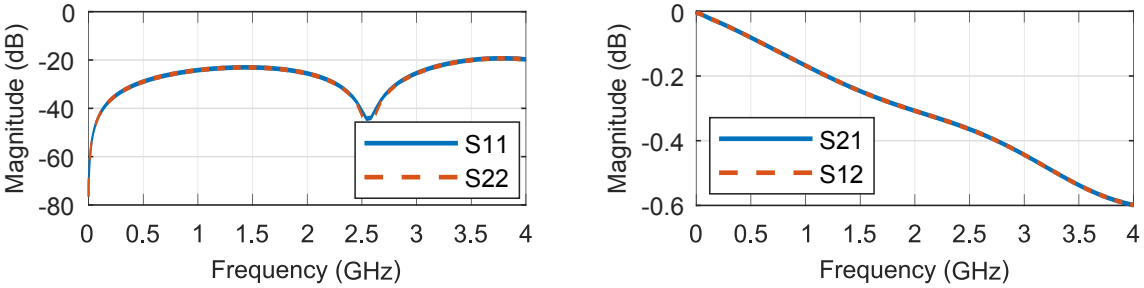

Figure 4.5: Final results obtained in the simulation of the improved CPWG for 2.5GHz.

It is observed that the 2.45 GHz line is very well matched and acts as a 50 Ohm line since the $|S_{11}|$ parameter is below -20 dB which means that less than 1% of the power is reflected back at the input port. The $|S_{21}|$ is as high as expected for a low cost FR4 substrate with a tangent loss of 0.01.

The CPWG designed for 2.45 GHz works very well for the 100 MHz frequency as expected since the increase in frequency brings more parasitic effects on the lines. Despite that, for the IF

frequency the width of the line could be decreased and still maintain a very good matched line, which was the adopted solution because of routing easiness on the final board.

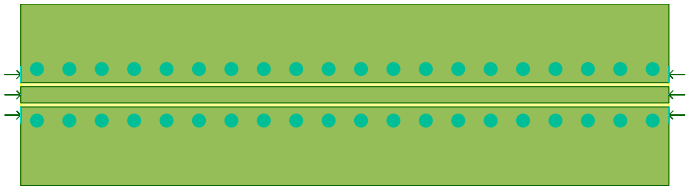

Figure 4.6: Layout of the improved CPWG for 100 MHz using ADS from Keysight.

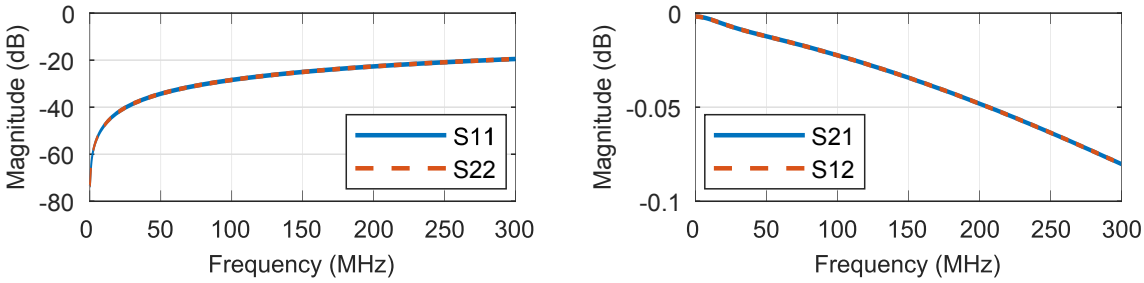

Figure 4.7: Final results obtained in the simulation of the improved CPWG for 100 MHz.

For the 100 MHz CPWG line the results showed that the $|S_{11}|$ is lower than -20 dB for the frequency of interest and the $|S_{21}|$ is better than the one designed for high frequency as expected by the increase in losses with an increase in frequency.

4.2.4 Connectors

The connector is the component that makes the interface between the Wi-Fi card and the RF Port, and between the Antenna and the IF Port.

The chosen connector was the SMA 142-0711-881 SMA from Cinch Connectivity Solutions. This choice was made because there were already a couple of this SMA connectors ready to use in INESC TEC and they have a very good performance at this frequency.

In order to accurately model this transition between the SMA connector and the CPWG transmission lines and improve its performance a 3D simulation and optimization was performed using HFSS software from ANSYS. Two different versions were simulated, one using the traditional connection (Figure 4.8b) and another by means of a tapper used in different boards from Analog Devices (Figure 4.8a). Several vias were also placed on the pads of the connector to reduce parasitic effects on the pad by reducing the inductance between the top and bottom ground planes near the transition.

It was verified through simulation that as the tapper height and width were increased, within some limits, and ensuring that the bottom ground plane that is bellow the tapper was removed (Figure 4.10b, this transition could be improved. Through optimization it was possible to improve the $|S_{11}|$ parameter from -28 dB to -32 dB at the frequency of interest as shown in Figure 4.9.

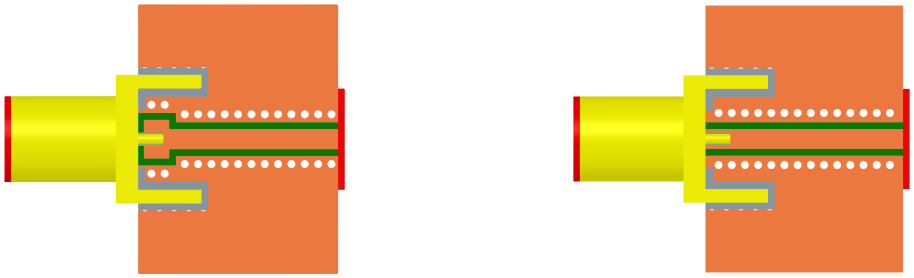

(a) (b)

Figure 4.8: Two different approaches to perform the transition between the SMA and the PCB board.

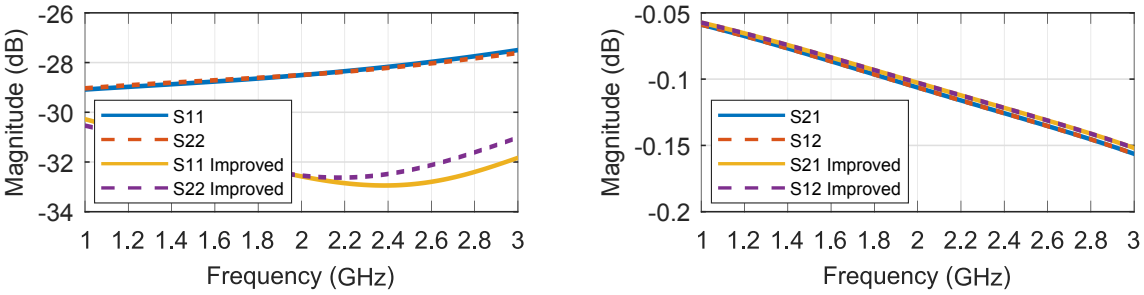

Figure 4.9: Comparison between the S-Parameters of the two approaches for the connector-to-board transition.

An illustration of the simulated improved transition is show in Figure 4.10. The tapper height is 2.3 mm and the width is 3.5 mm. Despite the improvement obtained was not significant it was decided to use this transition for the self-designed evaluation boards as an academic prove of concept.

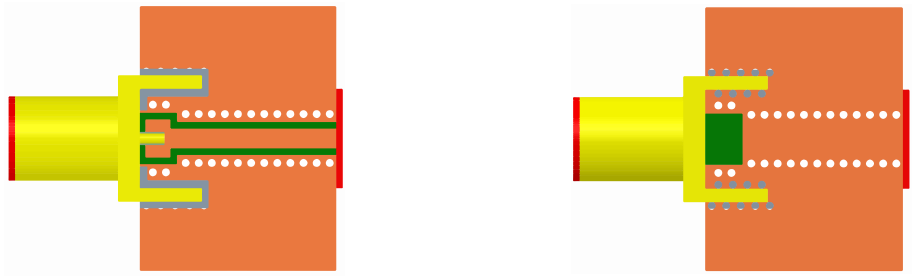

(a) (b)

Figure 4.10: Illustration of the improved transition used in the individual module design.

4.2.5 Coupler

The coupler is used to route some of the RF power transmitted by the Bullet M2 to the power detector presented in Section 4.2.6. For this task a relatively low cost directional coupler from

Mini-Circuits (D17IA+) was used. This coupler has a typical 0.4 dB insertion loss, 17.1 dB nominal coupling, 14 dB directivity and a typical return loss higher than 16 dB in all the ports.

Different views of the 3D model of the designed coupler board are shown in Figure 4.11.

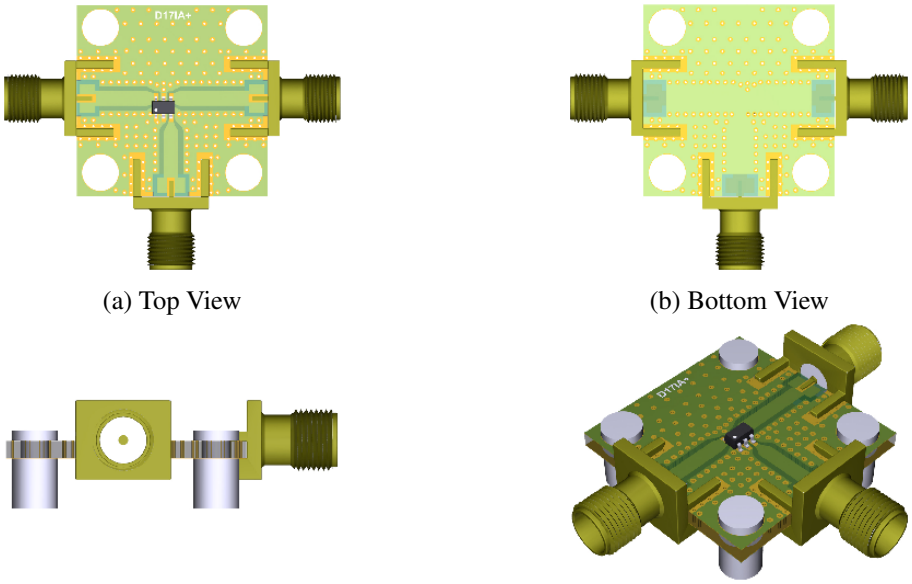

(a) Top View (b) Bottom View

(c) Side View (d) Isometric View

Figure 4.11: Different views of the designed coupler board.

4.2.5.1 Measurements

After the process of soldering the board, it was time to measure the values of the insertion loss, return loss, coupling and directivity of the designed coupler board. All this results were obtained by using a VNA and measuring the S-Parameters as shown in Figure 4.12. The port 1 is the input port, the port 2 is the output port and the port 3 is the coupled port. The obtained results are shown in the Figure 4.13.

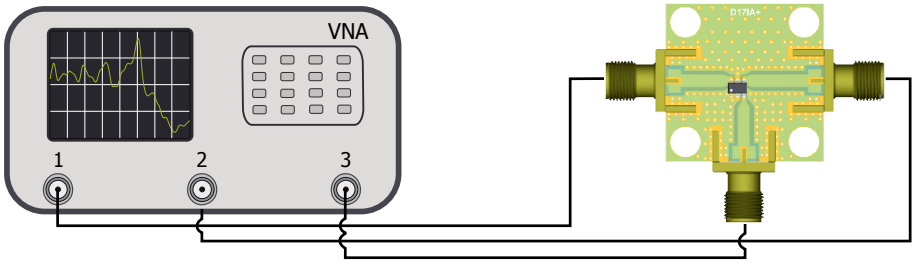

Figure 4.12: Illustration of the measurement setup for the coupler board.

The insertion loss (given by $|S_{21}|$) is around 0.6 dB and increases as a function of frequency but at a relatively low rate. The coupling gives us the ratio of power that is coupled to the coupling port and is given by the $|S_{31}|$ and is around -17 dB at the frequencies of interest. The directivity is the figure of merit that defines how well a coupler discriminates between forward and reverse

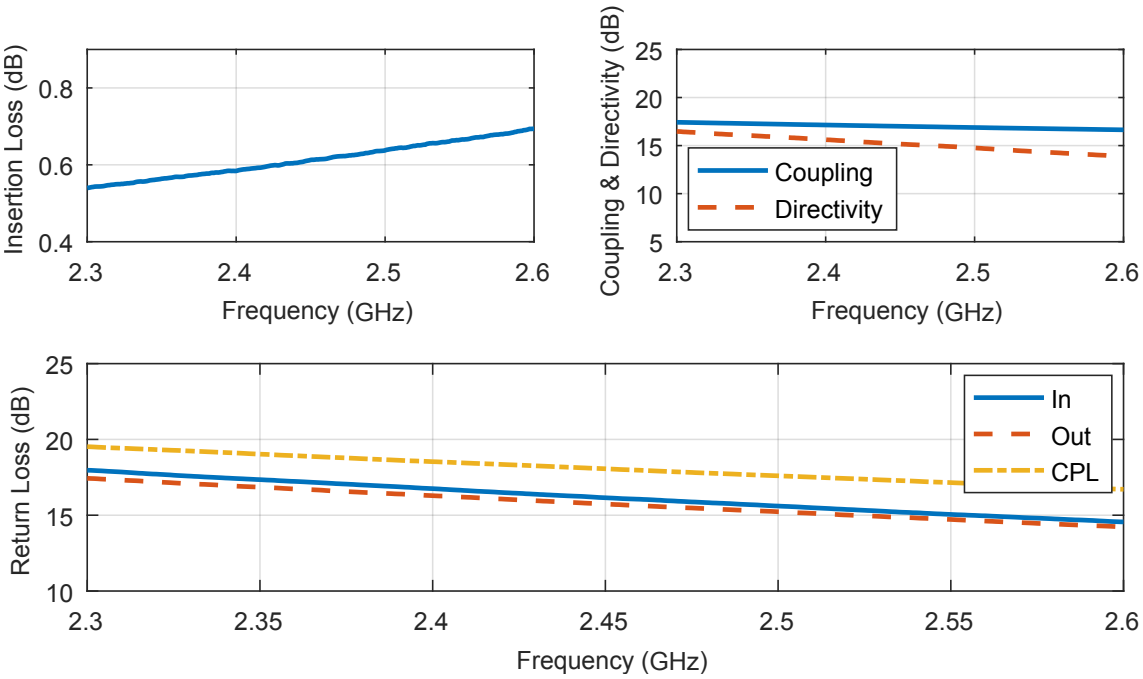

Figure 4.13: Obtained results for the different measurements to the coupler board.

waves and was measured by using the following equation given by [29],

$$D = S_{31} + S_{21} - S_{32}, \tag{4.3}$$

where in our case, despite the value is not very high (around 15 dB), it is good enough for the detector and comparator presented in Section 4.2.6 to distinguish between the transmitted and received signal.

On the other hand, the return loss ($|S_{11}|$, $|S_{22}|$, $|S_{33}|$) decreases as a function of frequency but for the three ports it is higher than 15 dB which means that all the ports are well matched to 50 Ohm.

Although the values have shifted a little from the ones stated in the datasheet, which can be explained by the fact that this measurements were performed to a embedded coupler, they were very similar, as expected, since the length of the CPWG lines were very small.

4.2.6 Detector and Comparator

The detector is used to sense the power that is coupled and output a DC voltage accordingly to its input power. This DC voltage is used as the input of the comparator that will compare that voltage with a threshold voltage (provided by external circuitry) and output a digital signal voltage of 5 V or 0 V, depending if it is in receiving mode or in in transmitting mode respectively. These signals are used to control different components as will be discussed in the succeeding sections.

The chosen component for the power detection task was the HMC602 from Analog Devices. This power detector operates from 1 MHz up to 8 GHz and delivers an high dynamic range and

conversion accuracy over the whole range. It also provides very fast transitions that can be controlled by changing the capacitance selected for the CLPF pin which is the pin used for the output ripple filtering.

The comparator used was the LMV7219 from Texas Instruments which is a low power and high speed comparator with internal hysteresis that can achieve transitions in the order of 7ns. The hysteresis is useful to deal with some unwanted noise that might be present in the comparator input pin.

Different views of the 3D model of the designed power detector and comparator board are shown in Figure 4.14.

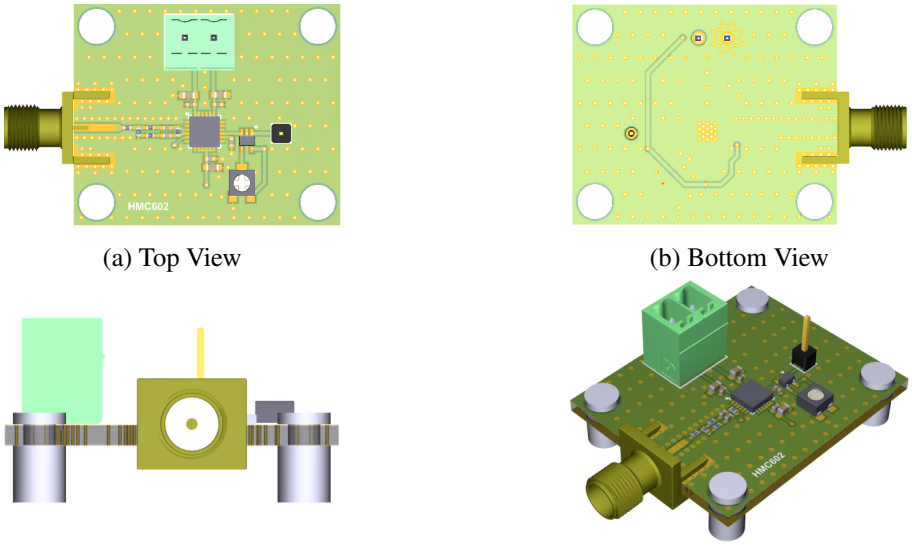

(a) Top View (b) Bottom View

(c) Side View (d) Isometric View

Figure 4.14: Different views of the designed detector and comparator board.

Despite the designed board was ready for manufacture, this was not done since there were already an evaluation board bought for the comparator. This board was manufactured in Rogers substrate with a FR4 substrate behind to give some mechanical stiffness. Despite those differences, it was established that the board was good enough to evaluate the performance of the detector used in the final board. There was no tests performed to the comparator board.

4.2.6.1 Measurements

Two measurements were done to the evaluation board of the power detector (Figure 4.15). The first one consisted in evaluating the output voltage based on the input power for two different signals: a simple sinewave, and a Wi-Fi 802.11/n OFDM signal. This measurement will show how the comparator react to these different signals and will define which DC voltage should be used as the reference voltage of the comparator. The second one consisted in turning on and off the applied OFDM input signal and check its response in the oscilloscope. This last measurement was done for different values of the loop filter capacitor.

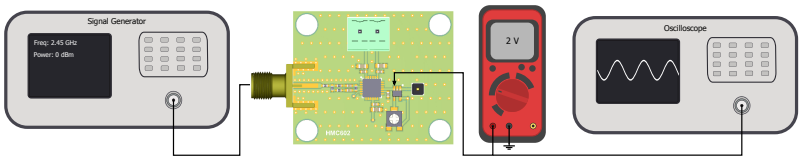

Figure 4.15: Illustration of the measurement setup for the detector board.

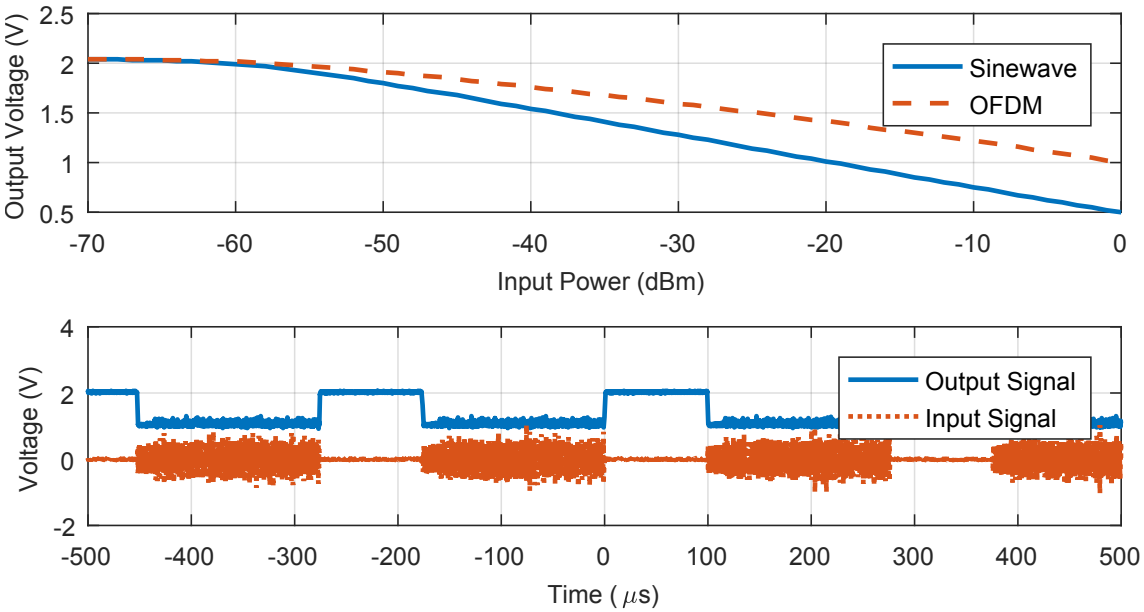

Figure 4.16: Obtained results for the different measurements to the detector board.

Figure 4.16 shows the obtained results for a loop filter capacitor of 150pF. It shows that if no signal is applied to the input port, the power detector outputs 2V as stated in the datasheet. As the input power is increased, for values above -60 dBm, the output voltage starts to decrease with a higher slope for the sinewave signal than for the OFDM signal. For a -20 dBm coupled Wi-FI signal, the comparator will output a DC voltage of around 1.5V. The reference voltage should be in the middle step which, in this case, is 1.75V.

For the second test, the compromise in terms of ripple filtering and rise/fall time was obtained for a loop filter of 150pF which corresponds to an output bandwidth of 505kHz. The measured rise and fall time were around 520 ns and 620 ns, respectively, and this was the best option in terms of a clean/fast output signal.

4.2.7 Inverter

The inverter was used to have both the logic high (5V) and logic low (0V) appearing simultaneously in the system. This is required since each of the switches need opposed control signals from each other as it is shown in the Section 4.3. Another reason is that when the bullet is transmitting the comparator will output 0V, and the LNA shown in section 4.2.14 is turned off with 5V, needing a 180^o phase shift on this control voltage.

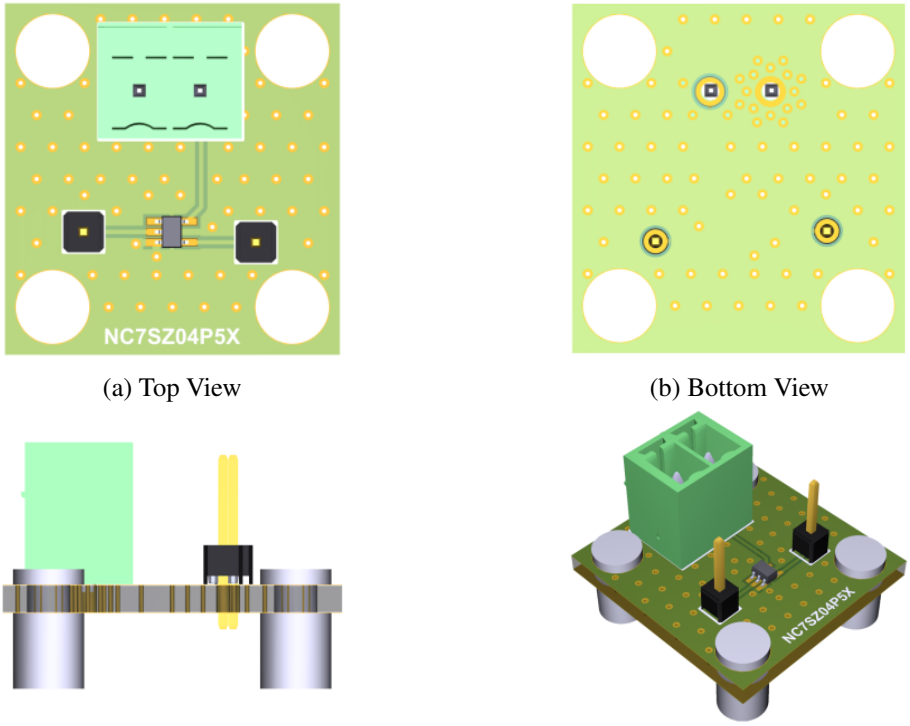

(a) Top View (b) Bottom View

(c) Side View (d) Isometric View

Figure 4.17: Different views of the designed inverter board.

For these needs, the inverter chosen was the NC7SZ04P5X from ON Semiconductor which is a fast inverter with typical rise and fall times of 5 ns.

Different views of the 3D model of the designed inverter board are shown in Figure 4.17.

4.2.7.1 Measurements

Only one test was performed to this board, which consisted in sending a 2.8 kHz input signal and verify if the output was inverted, and calculating its rise and fall times using the setup illustrated in Figure 4.18. The frequency chosen is higher than the usual switching time of the Wi-Fi 802.11n standard. The results for this measurement are shown in Figure 4.19.

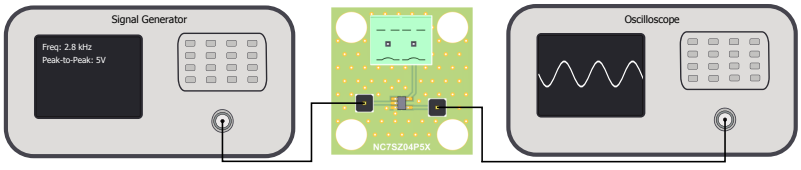

Figure 4.18: Illustration of the measurement setup for the inverter board.

It is observed that the digital signal is in fact phase shifted. Despite not shown due to the scale of the graph, the rise-time and fall-time are both 5ns. There was also some overshoot and ringing on the falling edge of the signal that can be eliminated with a parallel RC circuit at the output of

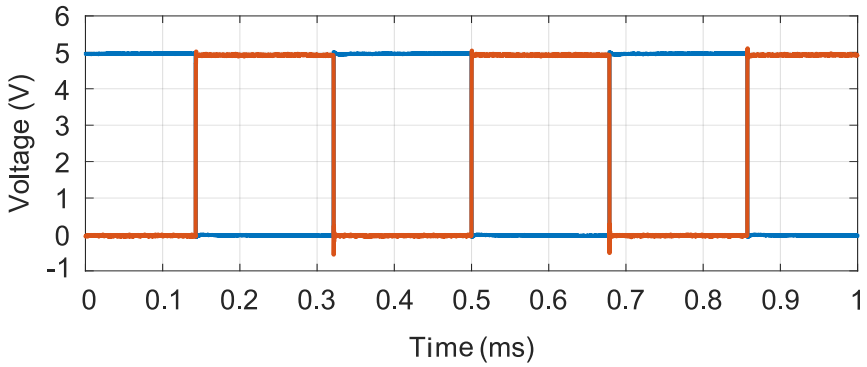

Figure 4.19: Obtained results for the measurement of the inverter board.

the inverter pin. This circuit, despite filtering those effects, increases the rise and fall time of the inversion.

4.2.8 Mixer

The mixer is the heart of the Up-Down Converter. As was discussed in section 2.6 the mixer is a three port device is responsible for downconverting the signal when the Bullet M2 is transmitting, and upconverting when the Bullet M2 is receiving. The same mixer should work in transmission and reception, arising the need for a passive mixer with high linearity in order to handle the high input/output power of the transmitting mode. A mixer with low conversion loss and low noise figure is also required to improve the system's performance.

The best mixer found that matches all these requirements was the HMC689 from Analog Devices. This mixer meets all the frequency requirements for each port with matched ports (Input Return Losses around 14 dB), a typical conversion loss of 7.5 dB, and a noise figure of 7.5 dB. The typical isolation between ports are around 30 dB.

The only concern about this mixer is that, despite having a high P1dB compression point of 24 dBm, it is not linear enough to handle the maximum power of the Bullet M2 without starting to distort the OFDM signal. Since no better choice was found, this was the option used, having in mind that the output power of the Bullet M2 has to be limited. These calculations are shown in Section 4.3 when presenting the final designed Up-Down Converter board.

Different views of the 3D model for the designed LNA board are shown in Figure 4.20.

4.2.8.1 Measurements

To evaluate the results and the performance of this mixer, the first step consisted in identifying which frequencies are used in each port. Starting for the RF port, it deals with the Wi-Fi OFDM signal that goes from 2.4 GHz to 2.5 GHz approximately, depending on the channel used. The LO port is settled in order for the IF frequency to be centered at 100 MHz, this means that the typical frequencies that are routed to the LO port will be from 2.3 GHz to 2.4 GHz. The IF routes the signal that goes underwater, which has a maximum bandwidth of 20 MHz, centered around a 100 MHz carrier frequency.

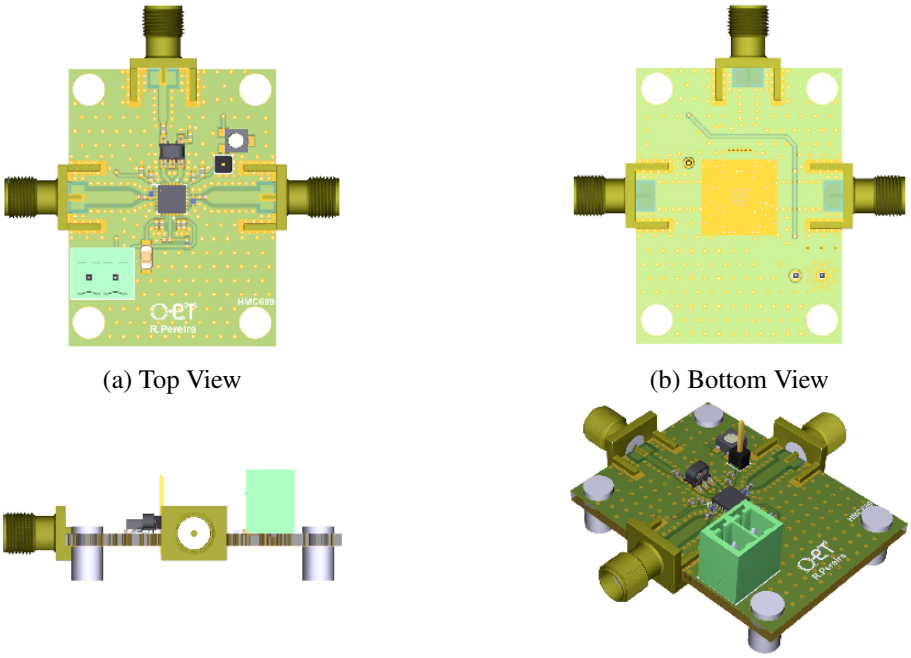

(a) Top View (b) Bottom View

(c) Side View (d) Isometric View

Figure 4.20: Different views of the designed mixer board.

After settling the frequency sweep in all the ports, different measurements were done to the mixer's board by using the VNA as ilustrated in figure 4.21.

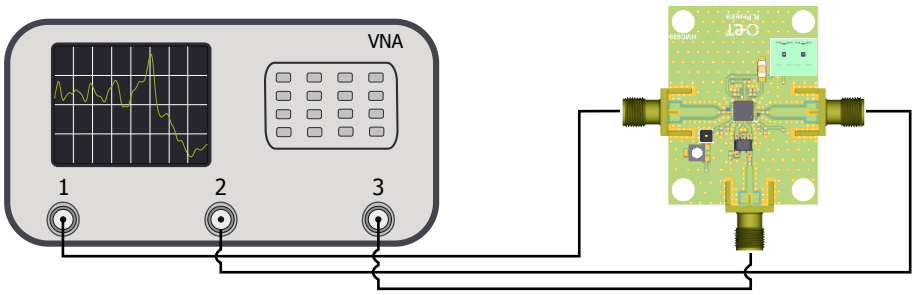

Figure 4.21: Illustration of the measurement setup for the mixer board.

The first one was to use the VNA to measure the return losses and isolation between the different ports. Then it was measured the conversion loss when the mixer is upconverting and when the mixer is downconverting. The different obtained results are shown in Figure 4.22, and it is observed that, despite the matching on the RF port is degraded as the frequency increases, both the RF and LO ports are matched for the needed frequencies.

In terms of isolation, the values obtained were the ones expected and described in the datasheet. The results show a typical isolation of 40 dB between the LO and the RF port which is very important since these frequencies are close to each other in the frequency spectrum.

The typical conversion loss was measured by fixing the LO frequency, and by changing the RF frequency (to measure the donwnconverting conversion loss), or the IF frequency (to measure

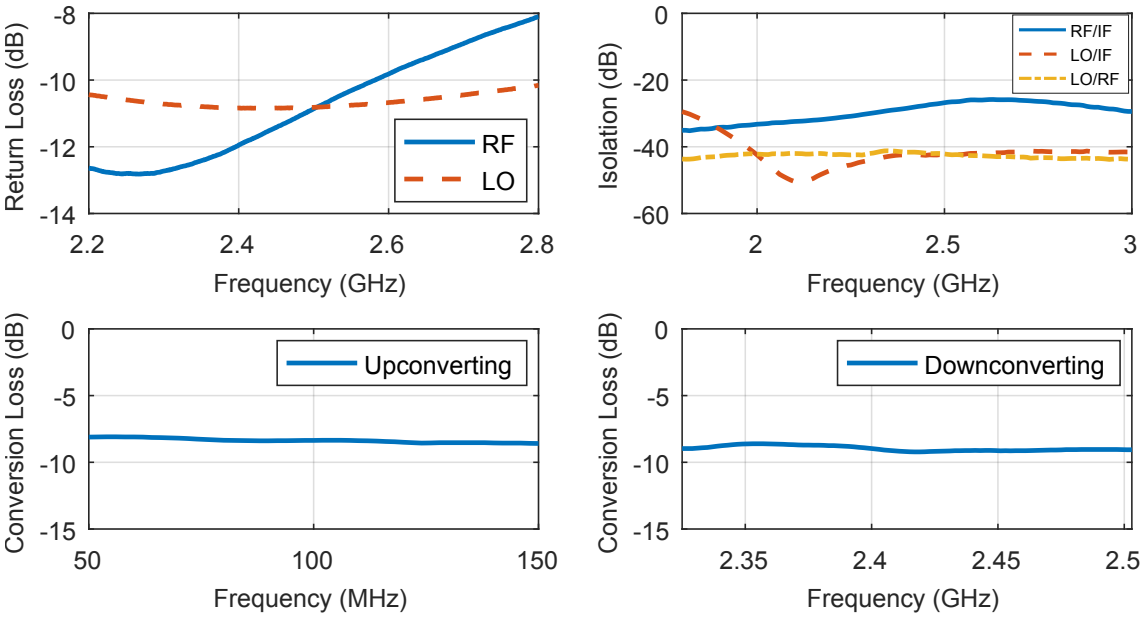

Figure 4.22: Obtained results for the measurement to the mixer board.

the upconverting conversion loss). The typical values obtained were 8.3 dB for the upconversion and 9 dB for the downconversion. These values are a slightly higher than what was expected from the datasheet but these differences are acceptable since we are dealing with high frequencies and these values were not de-embedded.

4.2.9 Phase-Locked Loop

The phase-locked loop (PLL) is used to set up the local oscillator of the mixer, and therefore is used as a synthesizer. There are 21 different frequencies that can be used as the carrier frequency in the IEEE standard, ranging from 2.412 GHz to 2.474 GHz which means that if the desired mixer's output IF frequency is 100 MHz, then the PLL must be able to synthesize frequencies from 2.312 GHz to 2.374 GHz.

The performance of the local oscillator in a receiver design is very important and requires caution to ensure that there are no spurious signals that might create unwanted multiplication at the mixer or even interfere with the performance of other integrated circuits in the board. The local oscillator should be stable across all the temperatures expected to the board and provide enough output power to drive the subsequent mixer. The phase noise is one of the critical parameters of the PLL since in OFDM systems it will often limit the maximum noise power ratio of the receiving system as shown in [30].

The HMC832 from Analog Devices was chosen to perform this task. This is a 3.3V, high performance, wideband, fractional-N PLL that features an integrated VCO that covers the frequencies from 1500 MHz to 3000 MHz. It has an integrated phase detector and delta-sigma modulator that allow wider loop bandwidths and faster frequency tuning with very good spectral performance. The phase noise and spurious performance are industry leading as stated in the datasheet, and it

has a very low noise floor (-160 dBc/Hz) which eliminates any contribution to the mixer's noise floor. The output frequency is digitally controlled as well as the output power with a maximum of 7 dBm. It has an output mute mode that will be used to digitally turn on/off the PLL using the interface shown in Section 4.2.11.1.

To power up the HMC832 a very low noise power supply is needed and for that task the HMC1060LP3E, also from Analog Devices, was chosen. It is a BicMOS ultra low noise linear voltage regulator targeted for these applications that requires high levels of power supply isolation. It can supply up to 500mA of current distributed between four independent pins which enables it to supply all the power needs of the HMC832 and also the TCXO reference presented in section 4.2.10.

4.2.9.1 Design

Designing all the layout and all the programming code for the HMC832 was one of the most challenging tasks in this master's work. To help achieving this goal, the HMC832's evaluation board's schematic was used as a guideline. The first step was to go through the datasheet and the evaluation board's schematic to understand what could be removed and what could be critical in the performance of this integrated circuit.

The first problem arising was that Analog Devices' engineers stated as "critical" that the substrate used to separate the top and bottom layers should be Rogers4003 or Arlon25 which are high frequency substrates. Another problem was that their layout was done in a board containing 4 copper layers, and in our case it is desired to keep it as a two layer board for minimizing production costs. A very carefully design had to be done in order for the PLL to work properly and with the expected performance needed for a LO transceiver system.

The first step of the layout was to route the RF paths and the loop-filter since these are the most sensible areas of the design. The output frequency of the PLL was connected to an SMA connector though a direct CPWG line, and the same was done to the reference input pin. The loop filter was designed for a 50 MHz PD reference frequency with a loop filter bandwidth of 127kHz and a loop filter phase margin of 61^o. These values were chosen since they provide the best performance in terms of phase noise as stated in the datasheet. The layout of the loop filter was performed with two main objectives. The first was to minimize the distance between the charge pump (CP) pin and the VTUNE pin of the HMC832 which are the two pins that interconnect the loop filter feedback. The second and more important objective, was to locate it as close as possible to the CP pin since the first components of the loop filter deal with higher frequencies signals than the final ones, where the signal is already smoothed into a close to DC signal by the filter.

The low noise performance on all of the VCC pins was guaranteed with bypass and decoupling capacitors with the values recommended in the datasheet and with the usual features recommended for these tasks. The low noise was also guaranteed by using the recommended layout for the HMC1060.

To access the SEN, SDI, SCK and SDO pins of the HMC832, which are the pins used to digitally control the PLL, straight lines to a 6x2 header were used for future connecting the Arduino. An 1x1 header was also used to check the 3.3V line that supplies supply the TCXO.

As always, shielding vias were used on the RF CPWG lines as well as stitched vias through all the board and on the ground paddle of the integrated circuit to reduce as much as possible the ground inductance. With exception for the high capacitance bypass capacitors, all the components used were 0402 to avoid unexpected parasitic effects.

Different views of the 3D model for the designed PLL board are shown in Figure 4.23.

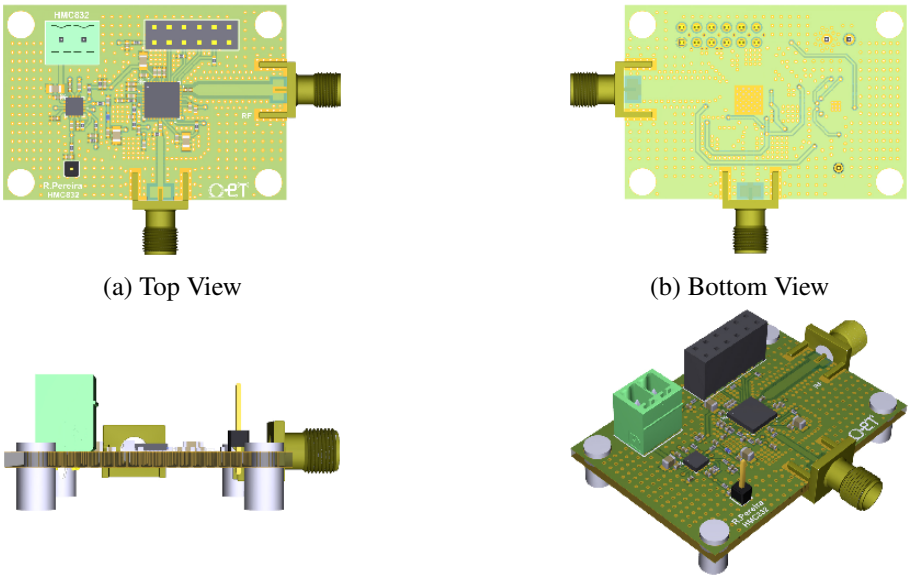

(a) Top View

(b) Bottom View

(c) Side View

(d) Isometric View

Figure 4.23: Different views of the designed PLL board.

4.2.9.2 Measurements

Using the Arduino Mini Pro board and the developed code presented in Appendix A it was possible to check the performance of the PLL for the different frequencies that were used for the LO to properly up/down convert the signal. The code provided sets the PLL to be at the high performance mode and in the exact frequency mode, which are the modes for improved noise floor and with 0 hertz frequency error respectively.

Two different measurements were done to the PLL board:

- The first one was to validate the arduino code, the reference and the PLL as a system by programming the Arduino to set the output frequency of the PLL to different values and to validate, by using a spectrum Analyzer as illustrated in Figure 4.24, that indeed this system works.
- The second one was to measure the phase noise by using the same system presented in the previous point.

The results obtained for the first measurement (for an output frequency of 2.312 GHz) are shown in Figure 4.25. It is verified that the PLL has a very good performance with a low phase noise.

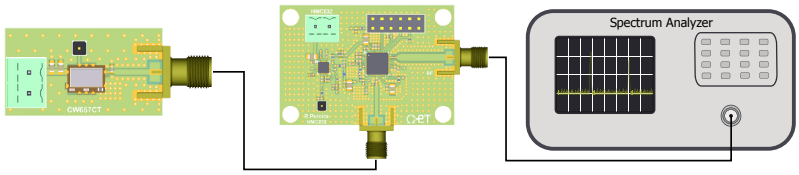

Figure 4.24: Illustration of the measurement setup for the PLL board.

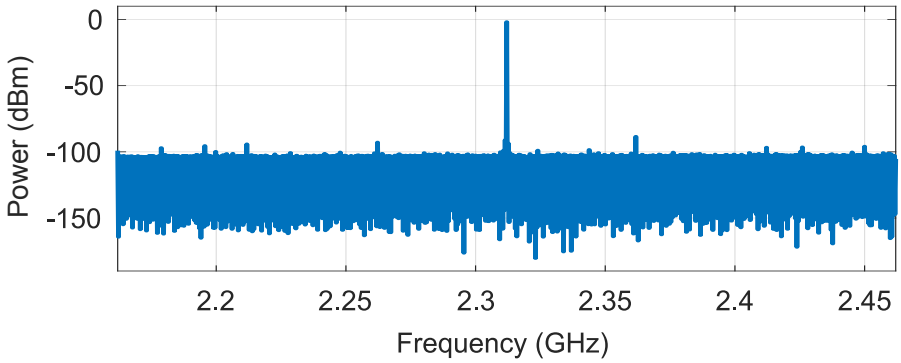

Figure 4.25: Obtained results for the measurement to the PLL board.

4.2.10 TCXO

The TCXO will be used to set up the reference frequency to the PLL. As mentioned before, the loop filter of the PLL was designed for a reference frequency of 50 MHz, meaning that this is the frequency of the TCXO. The reason to buy a TCXO (Temperature Compensated Crystal Oscillator) instead of a simple crystal oscillator was that the TCXO provides much higher levels of temperature stability than are possible with a normal crystal oscillator. A good, high quality and low-phase-noise reference is then crucial to have a stable low-phase-noise RF output. A square wave or clipped sine wave usually offers excellent performance because of its sharper clocking edges that allow for a lower phase jitter at the output.

For this task, the D75J-050.0M from Connor-Winfield was chosen. This is a TCXO with a LVCMOS clipped sinewave output which can hold 1-ppm stabilities over the 0 to 70^{o}C temperature range.

Different views of the 3D model for the designed TCXO board are shown in Figure 4.26.

4.2.10.1 Measurements

Two simple measurements were performed to this board: one to show the signal in its time domain and another to show it in its frequency domain. Those results are shown in Figure 4.28

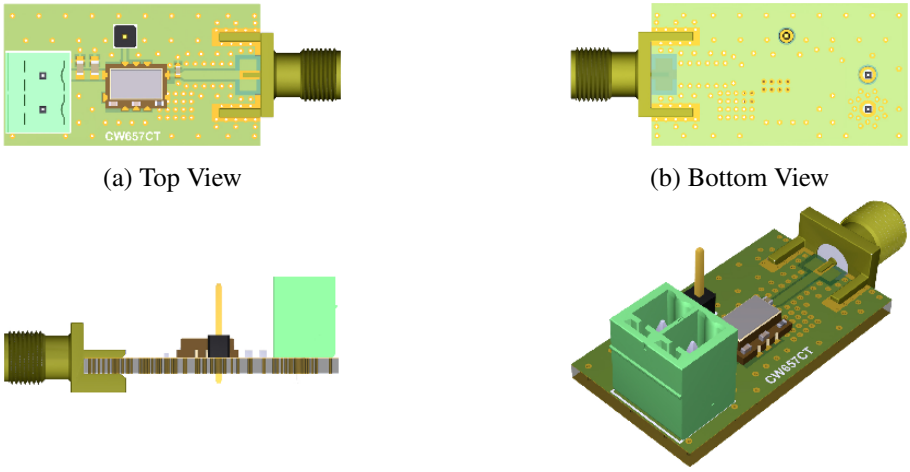

(a) Top View (b) Bottom View

(c) Side View (d) Isometric View

Figure 4.26: Different views of the designed TCXO board.

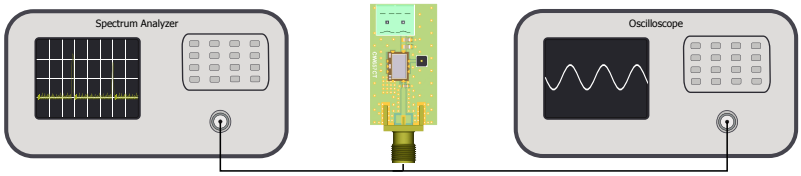

Figure 4.27: Illustration of the measurement setup for the TCXO board.

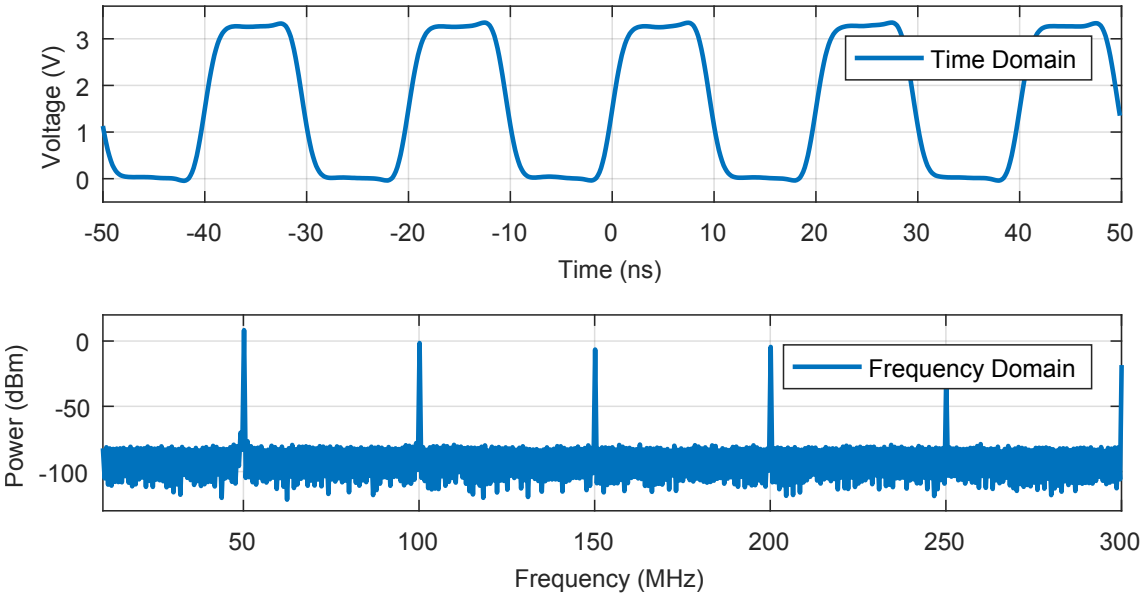

Figure 4.28: Obtained results for the measurement to the TCXO board.

As can be seen, the output has a LVCMOS format and its frequency is 50 MHz. The figure also shows the expected harmonics as expected by this wave format.

4.2.11 Digital Unit

The Arduino Mini Pro was used to digitally control the output frequency of the PLL and to turn on and off the whole system using the user interface shown in Section 4.2.11.1. Of the 14 digital input/output pins of the ATmega328p only 6 were used: 5 to control the PLL, and 1 to control the enable pin of the LDO. The board comes with a six pin header that allows the connection of an FTDI cable to provide USB power and a serial communication to the board. There are two version of the Pro Mini: one that runs at 3.3V and 8 MHz, and another at 5V and 16 MHz. For power supply simplicity, the one designed in this project was the 5V one.

Even though the self designed arduino board was designed and manufactured, it was not included in the final board for layout simplicity and to enable different ways to program the board and not just by using the arduino programming language. Instead the original Arduino Mini Pro board will be connected though 1x6 header connector. For that reason, this subsection ends with the 3D model for the designed Arduino board shown in Figure 4.29.

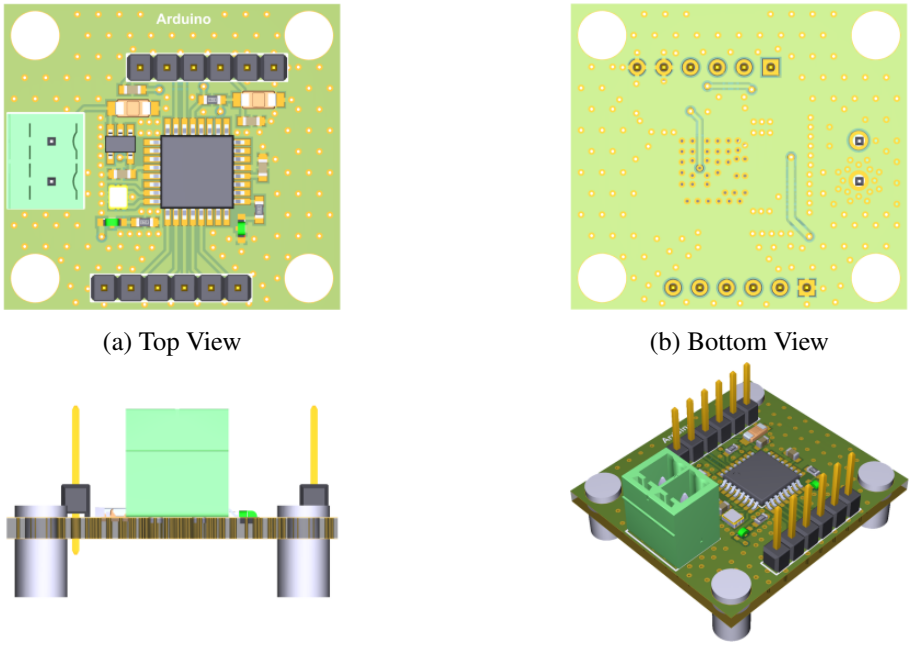

(a) Top View

(b) Bottom View

(c) Side View

(d) Isometric View

Figure 4.29: Different views of the designed arduino mini pro board.

4.2.11.1 Interface

One of the goals was to turn this system simple to use. The long self-developed Arduino code that is provided in the Appendix A of this master thesis is complex for someone that does not read the datasheet of the PLL or does not know arduino programming language. For this reason, a simple java program with only two menus was developed.

The first window is presented when the user starts the program, as shown in Figure 4.30a. This window has a logo developed for this interface, the logos of the different project partners evolved

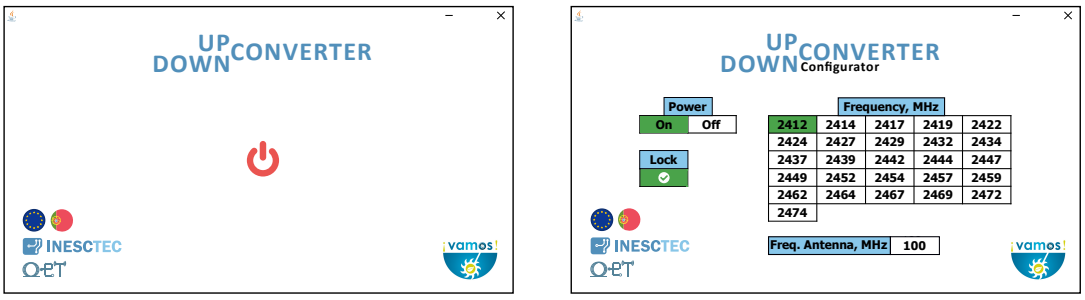

(a) First Panel (b) Second Panel

Figure 4.30: Java interface used to select the frequency of the PLL and to turn on/off the system.

in the project and a start button. When this button is pressed, the program verifies if there is a serial port connection to the Arduino and, if so, a second window is presented, as shown in figure 4.30b, otherwise, it remains in the same window.

The second window is basically a control room for the Up-Down Converter system. Four actions can be done in this menu:

- **Turn On/Off** - By using a digital output pin of the Arduino connected to the enable pin of the LDO, it is possible to power down or power up the Up-Down Converter system.
- **Check LOCK** - By digitally measuring the voltage in the pin that connects to the SDO pin of the PLL it is possible to check if the PLL is locked or not. By doing this we can safely say if the board is working properly since this is the most sensible part of the system.
- **Change the Wi-Fi carrier frequency** - By double clicking in the buttom of one of the different frequencies available the program automatically calculate the frequency needed at the LO based on the frequency chosen to the antenna and sends the respective information to change the frequency;
- **Set up the IF frequency needed** (frequency of the antenna that will be connected to the IF port of the system) - This is done in the same way as explained in the previous point.

All of the communication protocol was established by using the RXTX Java library available in the Arduino website.

4.2.12 Switch

The switch is needed to allow the use of amplifier chains both in the reception and transmission. Two different paths are needed: one to route the received signal through a low-noise amplifier; and another to route the transmitting signal through a gain block. An SPDT with very good isolation and high linearity is then needed.

The chosen IC for this task was the HMC349ALP4CE from Analog Devices, which is a GaAs MESFET SPDT switch with high isolation and is non-reflective from DC to 4 GHz. The switch

has more than 70 dB isolation between all the ports at 100 MHz and a low 0.9 dB insertion loss. The switching speed is also low, with typical values of 150ns.

Different views of the 3D model for the designed switch board are shown in Figure 4.31.

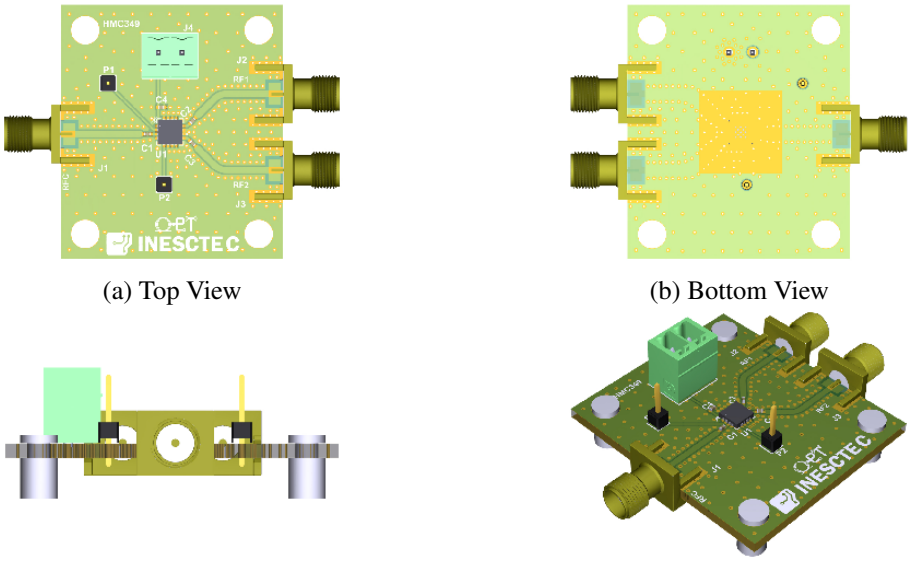

(a) Top View (b) Bottom View

(c) Side View (d) Isometric View

Figure 4.31: Different views of the designed switch board.

4.2.12.1 Measurements

Three different types of measurements were done to the switch boards by using the VNA and measuring the s-parameters of this 3 port device as ilustrated in figure 4.32.

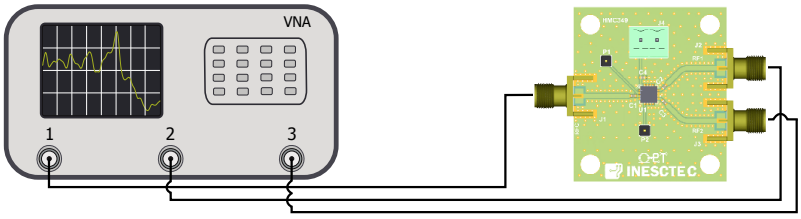

Figure 4.32: Illustration of the measurement setup for the switch board.

The first one was the insertion loss between the common RF input (RFC) and the two individual RF outputs (RF1, RF2). As can be seen in Figure 4.33 the insertion loss is around 0.9 dB.

Then the return loss in all the three ports was measured for the two different control voltages available. The return loss of the common RF port and the two enabled RF outputs is below -20 dB which means that the switch is very well matched at the working frequencies. When the RF outputs are disable the return loss is around -6 dB which means that at the switch does not internally switch to an exact 50 Ohm resistor at this frequencies.

In terms of isolation it was seen that all the ports are very well isolated between each other with typical values bellow -70 dB which is very good since the goal is to isolate both the amplifiers as much as possible to avoid any feedback loop in this system.

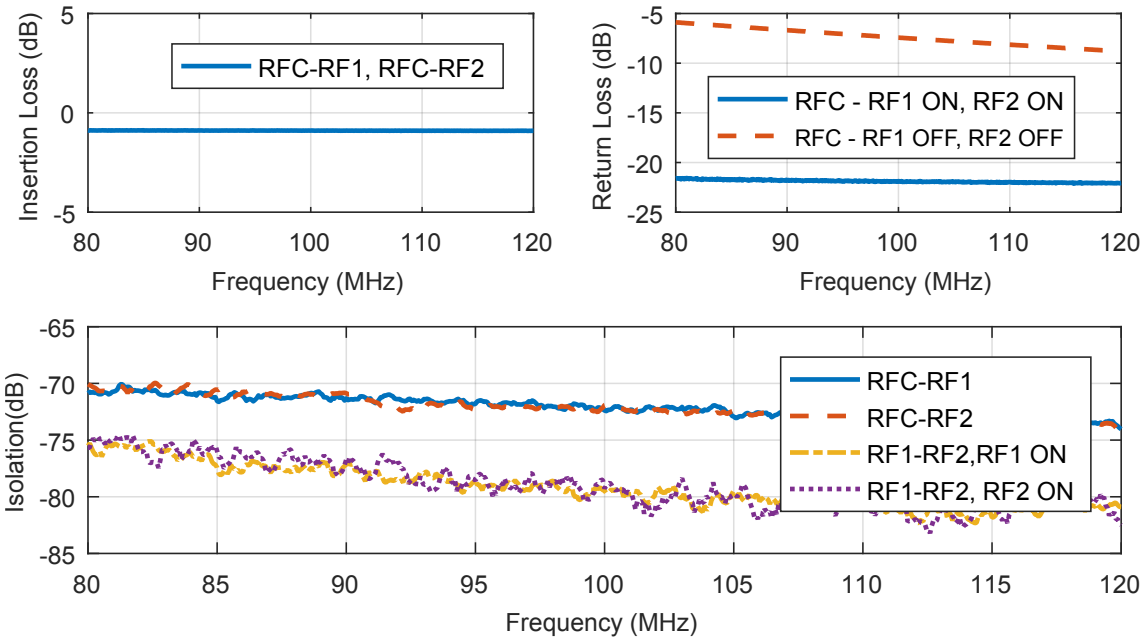

Figure 4.33: Obtained results for the measurement to the switch board.

There was some difficulties in measuring the P1dB point for the switch. In an attempt to understand if the switch could distort the signal, we use the gain block output shown in section 4.2.13 that have a linearity of +25 dBm as well be shown, and check if this signal was distorted by the switch. The result was that this signal had no distortion, so we conclude that the input P1dB is higher than +25 dBm, and so its performance is good for this application.

4.2.13 Gain Block

The gain block will be used to improve the output power transmitted to the underwater medium. Instead of a power amplifier that could degrade the performance of the rest of the board and also would consume to much power, it was decided to use a gain block. The expected main goal for this component is then to compensate the conversion loss of the mixer and if possible improve the output power with a low power consumption.

There was a lack of gain blocks with high linearity for this frequency in the market. The best one found for this task was the TQP7M9105 from Qorvo, which is a InGaP / GaAs an amplifier with high linearity and high gain that delivers good performance across a wide band of frequencies depending on its matching network. The TQP7M9105 also features a dynamic active bias circuit that enable stable operation over bias and temperature variations. The company provides the S-Parameters which were used to match the component and improve its performance for the frequencies of interest as shown in the next section.

4.2.13.1 Design

The chip itself is completely unmatched at 100 MHz with an $|S_{11}|$ of -1.08 dB and a $|S_{22}|$ of -3.00 dB. To match the amplifier, the first step was to use the ADS tool *Impedance Matching Utility* and create a Chebychev Low Pass filter match for both the input port and output port. After that, and using the optimization tool from ADS it was possible to improve even further the matching circuitry and S-Parameters. The schematic sheet used in ADS to improve the performance of the matching network is shown in Figure 4.34.

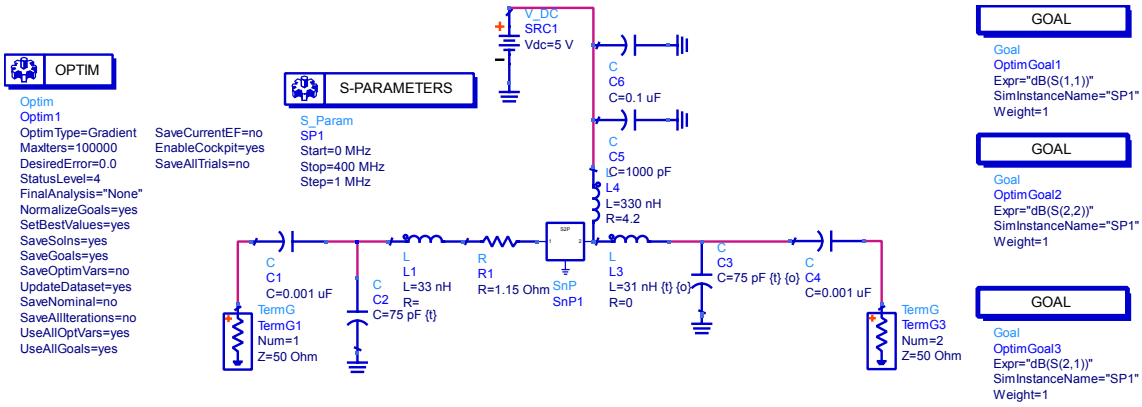

Figure 4.34: Schematic used in ADS to calculate the matching network for the gain block.

By using this matching network, the amplifier was matched through the whole bandwidth needed as it is shown in the measurements section (Figure 4.37) which shows a comparison between the results obtained in simulation and the measured practical results.

In terms of layout, the components used had the usual features for both power decoupling/bypassing and matching network. A switch was also used to check if turning on and off the gain block using a switch in the power supply could keep a fast performance in terms of transition between states.

Several stitching vias were used behind the ground paddle of the chip, as always, to reduce its inductance to ground and to dissipate as much as possible the heat generated at the component. The different views of the 3D model for the designed switch board are shown in Figure 4.35.

4.2.13.2 Measurements

The first task was to measure the S-Parameters of the gain block board to check if they were matched with the simulation results. By using a calibrated VNA it was possible to check that indeed they were almost perfectly matched as shown in Figure 4.37. This was expected since at these frequencies a schematic simulation using ADS is very accurate.

The return loss ($|S_{11}|$) is bellow -10 dB from 74 MHz to 113 MHz which show that the gain block is matched and low power will be lost due to mismatch; the isolation ($|S_{12}|$) is above 30 dB through all the bandwidth and the typical gain ($|S_{21}|$) is 22 dB from 90 MHz to 110 MHz.

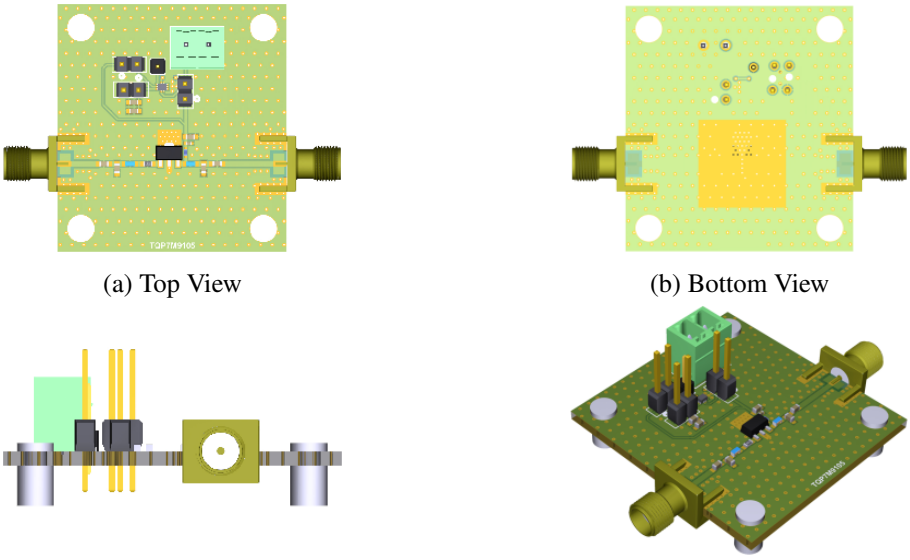

(a) Top View (b) Bottom View

(c) Side View (d) Isometric View

Figure 4.35: Different views of the designed gain block.

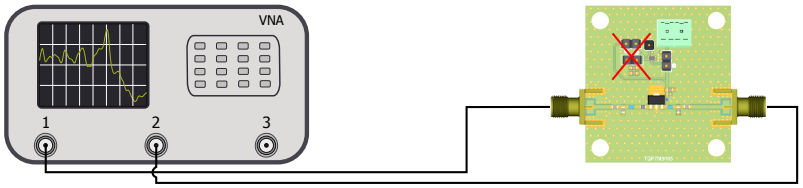

Figure 4.36: Illustration of the measurement setup for the gain block board.

Since the S-Parameters corresponded to what was expected the next step was to measure the P1dB point to evaluate the linearity of this amplifier. In the datasheet it was stated that at 940 MHz the P1dB was +30 dBm but there was no information on the value for 100 MHz. By using a VNA it was possible to measure this point for the different frequencies needed and the results are shown in Figure 4.38 (left).

The values obtained for the P1dB at 100 MHz are lower than the ones stated for 940 MHz. This is a major penalty since it limits the amount of power transmitted to the underwater medium. These results show that for a signal centered at 100 MHz and with a 5 MHz bandwidth the maximum output power should be around 23 dBm. On the other hand, if the signal has a bandwidth of 20 MHz the maximum output power should be 22.2 dBm.

The switch used to verify if it was possible to turn on and off the gain block was not used since its performance was worse than expected, needing around 2 μs to function properly when turning on. For this reason the gain block used in the final board is always enabled. To verify if there was no feedback on the amplification chain due to this choice that could compromise the proper functioning of the system, the complete loop was simulated and those results are presented in Section 4.3.

Despite the performance of the gain block in terms of linearity was not the expected, it can

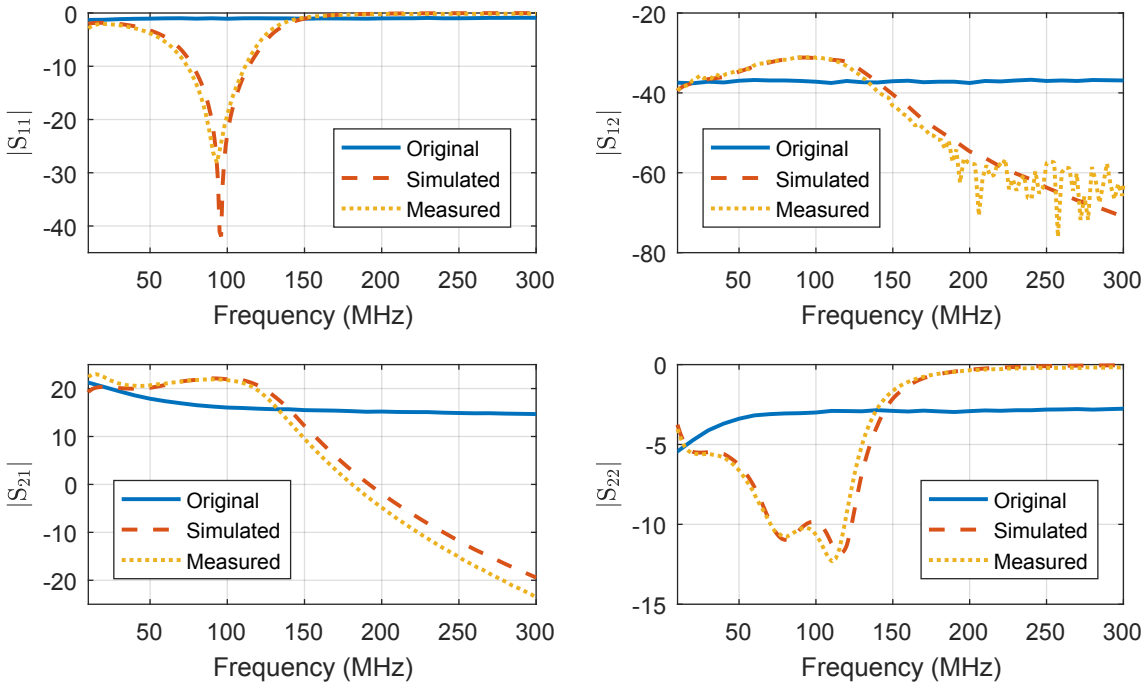

Figure 4.37: Obtained results for the S-Parameters of the gain block board.

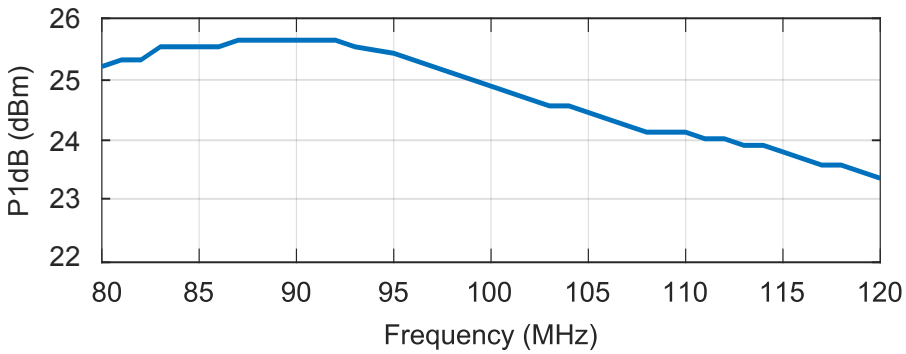

Figure 4.38: Obtained results for the measurements to the gain block board.

still be used on the Up-Down Converter board to compensate the conversion losses of the passive mixer.

4.2.14 Low-Noise Amplifier

As demonstrated in chapter 2 the first stage of a receiver front end has the dominant effect on the noise performance of the overall system. Especially in these kind of high loss transmission mediums where the signal received by the antenna has very low power, a good LNA is crucial for the performance of the overall system. The most relevant parameters for the LNA are their linearity, gain and noise figure.

The LNA is used to amplify the 100 MHz signal that is received in the antenna. One good option for this task was designed by Qorvo, the TQP3M9035. This is a broadband LNA that is internally matched over all the frequencies of interest and only required an external RF choke and

bypass capacitors for the supply/output pin. Despite that, by using the S-Parameters provided by Qorvo and the ADS, its performance was optimized even further for our IF signal by making suitable adjustments to the external RF choke and DC Block capacitors by changing the inductance to 330nH and the DC block capacitors by a higher value of 1000pF. The expected LNA performance has high linearity (P1dB = 21.3 dB @ 100MHz), high gain (Gain = 28.3 dB @ 100MHz) and low noise figure (NF = 0.52 dB @ 100MHz). This LNA also comes with a shutdown biasing capability that will allow the turn on/off based on the signal outputted by the comparator.

Different views of the 3D model for the designed LNA board are shown in Figure 4.39.

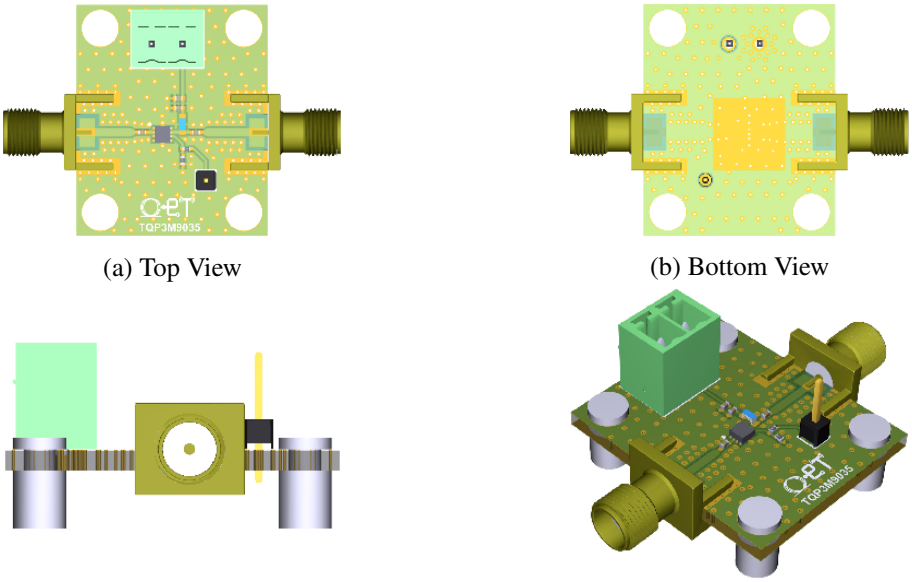

(a) Top View (b) Bottom View

(c) Side View (d) Isometric View

Figure 4.39: Different views of the designed LNA board.

4.2.14.1 Measurements

Different measurements were done to the LNA board. Starting by the usual S-Parameters measured by a calibrated VNA and illustrated in figure 4.40 (left) and ending with a measurement performed using a modulated Wi-Fi 802.11n OFDM signal (64 QAM) with an avarage power of -60 dBm and checking the difference between the spectrum before and after going through the LNA. The results are shown in Figure 4.41 and Figure 4.42 respectively.

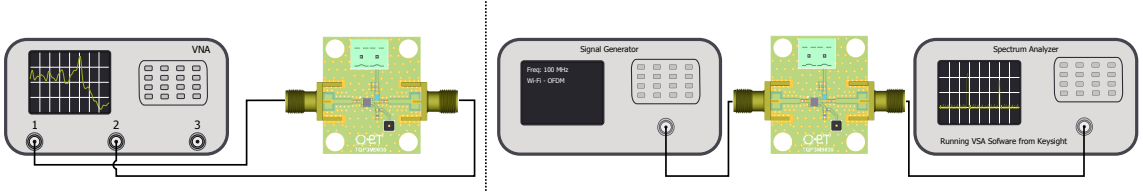

Figure 4.40: Illustration of the measurement setup for the LNA board.

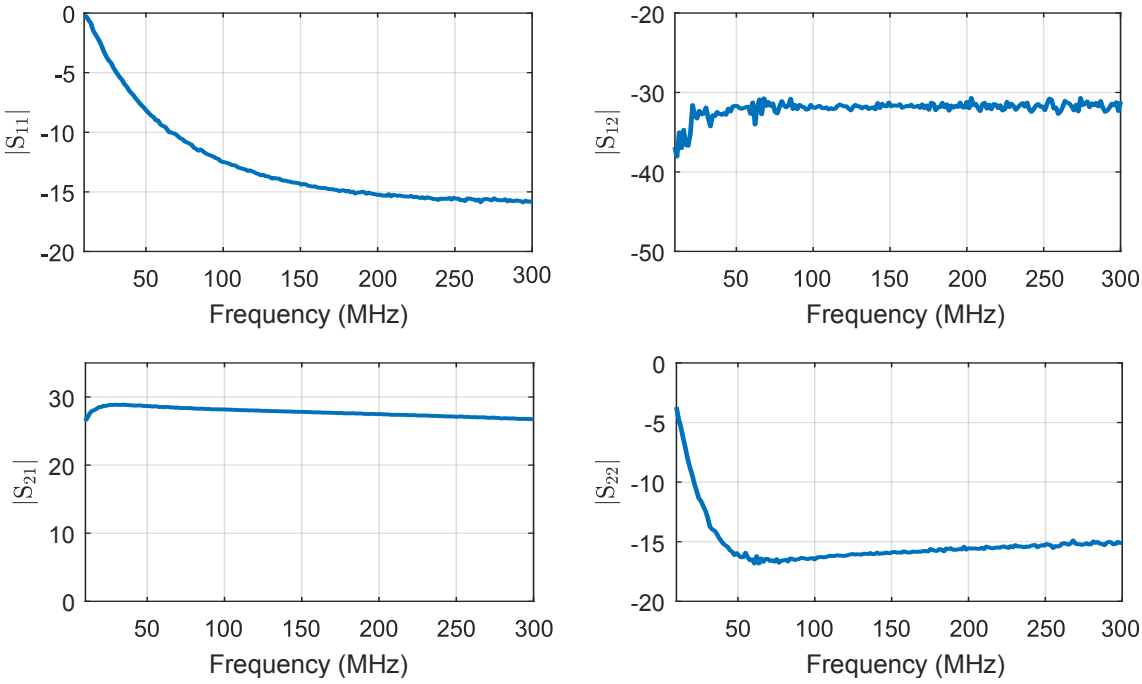

Figure 4.41: Obtained results for the S-Parameters of the LNA board.

The results obtained for the return loss shown that the LNA is well matched from 65 MHz to at least 300 MHz. The gain is around 28 dB in the whole band needed. The isolation is high with values above 30 dB and the output port is also matched as shown by the return loss at the second port (S_{22}).

The second measurement showed that, the power of the signal is highly amplified and the EVM of the demodulated Wi-Fi signal is much lower when the signal go through the LNA.

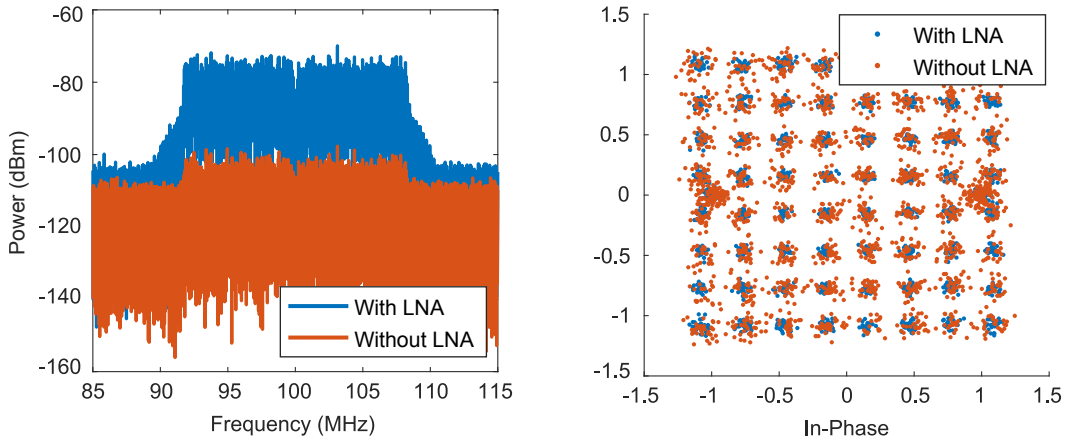

Figure 4.42: Obtained results for the measurements to the LNA board.

4.2.15 Low-Pass Filter

The low pass filter is used to clean the undesired inter-modulation products in the mixer when it is downconverting the transmitting signal. Another important task for this filter is to clean the undesired harmonics produced in the low-noise amplifier that should not go into the mixer.

The filter chosen for this task was the LFCN-105 from Mini-Circuits which is a ceramic low-pass filter with a very flat response and high roll.off factor as it will be shown in the measurements section.

Different views of the 3D model for the designed low-pass filter board are shown in Figure 4.43.

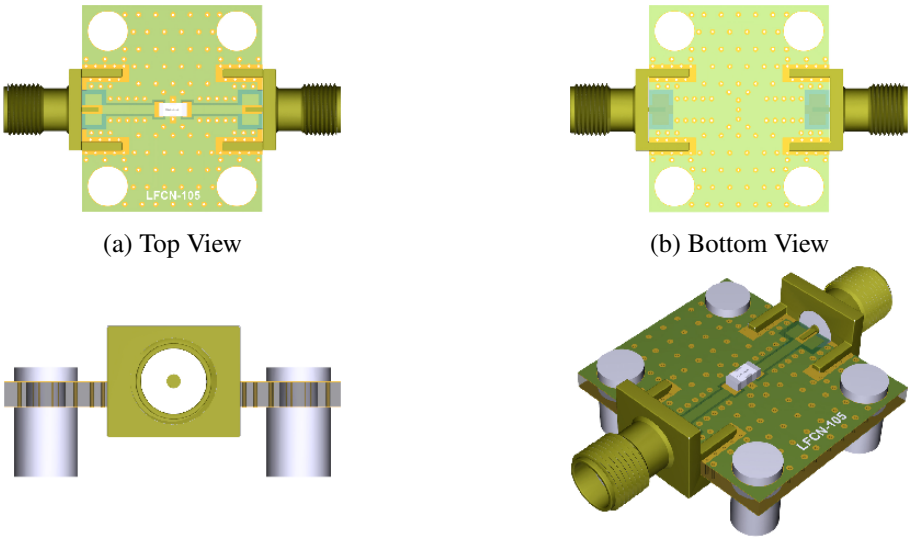

(a) Top View (b) Bottom View

(c) Side View (d) Isometric View

Figure 4.43: Different views of the designed low-pass filter board.

4.2.15.1 Measurements

The results obtained for the insertion loss and group delay of our low-pass filter are shown in Figure 4.45.

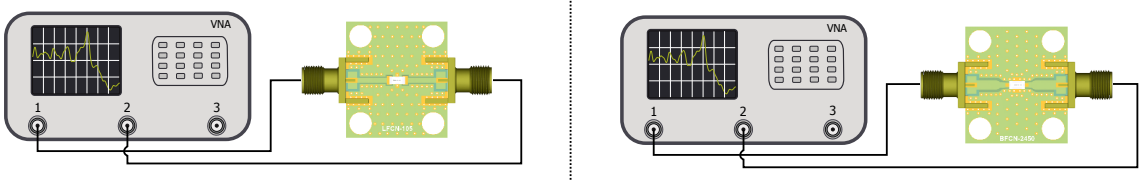

Figure 4.44: Illustration of the measurement setup for the low-pass filter (left) and band-pass filter boards (right).

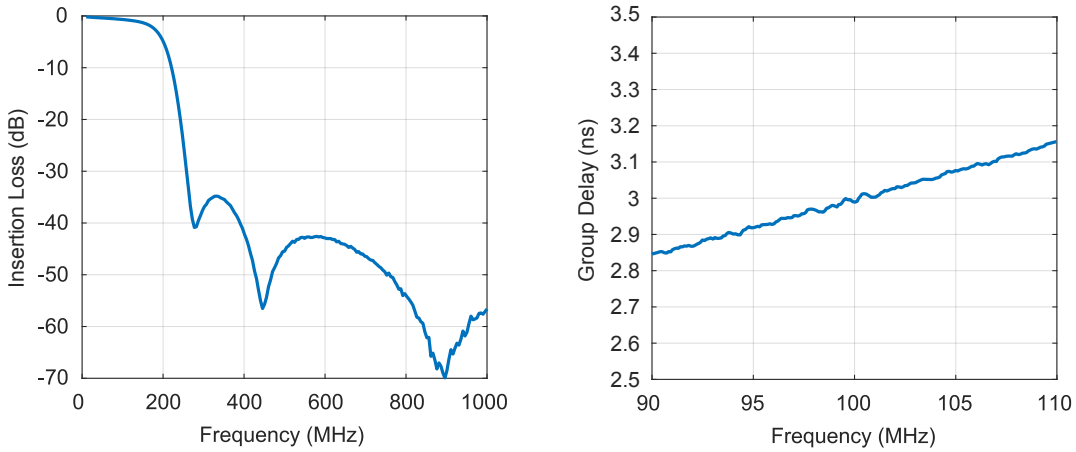

Figure 4.45: Obtained results for the different measurements to the low-pass filter board.

As can be seen, the filter has a relatively flat response in the passband with an insertion loss of around 0.5 dB, a 1 dB cut-off frequency of 133 MHz and a 3 dB cut-off frequency of 182 MHz. The roll-off of this filter is very high allowing an attenuation of 10 dB at 220 MHz.

In terms of group-delay, the response in the passband is very flat as desired and with a value of 3ns.

4.2.16 Band-Pass Filter

The bandpass filter in the transmission is going to be used to filter possible noise that might come from the Bullet M2 and, in the reception will be used to filter the frequency image of the mixer and undesired intermodulation products produced when upconverting in the mixer.

The desired filter for this application was the 885136, but due to unavailability at the market the filter used for this task was the ceramic bandpass BFCN-2450+ from Mini-Circuits. This option, despite not being able to provide good filtering on the frequency image of the mixer when upconverting, will be important in filtering some of the intermodulation products.

Different views of the 3D model for the designed band-pass filter board are shown in Figure 4.46.

4.2.16.1 Measurements

The results obtained for the insertion loss and group delay of our low-pass filter are shown in Figure 4.47.

As can be seen, the filter as a relatively flat response in the passband with an insertion loss of 2.2 dB which is a bit high but should not cause any problem since it deals with the high power RF signal transmitted by the bullet and the received signal amplified by the LNA. The center frequency of this filter is 2.45 GHz with the two 3 dB cut-off points at 2.24 GHz and 2.67 GHz.

In terms of group-delay, the response in the passband is very flat as desired and with a value of 1.8 ns.

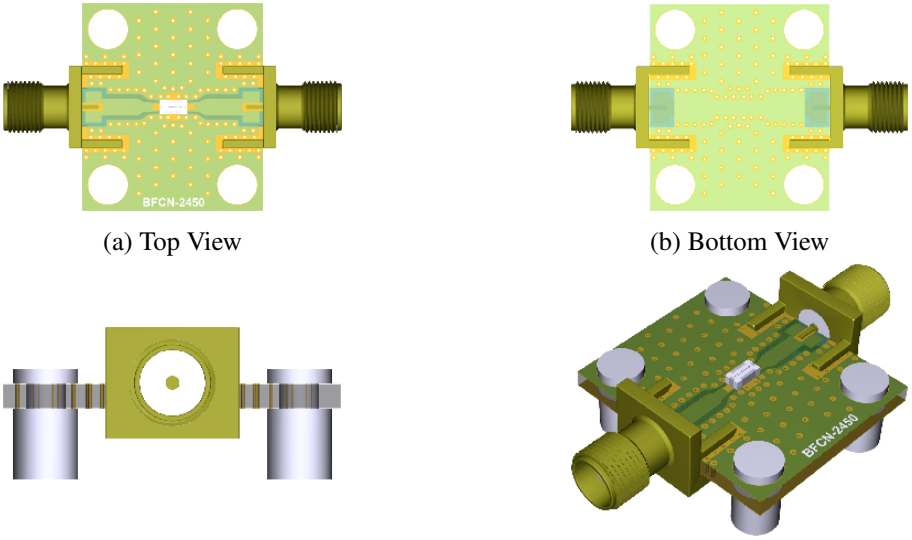

(a) Top View (b) Bottom View

(c) Side View (d) Isometric View

Figure 4.46: Different views of the designed band-pass filter board.

4.2.17 Power Supply

Obtaining a clean output signal when transmitting and receiving RF signals can be challenging and the first source of noise usually comes from the power supply. It was established by the engineers that are doing the AUV that the main source of power for the whole board would be a 24V battery. With exception of the LDO that supplies the PLL that needs 5.5V and the TCXO that needs 3.3 V (which is going to be supplied by that same LDO), all the other components need a VCC of 5V to work.

There are then two different voltages needed: 5.5V and 5V. To go from 24V to 5.5V a DC-DC switching regulator will be used. The reason for this is that they offer three main advantages in relation to a linear regulator for this high dropout voltages: better efficiency; less energy is lost in the transfer, less thermal management is required. Despite this advantages the linear regulators

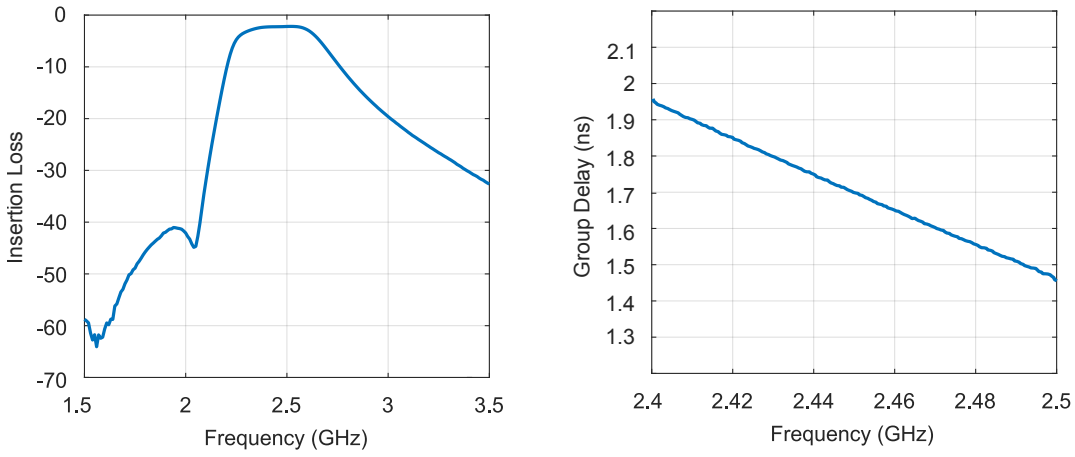

Figure 4.47: Obtained results for the different measurements to the band-pass filter board.

provide a lower noise and higher bandwidth and are cheaper. That's why a linear regulator will be used to go from 5.5V to 5V and supply all the other components.

The DC-DC chosen for this task was the UEI15-050-Q12 from Murata. This is a 15W DC-DC with a nominal input voltage of 24V, and an output voltage that can be trimmed to 5.5V. The maximum regulation on the line and on the load are $\pm$ 0.05 % and $\pm$ 0.075 % respectively and the typical efficiency is 87.3 %. It features an isolation up to 2250 VDC which will protect the whole final board, and an enable pin that will not be used for our application.

The LDO chosen to convert the 5.5V into 5V was the TPS7A89 from Texas Instruments. It features two independent LDO channels, low output noise, and an excellent load transient response that is needed for this kind of high-speed analog circuits. It also features an enable pin for each output channel of the LDO which will be used in the final board to turn on and off the Up-Down Converter system using the interface that communicates with the Arduino Mini Pro.

Different views of the 3D model for the designed Power Supply board are shown in Figure 4.48.

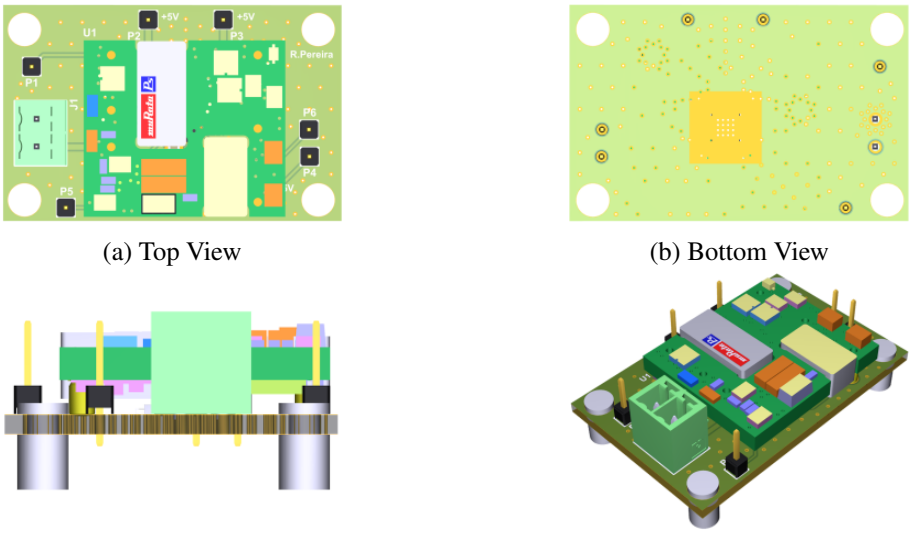

(a) Top View

(b) Bottom View

(c) Side View

(d) Isometric View

Figure 4.48: Different views of the designed power supply board

4.2.17.1 Measurements

The power supply board was mounted and its performance was validated by measuring the 5.5 V output voltage at the output pin of the DC-DC and the 5V output voltage at the two output pins of the LDO as illustrated in Figure 4.49.

4.2.18 Summary

Although it was not possible to measure some of the key performance indicators of some of the modules like the noise figure of the LNA, or the phase noise of the PLL, due to lack of time or

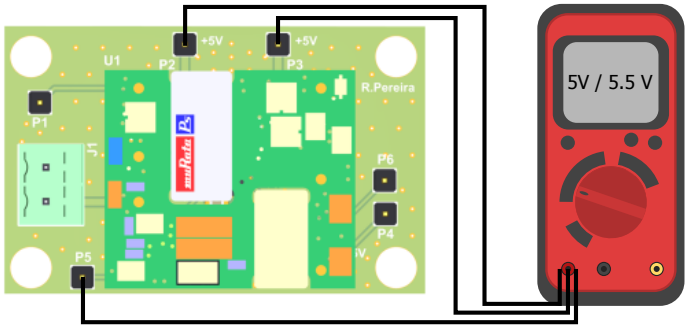

Figure 4.49: Illustration of the measurement setup for the power supply board.

lack of appropriate equipment, all the self designed evaluation boards were validated and almost complete characterized.

A photograph of these individual self-designed and self-soldered modules which are part of the final Up-Down Converter board is shown in Figure 4.50.

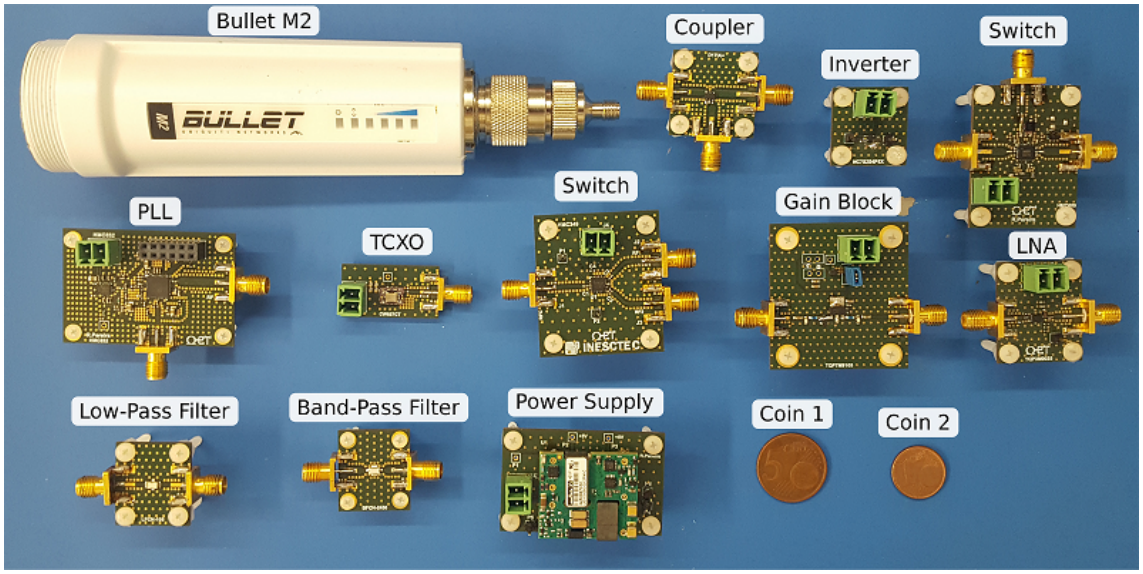

Figure 4.50: Individual self-designed and self-soldered modules which are part of the final Up-Down Converter board.

4.3 Up-Down Converter Design and Characterization

4.3.1 Up-Down Converter Design

After validating all the boards using the self-designed evaluation boards, it was time to join all their layouts in the same one and do the final Up-Down Converter board.

In this process, it was tried as much as possible to keep intact the same layouts of the already designed evaluation boards. The routings between modules as well as the size of the final board

should be as small as possible and without compromising the well functioning of the board, mainly in the RF routes.

Since it was not possible to use the switch to turn on/off the gain block, both the amplifiers are on when receiving the signal. This might create an unwanted feedback loop that might compromise the well function of the system. To avoid that, it was tried to put the two different tracks as far away as possible while keeping the symmetry of them as well as placing several vias inside the loop to ensure an extra level of shielding between the two tracks. All the loop was then simulated by importing the gerber files designed for the loop into the ADS.

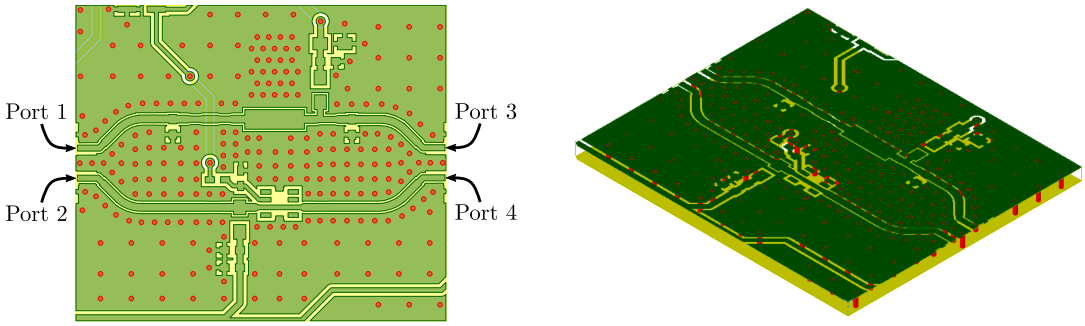

(a) (b)

Figure 4.51: Layout (a) and 3D Model (b) of the basic electromagnetic simulation performed to the loop

The first simulation done was a Momentum Microwave simulation where the matching networks were short-circuited as well as the amplifiers pads as seen in Figure 4.51. The goal was to measure the isolation of the two tracks that should be as high as the isolation inside the chips of the two switches. The layout and 3D model of this electromagnetic simulation as well as the 3D visualization of the magnitude of the electromagnetic fields can be seen in Figure 4.51 and Figure 4.52 respectively.

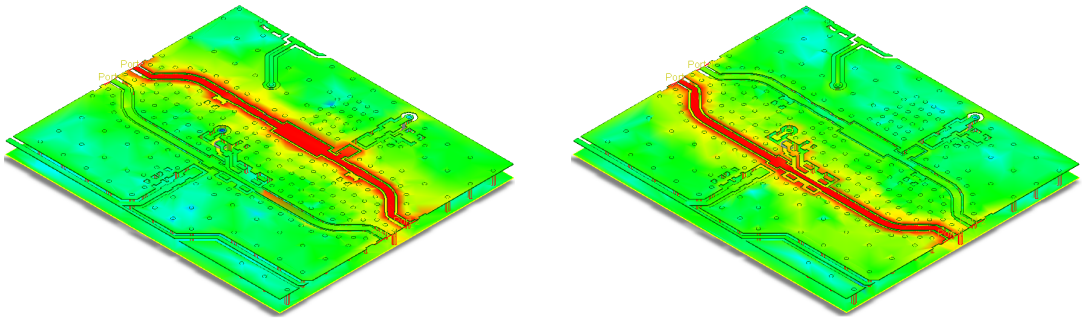

(a) Transmission path. (b) Receiving path.

Figure 4.52: Visualization of the magnitude of the electromagnetic fields for the electromagnetic simulation of the model shown in Figure 4.51

It is seen that the loop is filled with vias inside that increase the isolation between the two track through an improved ground plane between them.

In the simulation, the port 1 and port 3 are the input and output ports, respectively, of the transmission chain, and the port 2 and port 4 are the input and output ports of the receiving chain respectively. The results of the S-Parameters obtained for this simulation are shown in Figure 4.53. On the left side are shown the results for the transmission path, with the insertion loss ($|S_{21}|$), and isolation between Port 1 and Port 3 ($|S_{31}|$) and between Port 1 and Port 4 ($|S_{41}|$). On the right side are shown the results for the receiving path, with the insertion loss ($|S_{42}|$), and isolation between the Port 4 and Port 1 ($|S_{14}|$) and between Port 4 and Port 2 ($|S_{24}|$). It is seen that the insertion loss on the lines is very low as expected for a 100 MHz CPWG line and the isolation between all the tracks is around 70 dB which despite being less than the isolation inside the chip, is high enough for this application.

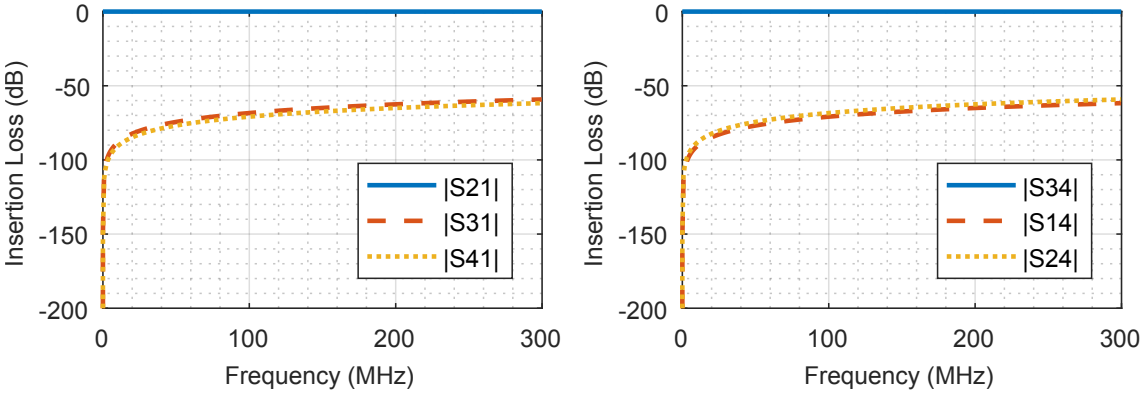

Figure 4.53: Obtained results for the S-Parameters of the designed loop.

After analyzing the isolation between the tracks, a more accurate electromagnetic simulation of the complete loop was done. This time, the complete loop was simulated by measuring its S-Parameters and then performing a co-simulation of the complete board using the obtained simulated results and the de-embedded S-Parameters provided by the manufacturers . The layout and 3D model of this simulation are shown in figure 4.54 and the obtained results are shown in Figure 4.55.

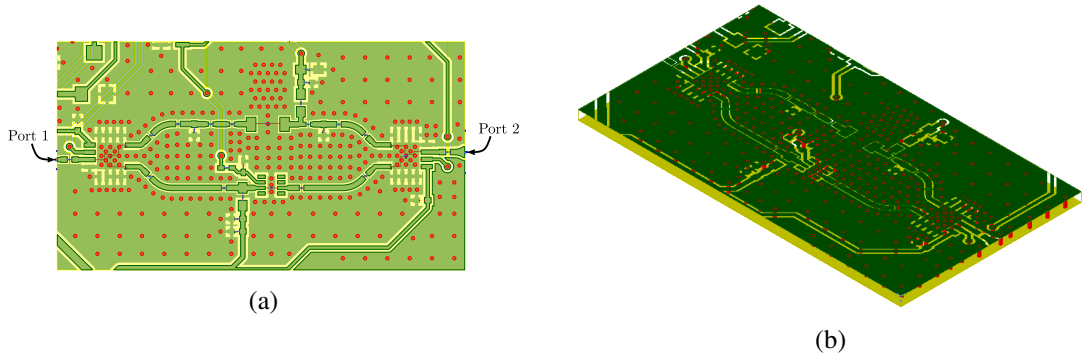

(a) (b)

Figure 4.54: Layout (a) and 3D Model (b) of the complete electromagnetic simulation performed to the loop

To note that the $|S_{11}|$ and $|S_{22}|$ shown give the return loss on RFC pin of the first and second

switches, respectively, when the transmitting path is enable or when the receiving path is enable. The $|S_{12}|$ gives approximated values of the the isolation between the output and input of the gain block for the transmitting path and gain of the LNA for the receiving path, while the $|S_{21}|$ gives approximated values of the gain of the gain block for the transmitting path and isolation between the input and output port of the LNA for the receiving path.

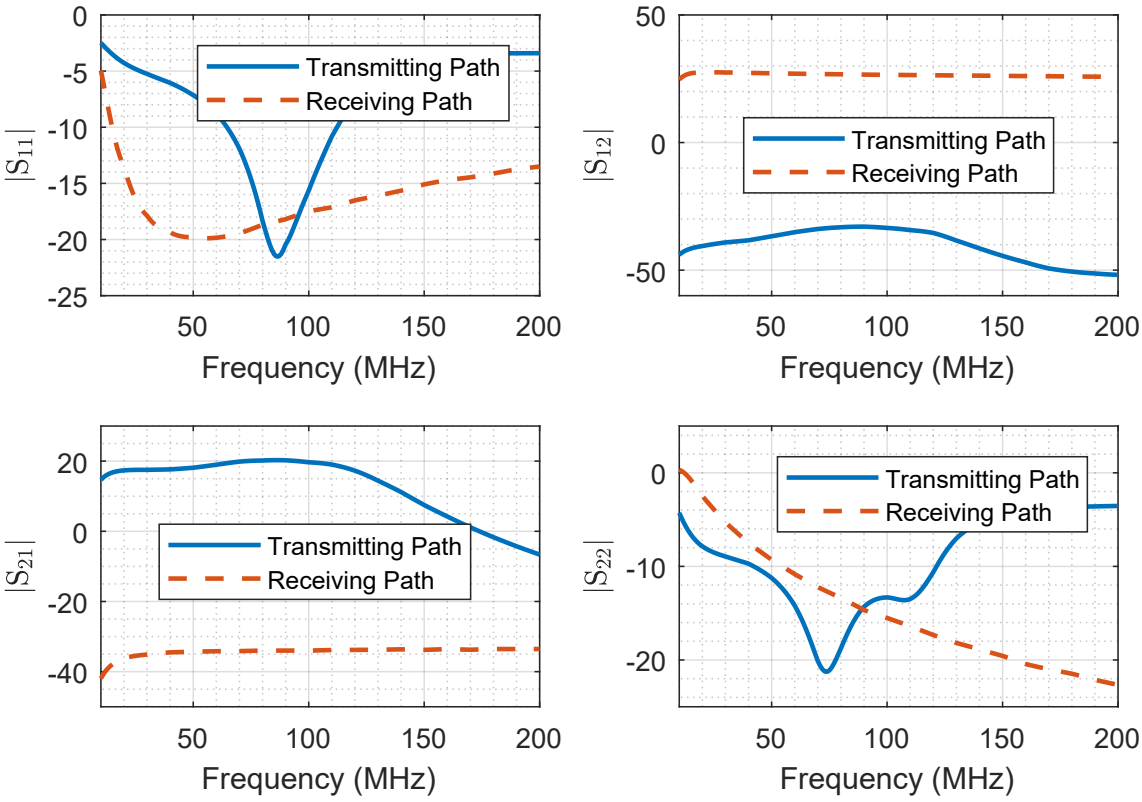

Figure 4.55: Obtained results for the S-Parameters of the complete designed loop.

The results show that there is no unwanted oscillation inside the loop since the $|S_{11}|$ and the $|S_{22}|$ are less than 1. Although the best values for the return loss shifted from the expected 100 MHz the results are still good with a return loss higher than 14 dB in all the ports. This shift can be explained by the parasitic effects introduced by the lines that were not taken into account in the design process. The gain of the transmission path and receiving path are as high as expected with values around 20 dB for the gain block and 27 dB for the LNA (to note that these values take into account the insertion losses of the two switches and the transmission lines).

After evaluating the performance of the loop, there were still two signal routes that had their bottom ground plane return path broken: one near the band-pass filter (Figure 4.56a), and another near the low-pass filter (Figure 4.56b). In order to evaluate if there were no major problems with these layout sections their performance was also evaluated with ADS.

To evaluate the performance of this sections two measurements were done: the return loss, to check if there was a higher attenuation and the group delay, to check if there was any distortion in the signal phase. The results of these two measurements are shown in Figure 4.58 for the low-pass

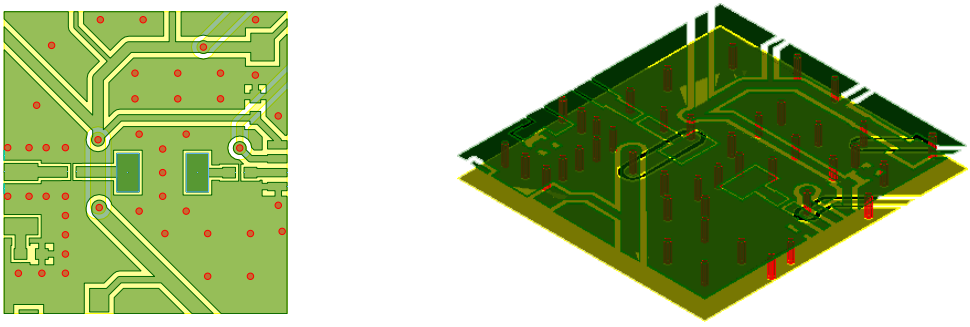

(a) (b)

Figure 4.56: Layout (a) and 3D Model (b) of the advanced electromagnetic simulation performed the low-pass filter section.

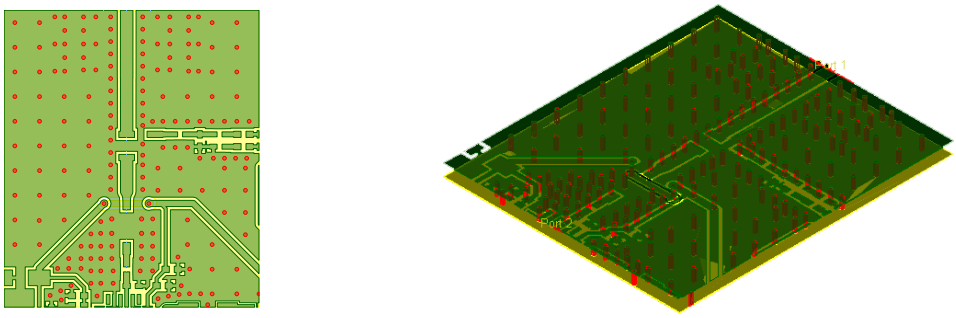

(a) (b)

Figure 4.57: Layout (a) and 3D Model (b) of the advanced electromagnetic simulation performed to the band-pass filter section.

filter section, and in Figure 4.59 for the band-pass filter section.

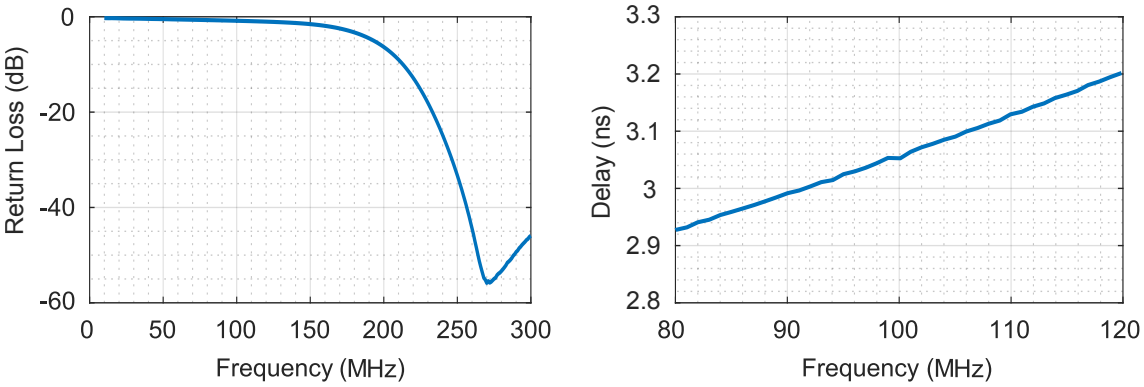

Figure 4.58: Obtained results for the return loss and group delay of the low-pass filter section.

The results show a similar behavior as the ones seen in the self designed evaluation boards, in terms of return loss and group delay for both sections. It was seen, despite not shown, that a diagonal brake on the ground plane beneath an RF trace degrades the performance at a shigher level than a perpendicular brake.

After taking into account, through simulation, of all the parts of the final Up-Down Converter

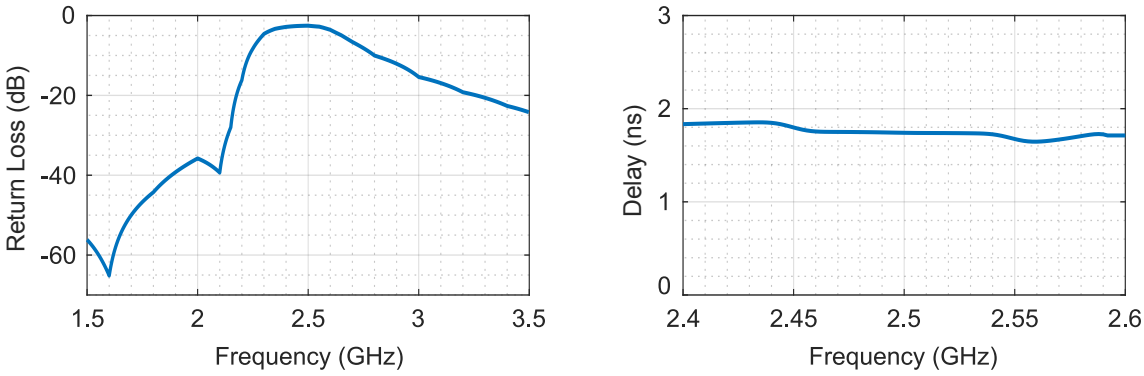

Figure 4.59: Obtained results for the return loss and group delay of the band-pass filter section.

board that could damage its performance, it is time to present the view of the final Up-Down Converter gerber files. That view with a guidance of all the modules which are part of the board are shown in Figure 4.60.

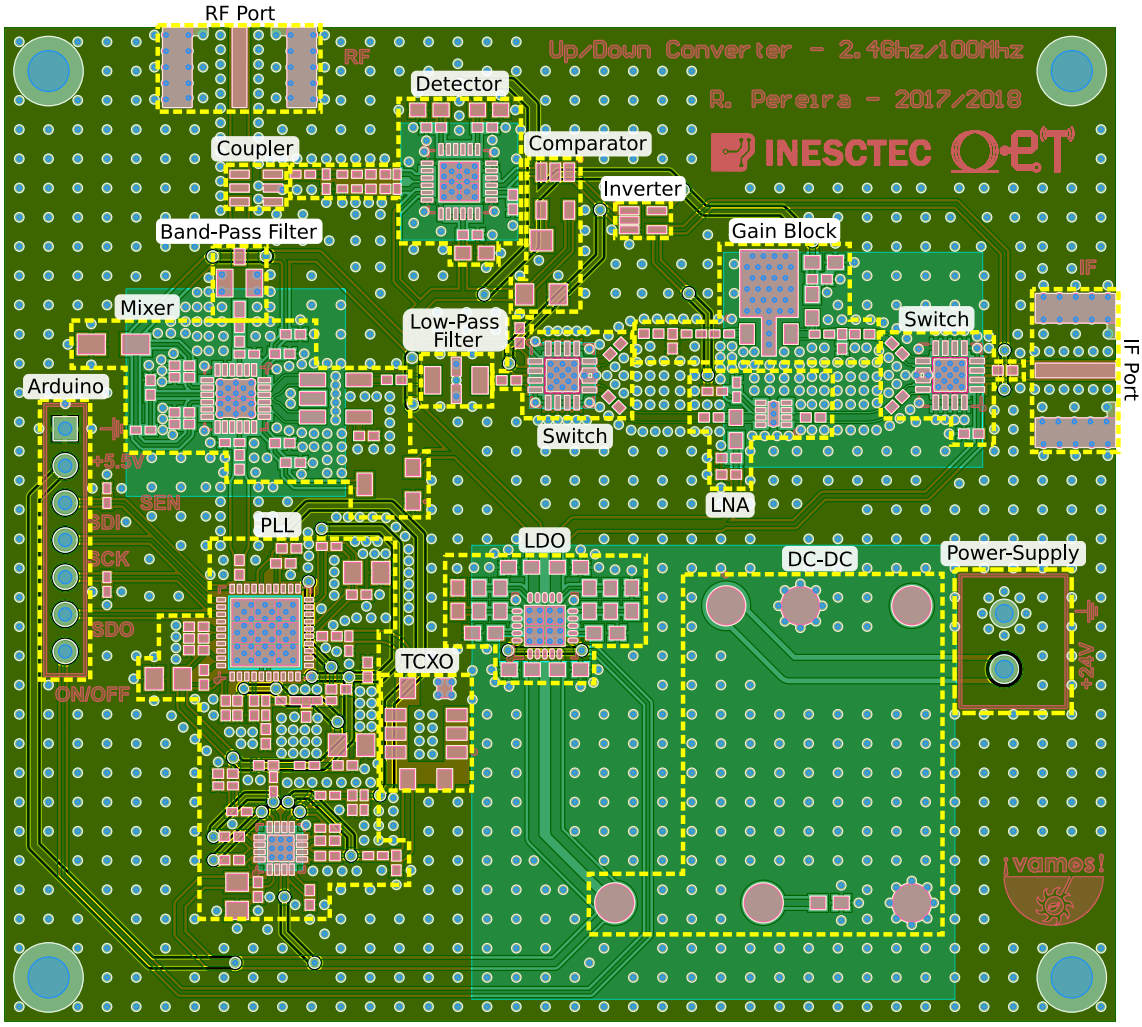

Figure 4.60: View of the gerber files for the designed final Up-Down Converter board.

The board's dimensions are 8x7 cm. It is possible to see that all the modules are very close, with the RF lines very small.

The board is supplied by a 24V battery which is then converted through a DC-DC into the 5,5V needed to supply 3 different LDOs: the embedded LDO of the Arduino, the LDO of the PLL, and the LDO chosen to supply all the other modules.

The board has two SMA Ports: the RF Port - used to connect to the Wi-Fi Card; and a IF port - used to connect to the antenna. The principle of functioning is the same explained before, with the board functioning in two modes:

- **Transmitting Mode:** When the Wi-Fi Card is in the transmitting mode, the power coupled to the Detector will be high enough to put its output voltage at 1.5V. This output voltage is the input voltage of the comparator that, with a reference voltage of 1.75V will output a digital signal of 0V that will activate the upper path of the first Switch. The second switch, since it is turned by 180^o need to activate the lower path (which correspond to the one that connects to the output of the gain block). The inverter is used for this task, turning the 0V signal into 5V that then goes to the second controller pin of the Switch. This signal also controls the enable pin of the LNA, turning it off. While this happens, the RF signal that went through the Coupler passes the band-pass filter and enters the RF pin of the mixer. On the other hand, the LO pin already has a defined frequency from the PLL which was programmed by the Arduino. This two signals, RF signal and LO signal, through mixing, will output the sum and difference frequency of the two, where the low-pass filter will just allow the frequency difference (IF Frequency) to go to the switch. This signal is then amplified in the gain block and radiated through the Antenna connected to the IF Port.

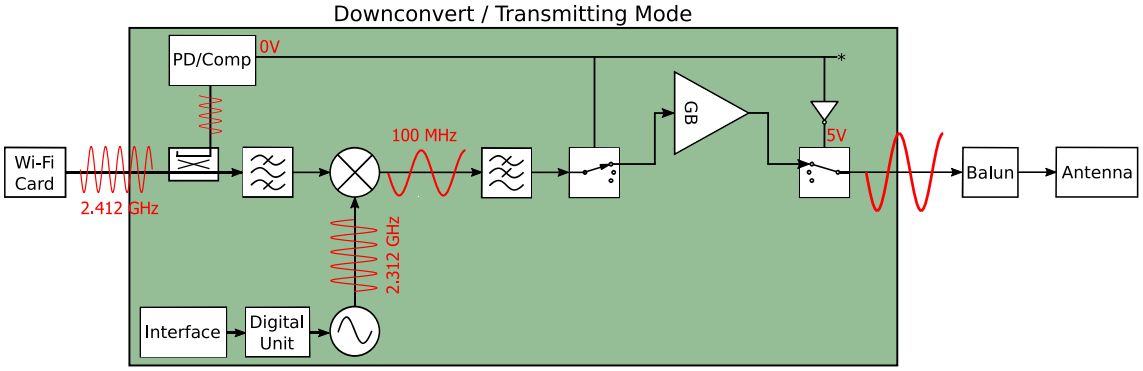

Figure 4.61: Illustration of the downconvert operation in the transmitting mode.

- **Receiving Mode:** When the Wi-Fi Card is in the receiving mode, the power coupled to the detector will be small and its output voltage will remain at 2V. This output voltage is the input voltage of the comparator that, with a reference voltage of 1.75V will output a digital signal of 5V that will activate the lower path of the first Switch. The second switch need to activate the upper path and this is done with the help of the inverter as was mentioned in the

previous mode. The LNA is also activated with the 0V signal that comes from the inverter. The IF signal that is received by the antenna goes through the LNA and enters the low pass filter where it filter some of the harmonics produced in the LNA. It then enters the IF pin of the Mixer and by mixing with the LO will upconvert the IF signal into the RF signal that goes to the Wi-Fi Card. To note that when in the receiving mode, both amplifiers are turned on, but the only problem is the energy waste as seen in the simulation performed to the loop.

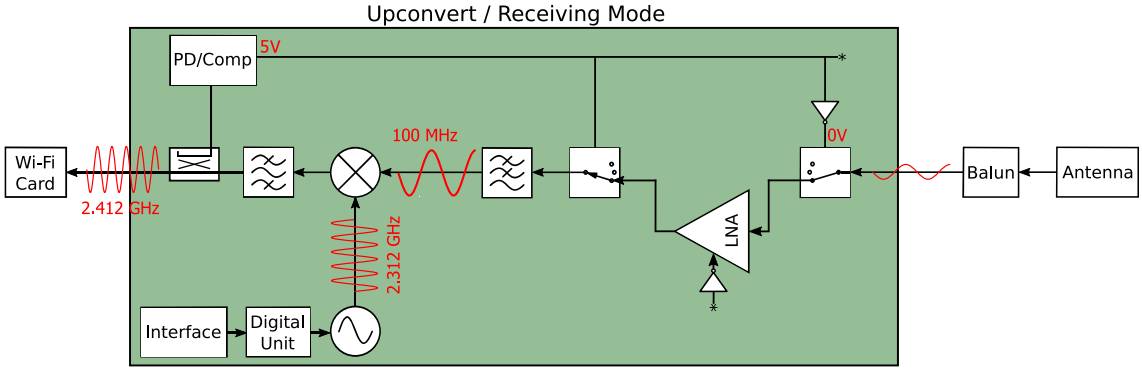

Figure 4.62: Illustration of the upconvert operation in the receiving mode.

The complete 3D view of the final Up-Down Converter board is shown in the Figure 4.63.

4.3.2 Up-Down Converter Characterization

After one week of waiting for it to be manufactured, and after 6 hours of manual soldering the final Up-Down Converter board was ready to have its performance evaluated, as shown in Figure 4.64.

The first measurement performed to the board consisted in applying a Wi-Fi 802.11n OFDM signal of -60 dBm to the IF port and check the upconverted signal at the RF port, to validate the performance of the receiver, as illustrated in Figure 4.65 (a). The obtained results are shown in the upper graph of Figure 4.66 .

It is possible to see that there is a lot of noise that is mixed with the OFDM signal, and this noise limits the maximum SNR, and consequently that maximum data-rate and distance obtained for the system.

As shown in Chapter *chap:sota*, in a telecommunication system the first source of noise is usual the power supply, and this was the case. By using a probe connected to the oscilloscope in the output of DC-DC and another connected in the output pin of the LDO, it was possible to find the source of all this noise. The results of time-domain signal and the equivalent frequency-domain signal obteined in the oscilloscope are shown in the top and bottom graphs, respectively, of Figure 4.67

The results show that the spectrum of the noise generated at the DC-DC is equivalent to the one obtained at the RF port while upconverting. The frequency of the noise is around 40 MHz and the choosed LDO is not able to filter such a high frequency noise as shown by the graphs and also

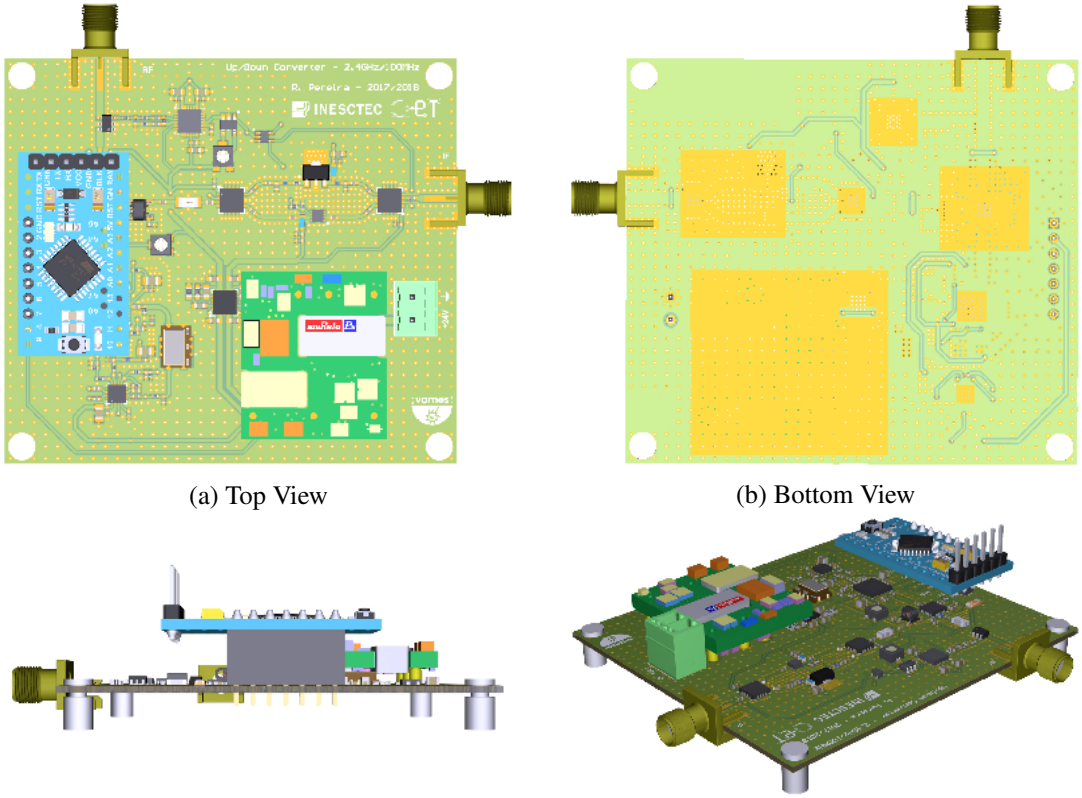

(a) Top View (b) Bottom View

(c) Side View (d) Isometric View

Figure 4.63: Different views of the designed final Up-Down Converter board.

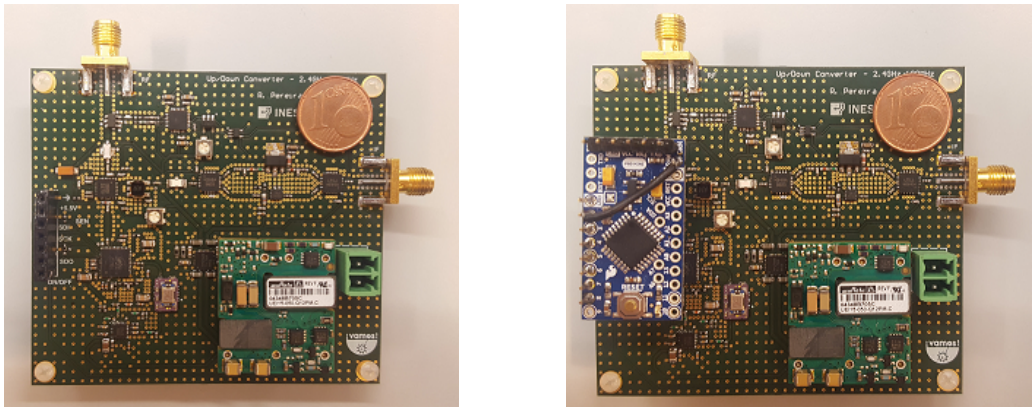

(a) (b)

Figure 4.64: Photograph of the final designed and soldered Up-Down Converter board with and without the Arduino connected.

as stated in the datasheet of the component. This noise then goes through the VCC net to the VCC pins of all the modules that do not have a decoupling capacitor for this frequency. This noise is even amplified at the LNA before being mixed with the LO.

The source of noise that degrade the performance of the designed Up-Down Converter was then found. Despite the final Up-Down Converter board could be used in underwater communi-

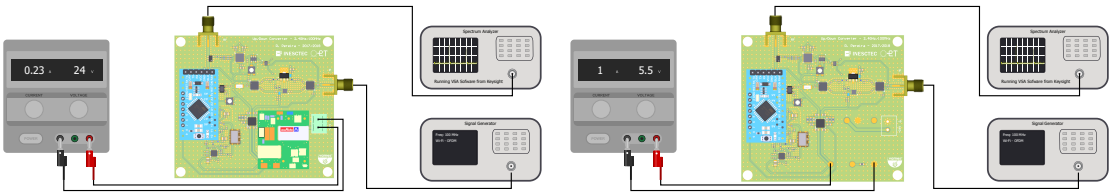

(a) (b)

Figure 4.65: Illustration of the two different measurement setups for the final Up-Down Conversion board.

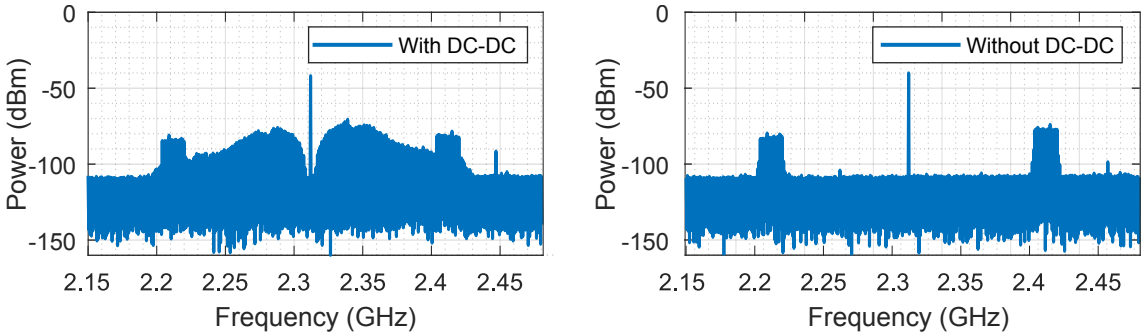

Figure 4.66: Comparative results on the performance of the upconversion with and without DC-DC.

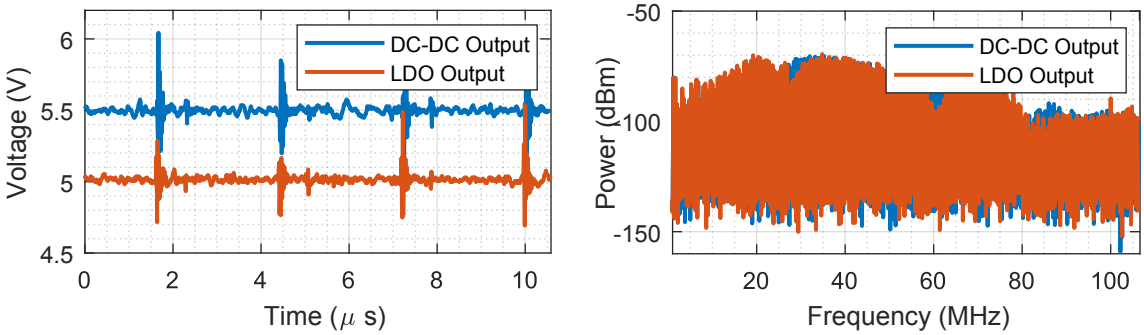

Figure 4.67: Noise measure on the output of the DC-DC and LDO in the time-domain (top) and frequency domain (bottom).

cation link as will be shown later in this section, its performance when compared with the board without DC-DC is a lot worse.

In order to boost the performance of the board, several solutions to this problem arise:

- Place decoupling/bypass capacitors with its SRF around the noise frequency on the output pins of the DC-DC.
- Design a new Up-Down Converter board with a better DC-DC for this application.
- Design a small PCB for a better DC-DC, in such a way that the designed PCB connect to the pads of the old DC-DC.
- Remove the DC-DC and apply 5.5V directly in the Up-Down Converter.

The last solution, illustrated in Figure 4.65 (b), despite not being the most sophisticated, was the one that could be implemented in the remaining time with a guaranteed good performance and in a way that the board was not damaged. This was then the used solution and the results obtained for the same measurements are shown in the bottom graph of Figure 4.66.

It is possible to see that the performance of the Up-Down Converter is much better with the new solution. The SNR is much higher allowing for a better demodulation of the OFDM signal and consequently a higher distance of communication and data-rate.

To validate even further this solution, the two boards were compared in another two different situations:

- Using a signal generated to apply a Wi-Fi 802.11n OFDM signal with a sweep in its output power into the IF port and check the demodulated signal using a VNA and the software VSA from Keysight to measure the resultant EVM. Figure 4.68 shows the IQ constellations of a demodulated signal for different values of EVM for the reader to have an illustrative guide.

- Establishing the communication between two Up-Down Converter boards with the Wi-Fi cards connected to the respective RF ports, and using attenuators to measure the maximum attenuation that the communication handles as ilustrated in Figure 4.70.

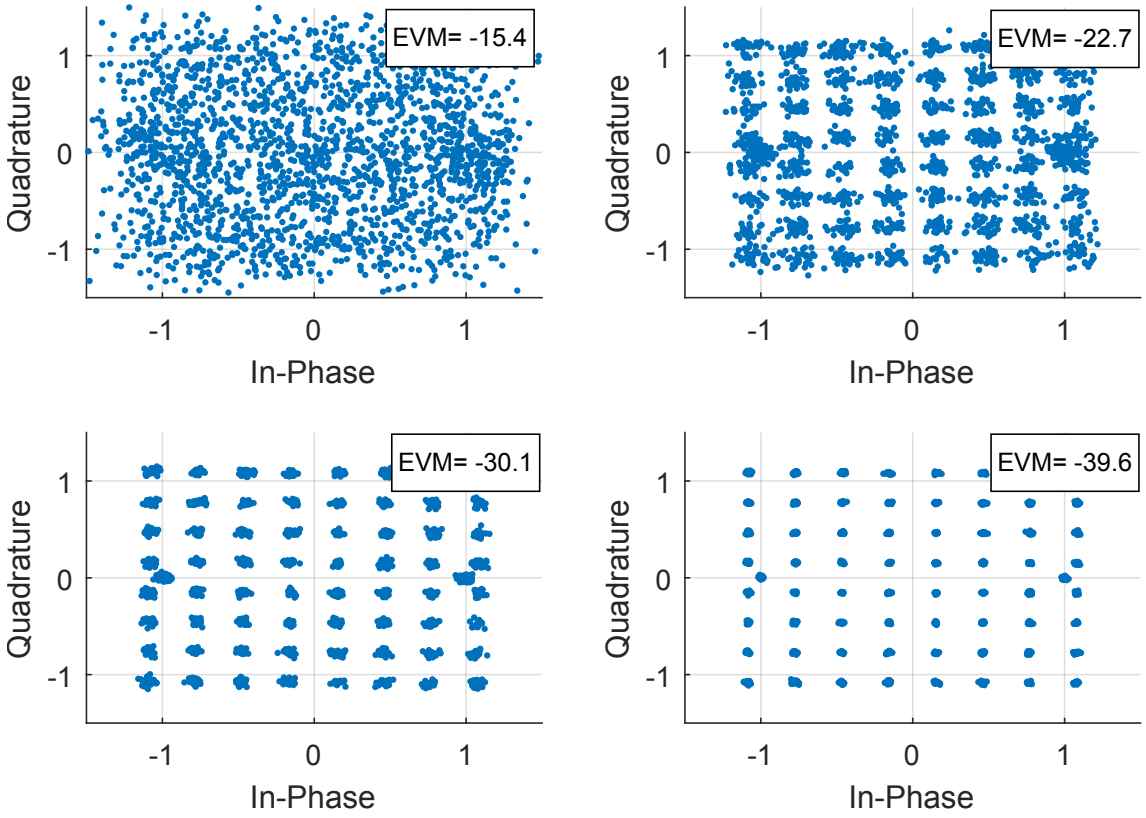

Figure 4.68: IQ constellations of a demodulated Wi-Fi 802.11n OFDM (64QAM) for different values of EVM.

The results obtained for the first measurement are shown in Figure 4.69 and is easily verified that for the same input power, the board without DC-DC has a much better (lower) EVM. As an example, for an input power of -50 dBm the EVM obtained for the board with DC-DC is -24 dB. The board without DC-DC just need -72 dBm to obtain the same performance, a difference of -22 dB. This extra 22 dB can be converted in an increased distance (as shown on subsection 2.3 of the *State of Art*) or higher data-rate. The results also show that for a received power higher than -24 dB the EVM starts to decreases. This is explained by the distortion on the LNA and the appearance of spurious signals that decrease the SNR.

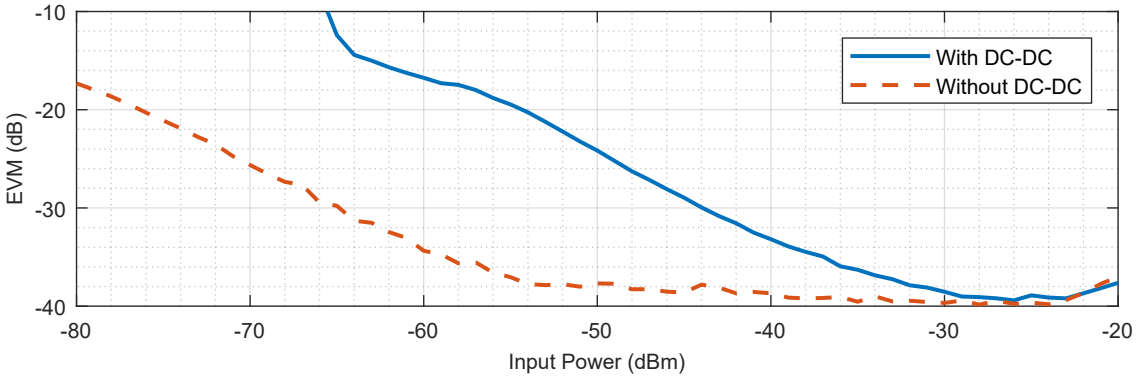

Figure 4.69: Compared results of the EVM obtained as a function of input power, for the full board and for the board without DC-DC.

For the second measurement only 10 dB steps of attenuation were used since this was just to validate if the two bullets could communicate through the Up-Down Converter boards, and if so, with how much attenuation the link would allow a communication with at least 1 Mbps, both in the case of the board with DC-DC and without. The link was successfully established in both cases, with the Up-Down Converter with DC-DC handling an attenuation of 60 dB and the Up-Down Converter without DC-DC handling an attenuation of 100 dB, both with a data-rate of 1 Mbps.

For the final measurements on the underwater medium, only the Up-Down Converter without DC-DC will be tested since there was no time to perform measurements for both cases, and it was decided to use the board with the best performance.

A photograph of the two Up-Down Converters used to establish the underwater tests in the pool that are presented in the next chapter is shown in Figure 4.71.

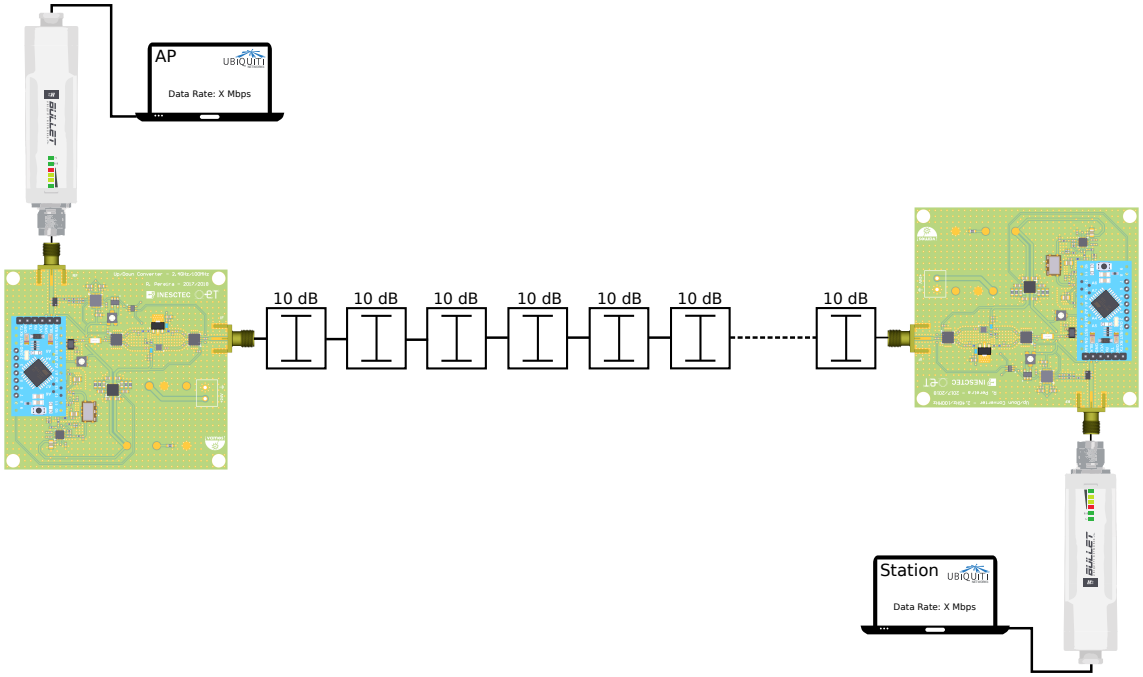

Figure 4.70: Illustration of the full link established by using the Bullet M2, the Up-Down Converters, and attenuators.

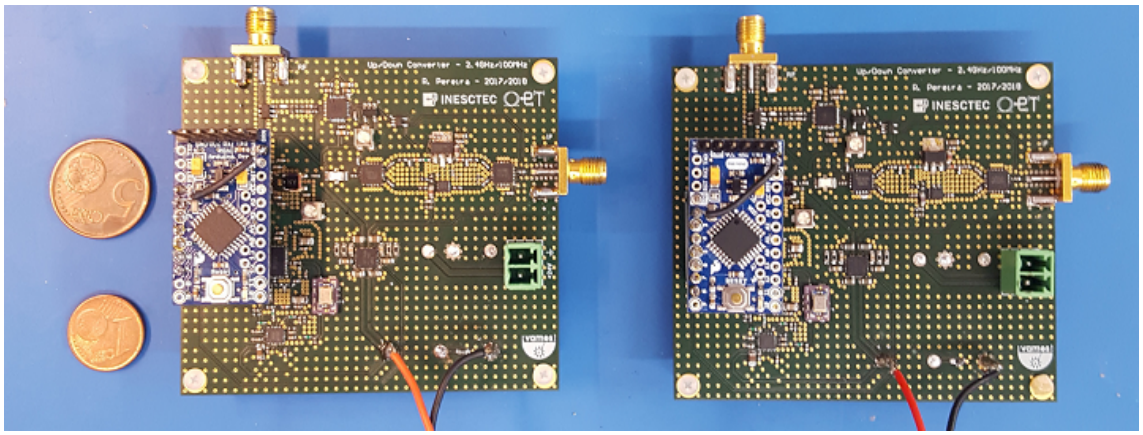

Figure 4.71: Photograph of the two Up-Down Converters without DC-DC used to perform the underwater measurements.

Chapter 5

System Characterization and Results

In this chapter it is presented all the tests that have been done to validate the implemented solution. Initially, the behavior of the S21 parameter as a function of distance was characterized. Then, the data-rate as a function of distance was measured, finalizing with a comparison of the size, price, robustness, maximum distance and correspondent data-rate of the new developed system and the one used before this master's work.

5.1 Field Characterization

To evaluate the performance of the system correctly, it is important to characterize the field where the measurements are performed. In this case, a sample of the water of INESC TEC's pool was taken and its conductivity was measured by using a conductivity meter as shown in Figure 5.1.

Figure 5.1: Measurement of water conductivity with a conductivity meter.

The obtained value was 353μS/cm, which corresponds to 0.0353S/m. By setting this value on FEKO software and changing the distance between the two antennas (Figure 5.2a), it was possible to measure the $|S_{21}|$ parameter as a function of distance and compare those results with the ones measured at INESC-TEC's pool (Figure 5.2b).

The comparative obtained results are shown in Figure 5.3. In this case it was found that the curve obtained experimentally was very similar to that obtained through FEKO software.

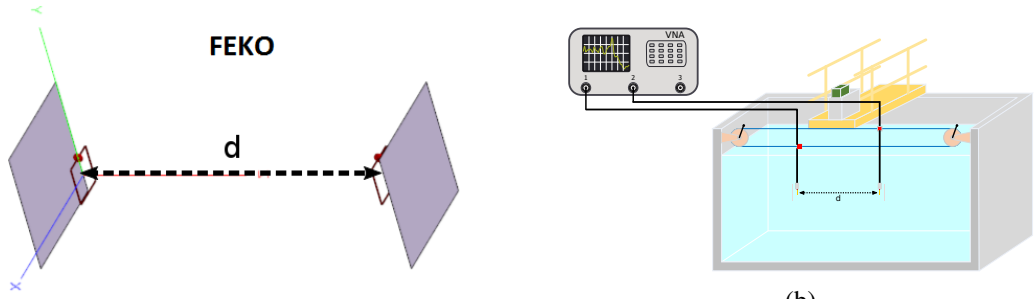

(a) (b)

Figure 5.2: Illustration of the simulated and measured setups used to evaluate the $|S_{21}|$ as a function of distance.

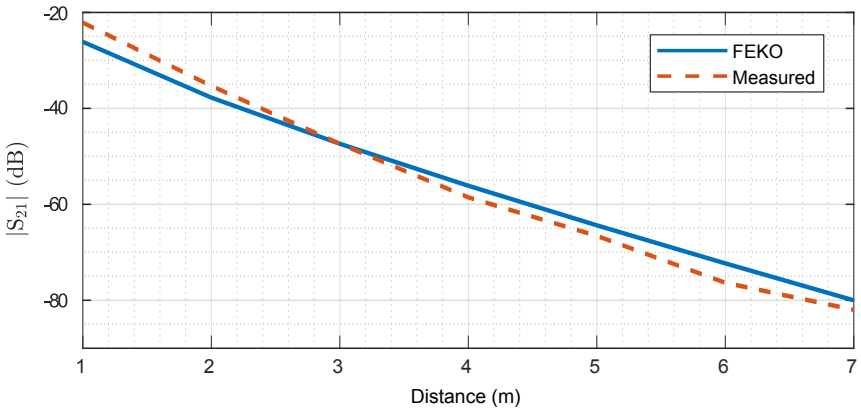

Figure 5.3: Comparison between simulated and measured results for the $|S_{21}|$ parameter as a function of distance.

Knowing that the attenuation at 7 m is around 80 dB, and by using the reference values obtained in laboratory (Section 4.3.2) it is possible to affirm that the communication will be established with success at 7 m and with a data-rate higher than 2 Mbps.

5.2 System Characterization and Results

The setup used to characterize the whole system is illustrated in Figure 5.4. The two Wi-Fi cards were connected to the RF port of the Up-Down Converters and to the computer to setup the network settings. Each IF Port was connected to a square loop antenna that was dived in INESC TEC's pool.

The Bullets M2 have an embedded software to measure the available data-rate, called SpeedTest, but as checked by some reviewers the measurements are not very reliable. To perform the measurement of the data-rate the software *Iperf* was used with the standard configurations. This software has been used in INESC TEC for a long time and has proven to give good results.

Due to lack of time the measurements were done in steps of one meter with just one output power for the bullet, which was 5 dBm. The measurement process was then to distance the antennas for one meter, measure the data-rate, change the distance to two meters, measure the data-rate,

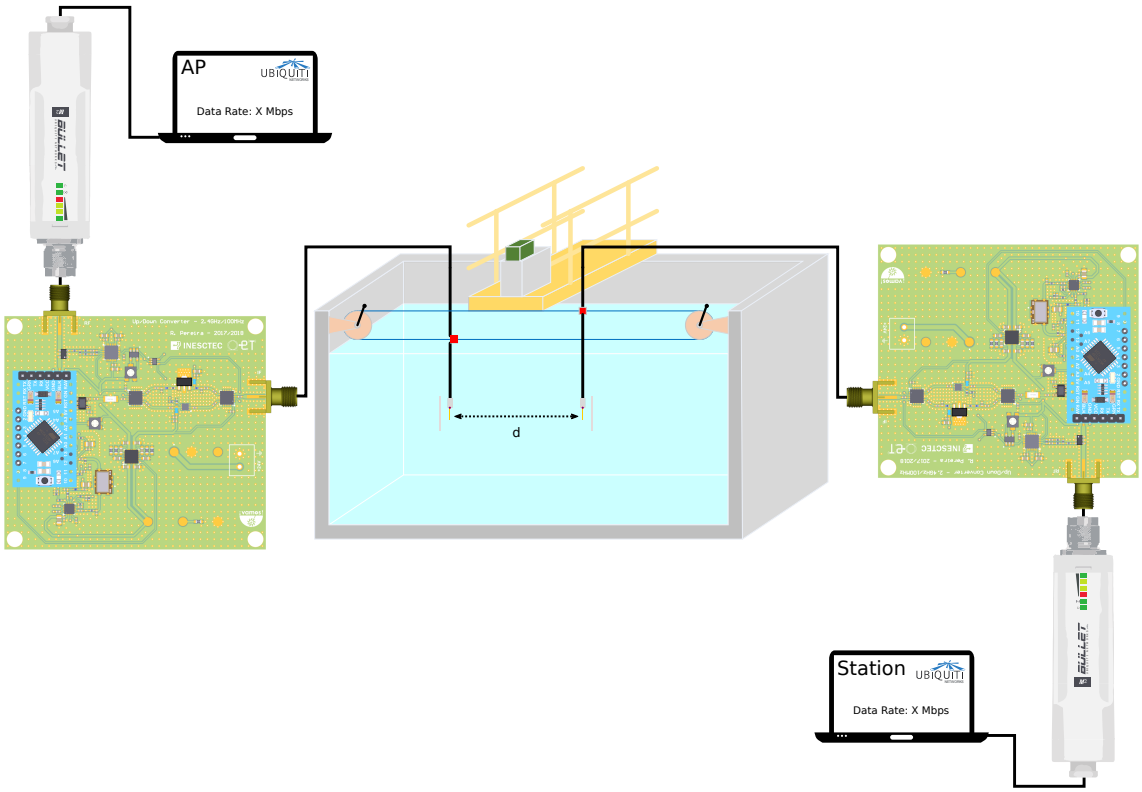

Figure 5.4: Illustration of the setup used to measure the data-rate available as a function of distance.

and so on until a maximum distance of 7 meters which is that maximum distance allowed by the dimensions of the pool. This measurement was done for a channel spectrum width of 5MHz and 8MHz. There was no time to test the performance of the 10 MHz, 15 MHz and 20 MHz channel spectrum width. The advantage of using a lower bandwidth is that it allows an increased number of channels to be used and provides also a more robust link over long distances since the power used is concentrated in lower bandwidth and less noise is captured at the reception.

The obtained results are shown in Figure 5.5 and Table 5.1. It is possible to see that for a distance of one meter the underwater link is not working. This happens because the attenuation is too small and the power of the received signal that goes through the coupler is so high that the coupled power do not allow the power detector and comparator to distinguish between transmitting and receiving. One solution to this is to adjust the potentiometer to have this effect in consideration, or use a coupler with higher directivity.

At 1.2 meters of distance, the underwater link is established around the maximum allowed data-rate for both the bandwidths. The link with a spectral width of 5 MHz keeps its performance until a distance of 5 meters while the one with 8MHz gets weaker with distance. For a distance of 6 meters, the 5MHz link is able to communicate at 4Mbps while the 8MHz link do it at around Mbps. This data-rates are sufficient to allow the transfer of high-quality video (720p/1080p).

At 7 meters, the 8MHz link is not able to hold the communication. The 5MHz link keeps a good performance of 3.15 Mbps which is enough to transmit 480p or even 720p content.

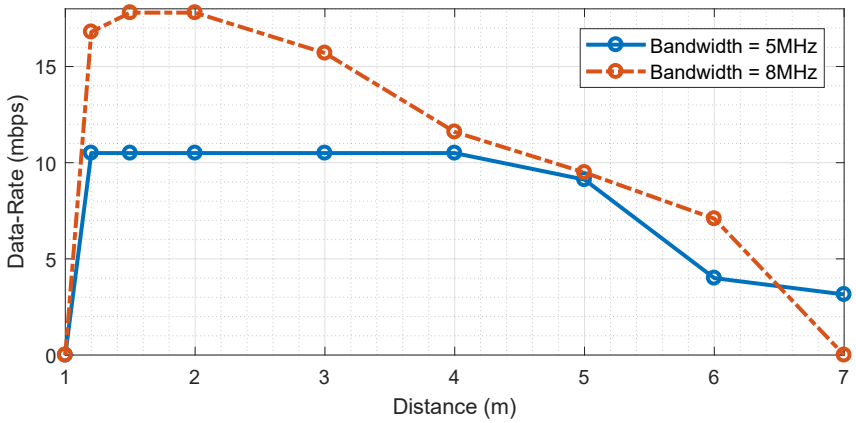

Figure 5.5: Data-Rate as a function of distance for different signal bandwidths.

Table 5.1: Data-Rate as a function of distance for different signal bandwidths.

Distance / Bandwidth	5 MHz	8 MHz
1.2 m	10.5 Mbps	16.8 Mbps
1.5 m	10.5 Mbps	17.8 Mbps
2 m	10.5 Mbps	17.8 Mbps
3 m	10.5 Mbps	15.7 Mbps
4 m	10.5 Mbps	11.6 Mbps
5 m	9.12 Mbps	9.49 Mbps
6 m	4.00 Mbps	7.09 Mbps
7 m	3.15 Mbps	0.00 Mbps

The results showed that it is possible to improve the distance of an underwater Wi-Fi communication by using an Up-Down Converter system. Note that the attenuation for the same water at 2.412 GHz is 291.7176 dB/m (Section 2.3) which would make the communication distance less than half a meter.

To finalize this chapter, a comparative analyses on the performance of the previous version of the Up-Down Converter used in INESC TEC (Figure 5.6a) and the new version that was designed for this master thesis (Figure 5.6b) is shown on Table 5.2. It is verified that the new Up-Down Converter is smaller, cost-effective, is more robust in the sense that it always lock, unlike with the older version that had locking problems due to noise, allows for a higher distance of communication, and the data-rate is higher.

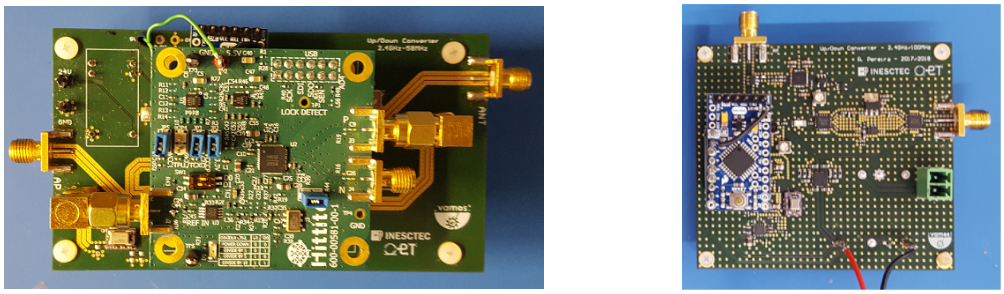

(a) Old Version (b) New Version

Figure 5.6: Illustration of the two different measurement setups for the final Up/Down Conversion board.

Table 5.2: Comparison between the best older version of the Up-Down Converter and the one designed for this master's work.

	Old Version	New Version
Size	110x61x38 mm	76x68x15 mm
Price [1]	$\approx$ 330 €	$\approx$ 120 €
Robustness	Low	High
Maximum Distance / Data-Rate	4.2 m / 2Mbps	7 m (limited by the pool) / 3.15Mbps

[1] Only components.

Chapter 6

Conclusions and Future Work

6.1 Summary of the Performed Work

The fundamental objective of this dissertation focused on the development and implementation of a physical module that could transmit the information transmitted by commercial Wi-Fi cards for longer distances by shifting the signal spectrum to a lower band in the transmitting side, and shifting it back in the receiving side. In order to achieve this objective, the following steps were followed:

- The study about the challenges and restrictions of underwater communications was conducted;
- The analysis on the electric properties of the water, the propagation models of the RF waves for the underwater environment and an analysis on the state of art of antenna design and PCB design were characterized;
- The development of an innovative system level design for an Up/Down Converter board with amplification chain in the transmission and reception with automatic switching, as well as the component selection that better match the performance necessities of the whole system;
- The development, soldering and characterization of self-designed evaluation boards for each of the choosed modules using sophisticated softwares for PCB layout design - Altium Designer - and electromagnetic simulation - Advanced Design System from Keysight, and HFSS from Ansys;
- The design, characterization and validation of the final Up/Down Converter board in a small FR4 laminate with only two layers and with all the designed modules embedded;
- The development of an arduino code and an interface that digitally control the frequency of operation of the PLL and the turn on/off of the up/down converter.
- The characterization of the performance of the final board by means of tests performed first in a laboratory environment and then in a real underwater environment;

- The development of a square-loop antenna with ground plane for underwater communications at 100 MHz with a bandwidth higher than 20 MHz and a directivity of 8.4 dBi.

6.2 Concluded Objectives

- Development of an innovative and low cost Up/Down Converter board from the Wi-Fi 2.4GHz band to 100 MHz with a digital control interface for an Arduino Mini Pro.
- Development of an underwater square-loop antenna with ground plane for 100MHz with a bandwidth higher than 20 MHz and a directivity of 8.4 dBi .
- Communicate through the underwater medium at a distance of 7 m with a data rate of 3.15 mbps.

6.3 Future Work

The major problem in the developed Up/Down Converter board was the noise introduced by the DC-DC converter that was a source of noise for the system and limited the signal-to-noise ratio of the communication link. One possible future work is to find a better solution with less noise and to change the layout to the new solution or to create a small PCB that connect to the already designed layout.

Another problem was to find an amplifier with higher linearity and with high efficiency for the 100 MHz IF frequency to transmit more power into the underwater medium and increase the distance of communication. Design an amplifier with these characteristics and embed it on the board would increase the distance of communication or the data-rate for the same distance. An amplifier with a fast shutdown operation would also increase the energy efficiency of the board and ensure an even better noise isolation between the two tracks of the amplification loop.

Other problem encountered was the temperature that the Up/Down Converter board reached when transmitting at higher power rates. Despite the vias used and the solder mask removal on the sources of heat there was no time to design a heat sink for the board to dissipate that heat generated by the module. Another way is to build a case with a heat conductive material like aluminum and connect it to the external case which will connected to the water. The circuitry can also be soaked in a cooling fluid.

The design of an antenna with higher gain would also increase the communication distance. A smaller antenna for the same frequency would also be a big plus to the mechanics of the whole system.

Finally, the further development of the interface and digital control of the whole board, with a higher control on the performance of the PLL or the development of a common interface between the Bullet M2 and the Up/Down Converter board will also be a big plus for the development of a commercial module.

Appendix A

Arduino Code

```
#include <stdlib.h>
#include <SoftwareSerial.h>
#include <string.h>
#include <math.h>

#define BAUDRATE 9600
#define REFERENCE 10
#define FREQUENCY 2506

// PLL Signal PINs1
uint8_t SCLK = 2;
uint8_t SDI = 3;
uint8_t SDO = 4;
uint8_t SEN = 5;

int count_para_restart=0;
int value=0;

char recString[20] = {'\0'};
int counterRec;
char recChar = 0x00;
int freqRec=0;

// Write value in register
// Inputs:
// reg_add = 6 register address bits
// value1 = [23-16] data bits
// value2 = [15-8] data bits
// value3 = [7-0] data bits
void TxBits(uint32_t reg_add, uint32_t value1, uint32_t value2, uint32_t value3)
{
  uint32_t bitMask = 0x20000000; //Sets bitMask with a 1 in position 29(MSB of data)

  //Sets Initial Write Conditions
  digitalWrite(SCLK,LOW);
  digitalWrite(SDI,LOW);
  digitalWrite(SEN,HIGH);

  int i=0;

  //DATA ARRAY FORMING
  uint32_t value = (value1<<16) | (value2<<8) | (uint32_t)(value3);
  uint32_t data = ((reg_add<<24) | value);

  //TX CYCLE
  for(i=1; i<=32; i++)
  {
    if(i!=1 && i<32)
    {
      if ((data & (bitMask >> (i - 2))) != 0)
      {
        digitalWrite(SDI, HIGH);
      }
      else
      {
        digitalWrite(SDI, LOW);
      }
    }

    //CLOCK
    delayMicroseconds(20);
    digitalWrite(SCLK,HIGH);

    if (i == 32)
    {
      digitalWrite(SEN, LOW);
    }
    delayMicroseconds(20);
    digitalWrite(SCLK,LOW);
  }

  //Returns Pins to Idle State
  digitalWrite(SCLK,LOW);
  digitalWrite(SDI,LOW);
  digitalWrite(SEN,LOW);
}

// Read register value
// Inputs:
// reg = 6 register address bits
// Output:
// data = 24 data bits read
void RxBits(uint32_t reg, uint32_t *data)
{
  int i=0;
  uint32_t bitMask = 0x00000001; //Sets bitMask with a 1 in position 1

  uint32_t dataRead=0;

  //Sets Initial Write Conditions
  digitalWrite(SCLK,LOW);
  digitalWrite(SDI,HIGH);
  digitalWrite(SEN,HIGH);

  //Read Cycle Indication
  delayMicroseconds(20);
  digitalWrite(SCLK,HIGH);
  delayMicroseconds(10);
  digitalWrite(SCLK,LOW);
  delayMicroseconds(10);

  //Adress TX Cycle
```

```
103   for(i=2;i<=7;i++)
104   {
105     if((bitMask<<(7-i)) & reg)
106     {
107       digitalWrite(SDI,HIGH);
108     }
109     else
110     {
111       digitalWrite(SDI,LOW);
112     }
113
114     digitalWrite(SCLK,HIGH);
115     delayMicroseconds(10);
116     digitalWrite(SCLK,LOW);
117     delayMicroseconds(10);
118   }
119
120   //Data RX Cycle
121   for(i=8;i<=31;i++)
122   {
123     digitalWrite(SCLK,HIGH);
124     delayMicroseconds(10);
125     digitalWrite(SCLK,LOW);
126     delayMicroseconds(10);
127
128     if(digitalRead(SDO))
129     {
130       dataRead = dataRead | (bitMask<<(31-i));
131     }
132   }
133
134   //Finishing Cycle
135   digitalWrite(SCLK,HIGH);
136   digitalWrite(SEN,LOW);
137   delayMicroseconds(10);
138   digitalWrite(SCLK,LOW);
139   delayMicroseconds(10);
140   digitalWrite(SDI,LOW);
141
142   data[0] = (dataRead>>16) & (0x000000FF);
143   data[1] = (dataRead>>8) & (0x000000FF);
144   data[2] = (dataRead) & (0x000000FF);
145 }
146
147 float read_freq()
148 {
149   uint32_t Nintaux[3]={0x00,0x00,0x00};
150   uint32_t Nfracaux[3]={0x00,0x00,0x00};
151   long int Nint;
152   float Nfrac;
153   long int Nfracaux2;
154
155   boolean LOCKED = false;
156
157   RxBits(0x02, Nintaux);
158   delayMicroseconds(5);
159   Nint=(Nintaux[2]+Nintaux[1]*256+Nintaux[0]*256*256);
160
161   RxBits(0x04, Nfracaux);
162   delayMicroseconds(5);
163   Nfracaux2=(Nfracaux[2]+Nfracaux[1]*256+Nfracaux
          [0]*256*256);
164   Nfrac=(float)Nfracaux2;
165   for(int i=0;i<24;i++)
166   {
167     Nfrac/=2;
168   }
169   return((Nint+Nfrac)*REFERENCE);
170 }
171
172 // Configure HMC830 PLL+VCO
173 // Input:
174 // freq = PLL frequency in MHz!
175 boolean setPLL(int freq)
176 {
177   int Nint = (int)(freq/REFERENCE);
178   float Nfrac = (float)freq/REFERENCE-Nint;
179   for(int i=0;i<24;i++)
180   {
181     Nfrac*=2;
182   }
183   long int auxNfrac = Nfrac;
184   byte intfreq = byte(Nint);
185   byte floatfreq1 = byte((long int)Nfrac & 0xFF);
186   byte floatfreq2 = byte((long int)Nfrac>>8 & 0xFF);
187   byte floatfreq3 = byte((long int)Nfrac>>16 & 0xFF);
188
189   boolean LOCKED=false;
190
191   uint32_t intfreqRead[3] = {0,0,0};
192   uint32_t floatfreqRead[3] = {0,0,0};
193
194   TxBits(0x00,0x09,0x40,0x75);     // ID Register
195   delayMicroseconds(5);
196
197   TxBits(0x01,0x00,0x00,0x02);     // Reset Register
198   delayMicroseconds(5);
199
200   TxBits(0x02,0x00,0x00,0x01);     // Reference Divider
          Register
201   delayMicroseconds(5);
202
203   TxBits(0x03,0x00,0x00,intfreq);        // Frequency
          Register Integer Part
204   delayMicroseconds(5);
205
206   TxBits(0x04,0x00,0x00,0xF2);        // Frequency
          Register Frac Part
207   delayMicroseconds(5);
208
209   TxBits(0x05,0x00,0x00,0x90);     // SD Seed Modulator
          Register
210   delayMicroseconds(5);
211
212   TxBits(0x05,0x00,0x0E,0x98);     // SD Seed Modulator
          Register
213   delayMicroseconds(5);
214
215   TxBits(0x05,0x00,0x4D,0x38);     // SD Seed Modulator
          Register
216   delayMicroseconds(5);
217
218   TxBits(0x05,0x00,0x00,0x00);     // SD Seed Modulator
          Register
219   delayMicroseconds(5);
220
221   TxBits(0x06,0x03,0x0F,0x4A);     // SD CFG Register
222   delayMicroseconds(5);
223
224   TxBits(0x07,0x00,0x02,0xCD);     // Lock Detect/Cycle
          Slip Prevention Register
225   delayMicroseconds(5);
226
227   TxBits(0x08,0xC1,0xBE,0xFF);     // Analog Enable
          Register
228   delayMicroseconds(5);
229
230   TxBits(0x09,0x30,0xED,0x5A);     // Charge Pump Register
231   delayMicroseconds(5);
232
233   TxBits(0x0A,0x00,0x20,0x06);     // Charge Pump Internal
          Amplifier Register
234   delayMicroseconds(5);
235
236   TxBits(0x0B,0x0F,0x80,0x61);     // Phase Frequency
          Detector Register
237   delayMicroseconds(5);
238
239   TxBits(0x0C,0x00,0x00,0x00);     // VCO SPI Register
240   delayMicroseconds(5);
241
242   TxBits(0x0D,0x00,0x00,0x00);     // GPO SPI Divider
          Register
243   delayMicroseconds(5);
```

```
244
245   TxBits(0x0E,0x00,0x00,0x00);
246   delayMicroseconds(5);
247
248   TxBits(0x0F,0x00,0x00,0x81);     // Lock Detect State
          Register
249   //  TxBits(0x0F,0x00,0x00,0xDF);     // Lock Detect
          State Register
250
251   delayMicroseconds(5);
252
253   TxBits(0x10,0x00,0x00,0x20);
254   delayMicroseconds(5);
255
256   TxBits(0x11,0x07,0xFF,0xFF);
257   delayMicroseconds(5);
258
259   TxBits(0x12,0x00,0x00,0x00);
260   delayMicroseconds(5);
261
262   TxBits(0x13,0x00,0x12,0x59);
263   delayMicroseconds(5);
264
265   TxBits(0x14,0x00,0x00,0x00);
266   delayMicroseconds(5);
267
268   TxBits(0x15,0x00,0x00,0x00);
269   delayMicroseconds(5);
270
271   TxBits(0x16,0x00,0x00,0x00);
272   delayMicroseconds(5);
273
274   TxBits(0x17,0x00,0x00,0x00);
275   delayMicroseconds(5);
276
277   TxBits(0x18,0x00,0x00,0x00);
278   delayMicroseconds(5);
279
280   TxBits(0x19,0x00,0x00,0x00);
281   delayMicroseconds(5);
282
283   TxBits(0x1A,0x00,0x00,0x00);
284   delayMicroseconds(5);
285
286   TxBits(0x1B,0x00,0x00,0x00);
287   delayMicroseconds(5);
288
289   TxBits(0x1C,0x00,0x00,0x00);
290   delayMicroseconds(5);
291
292   TxBits(0x1D,0x00,0x00,0x00);
293   delayMicroseconds(5);
294
295   TxBits(0x1E,0x00,0x00,0x00);
296   delayMicroseconds(5);
297
298   TxBits(0x1F,0x00,0x00,0x00);
299   delayMicroseconds(5);
300
301   TxBits(0x04,floatfreq3,floatfreq2,floatfreq1);     //
          Frequency Register Fractional Part
302   delayMicroseconds(5);
303
304   RxBits(0x03,intfreqRead);
305   delayMicroseconds(200);
306
307   RxBits(0x04,floatfreqRead);
308   delayMicroseconds(200);
309
310   int i;
311   for(i=0;i<10;i++)
312   {
313     LOCKED = digitalRead(SDO);
314     delay(500);
315     if(LOCKED==true)
316       break;
317     Serial.println(".");
318   }
319
320   if(LOCKED)
321   {
322     return true;
323   }
324   else
325   {
326     return false;
327   }
328 }
329
330 void setup()
331 {
332   //digitalWrite(REG,HIGH);
333   Serial.begin(BAUDRATE);  // Serial port initialization
334   while (!Serial);
335   Serial.flush();
336
337   // PLL + VCO initialization
338   pinMode(SCLK, OUTPUT);          // Define SCLK as a
          output
339   pinMode((uint8_t) 2, INPUT);          // Define SCLK as a
          output
340   pinMode(SDI, OUTPUT);           // Define SDI as a output
341   pinMode(SDO, INPUT);            // Define SDO as a input
342   pinMode(SEN, OUTPUT);           // Define SEN as a output
343
344   digitalWrite(SCLK,LOW);         // SCLK idle state = LOW
345   digitalWrite(SEN,LOW);          // SEN idle state = LOW
346   digitalWrite(SDI,LOW);          // SDI idle state = LOW
347
348   Serial.println("Inicializating␣VCO...");
349   if(setPLL((int)FREQUENCY))          // Frequency in MHz
350   {
351     Serial.println("VCO␣INITIALIZED!\n\n");
352   }
353   else
354     Serial.println("UNABLE␣TO␣INITIALIZE␣VCO\n");
355 }
356
357 void loop()
358 {
359   memset(recString,0,sizeof(recString)); //Clears
          received string
360
361   counterRec=0;
362
363   if(Serial.available()>0)
364   {
365     Serial.println("Bom␣digito!\n\n");
366     while((recChar = Serial.read())!=-1 && counterRec<19)
367     {
368       recString[counterRec] = recChar;
369       counterRec++;
370       delay(ceil((float)2000*8/BAUDRATE));
371     }
372     value=atoi(recString);
373     if(value>=2412 && value <=2474)
374     {
375       setPLL(value);
376     }
377   }
378 }
```

Appendix B

Gerbers and Schematics

B.1 Arduino Mini Pro

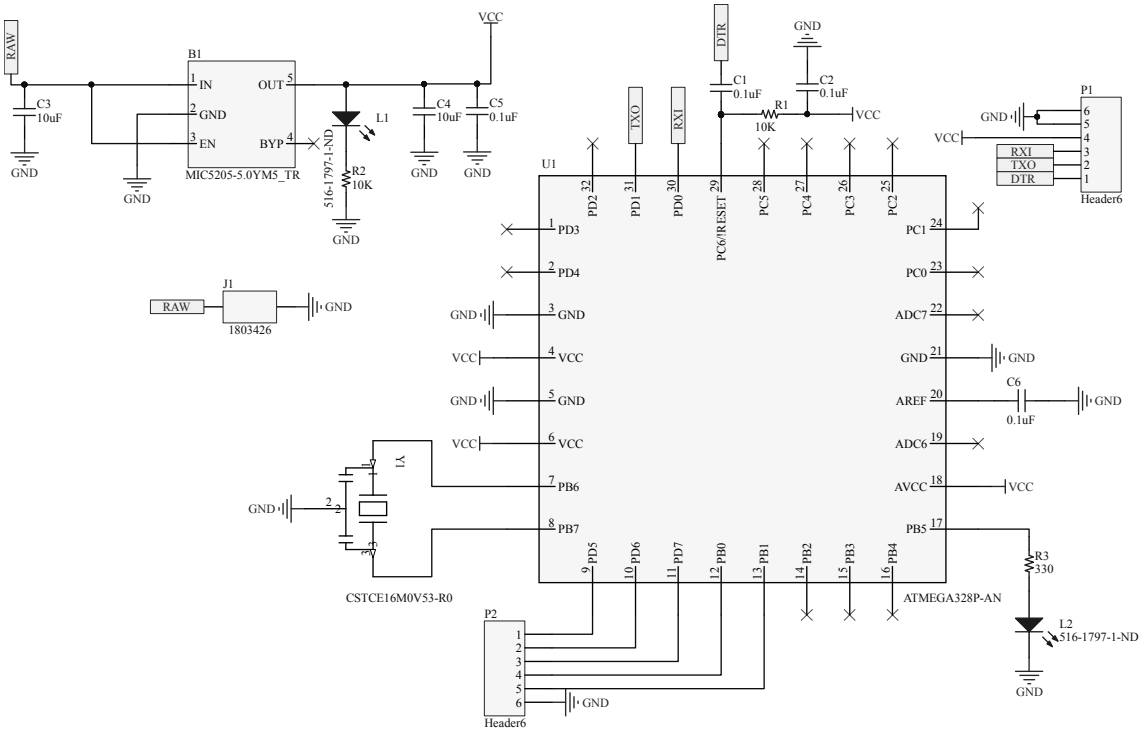

Figure B.1: Schematic for the designed Arduino Mini Pro board.

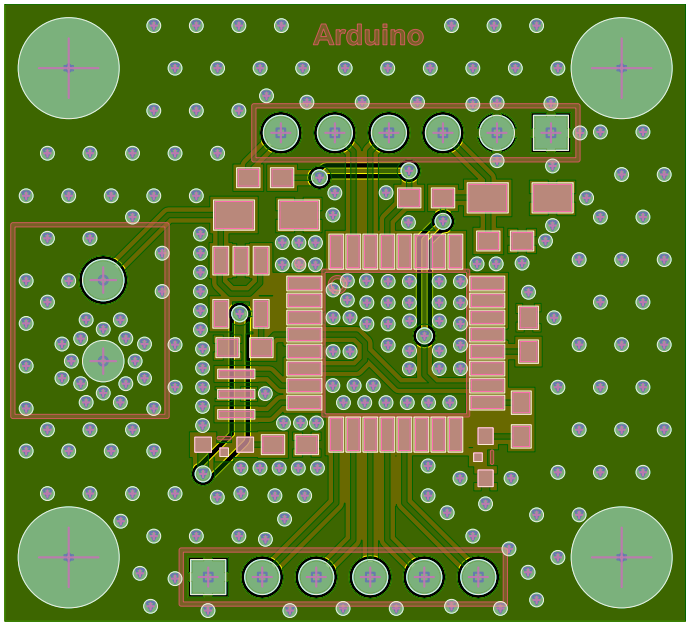

Figure B.2: View of the Gerber files designed for the Arduino Mini Pro.

B.2 Coupler - D17IA+

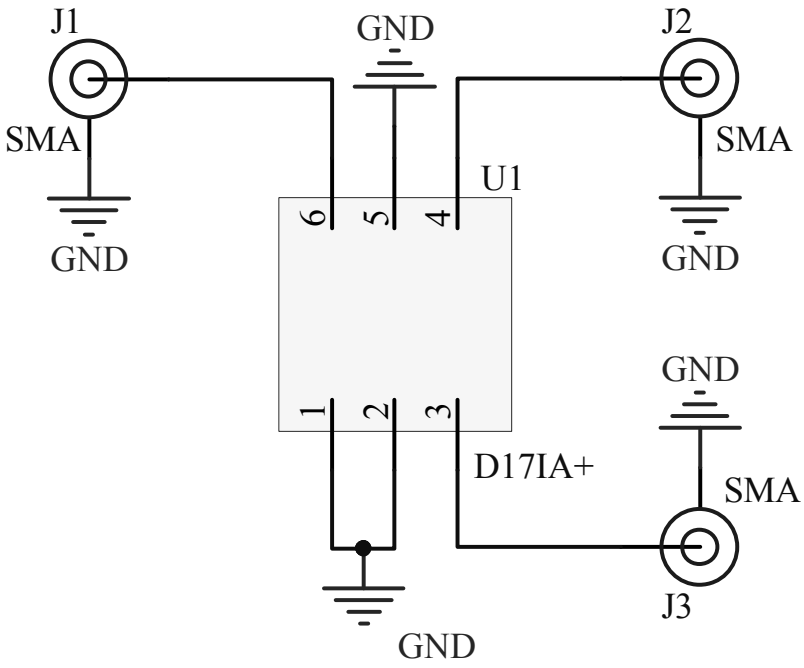

Figure B.3: Schematic for the designed Coupler D17IA+ board.

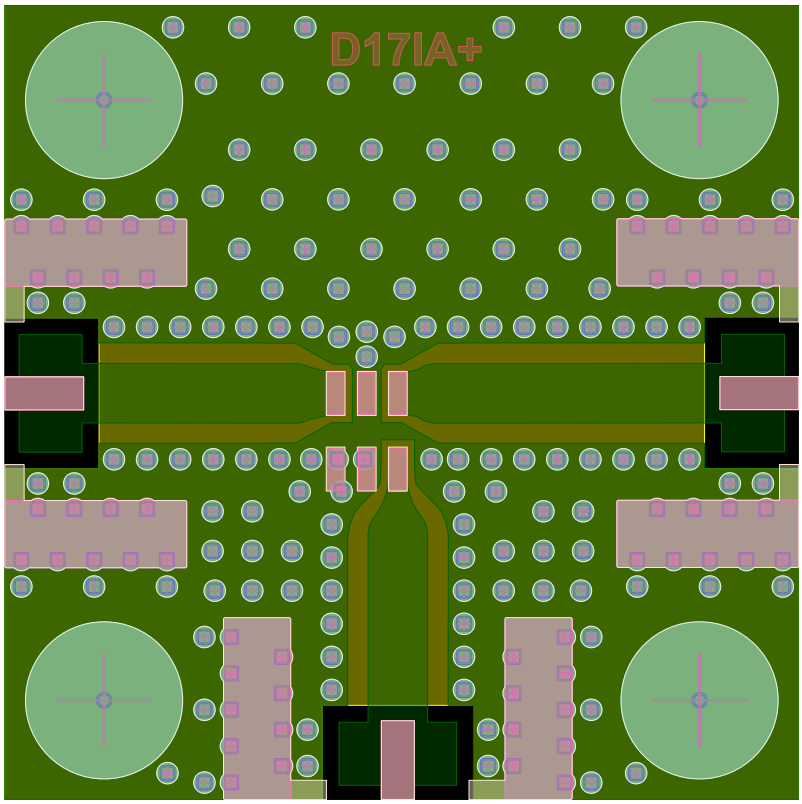

Figure B.4: View of the Gerber files designed for the Coupler D17IA+ board.

B.3 Detector - Comparator

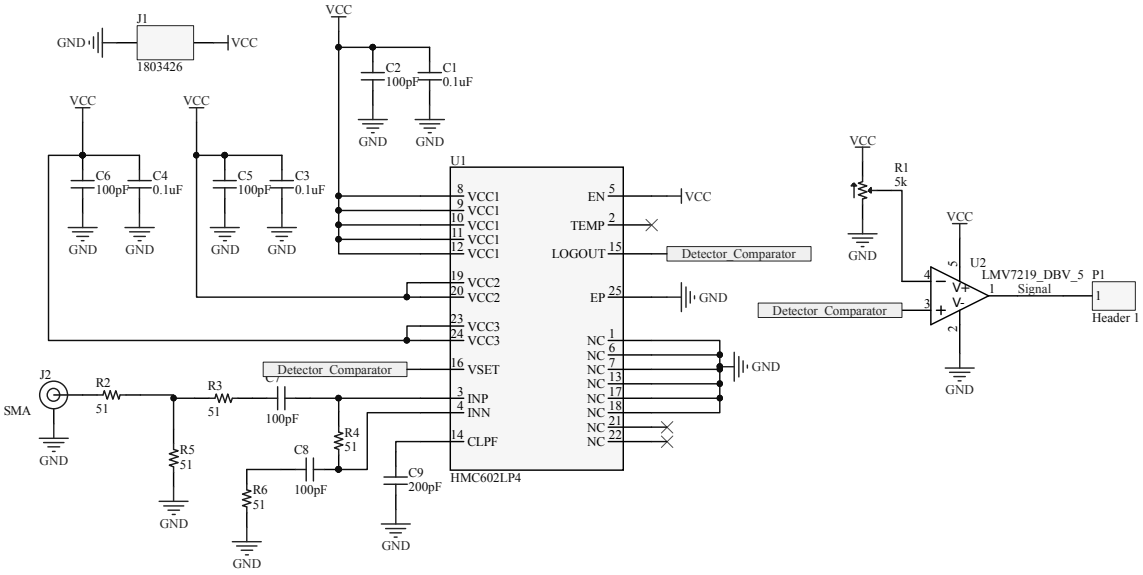

Figure B.5: Schematic for the designed Detector HMC602 and Comparator LMV7219 board.

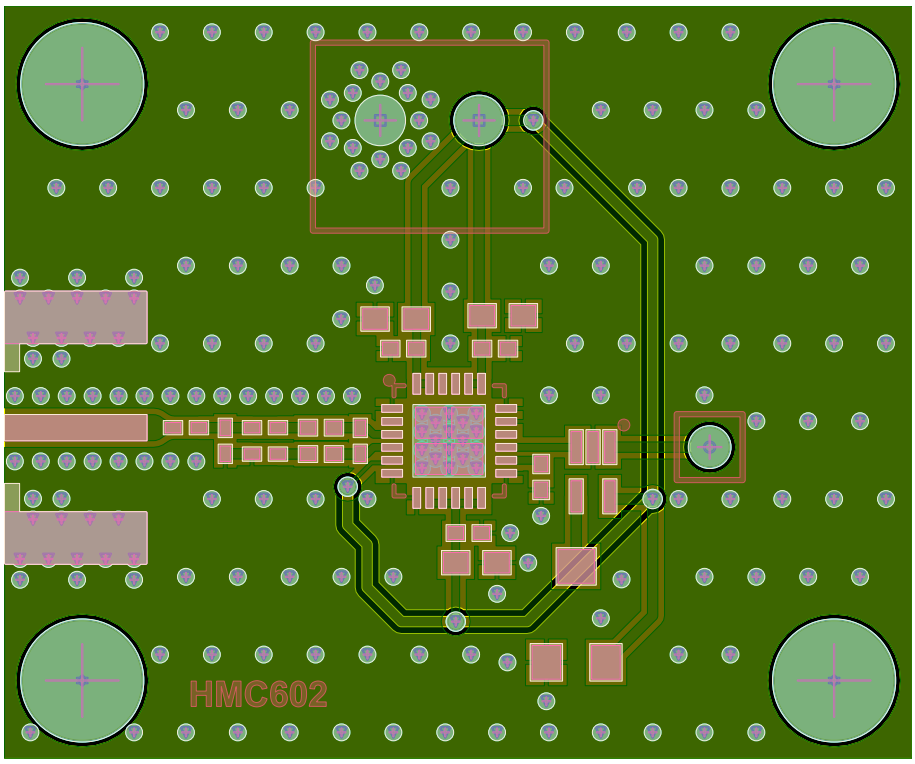

Figure B.6: View of the Gerber files designed for the Detector HMC602 and Comparator LMV7219 board.

B.4 Band-Pass Filter

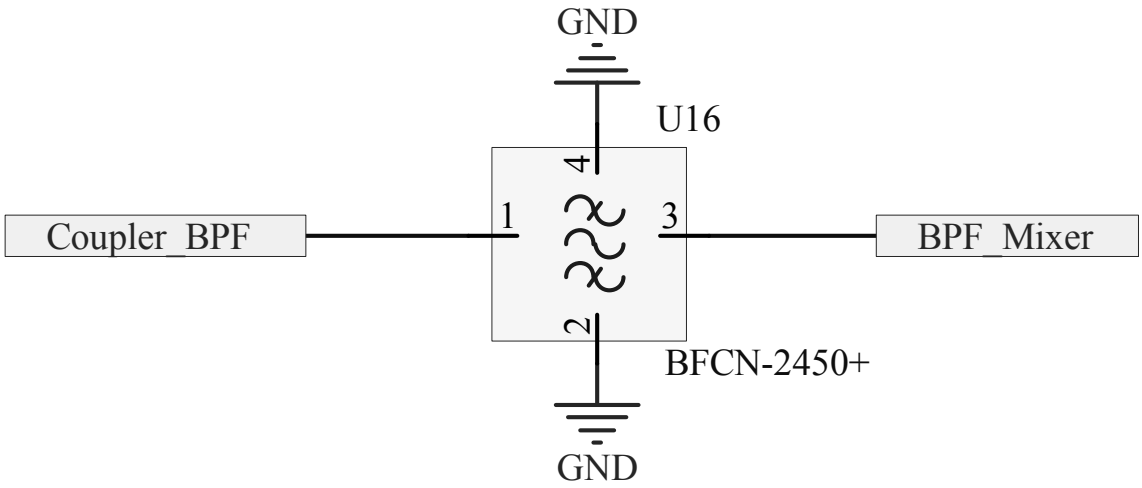

Figure B.7: Schematic for the designed Band-Pass Filter BFCN-2450+ board.

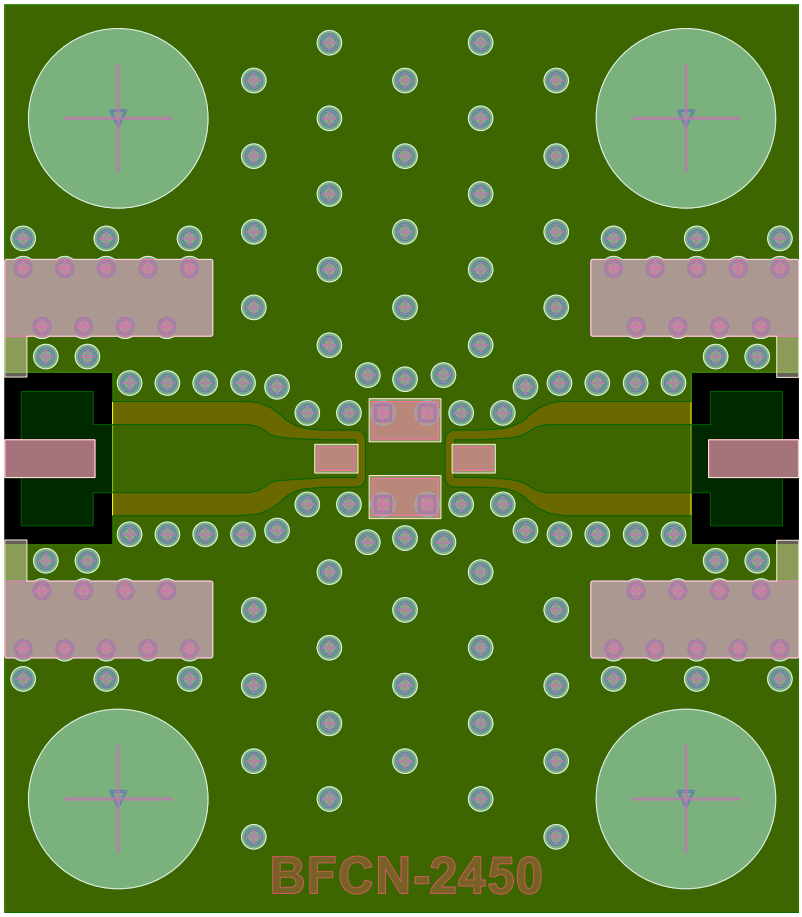

Figure B.8: View of the Gerber files designed for the Band-Pass Filter BFCN-2450+ board.

B.5 Low-Pass Filter

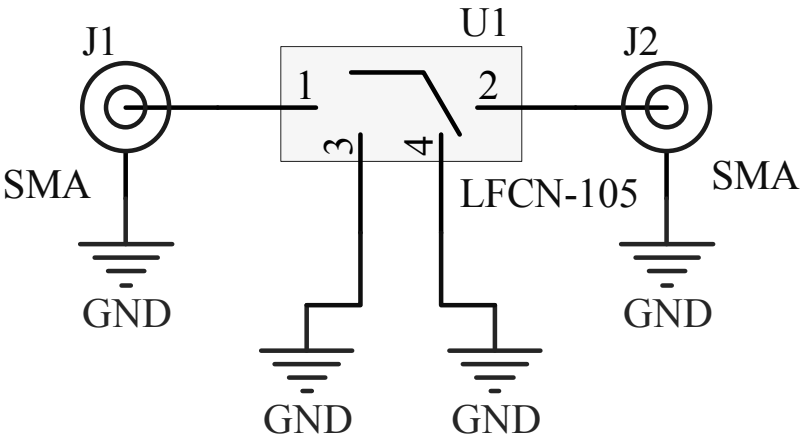

Figure B.9: Schematic for the designed Low-Pass Filter LFCN-105 board.

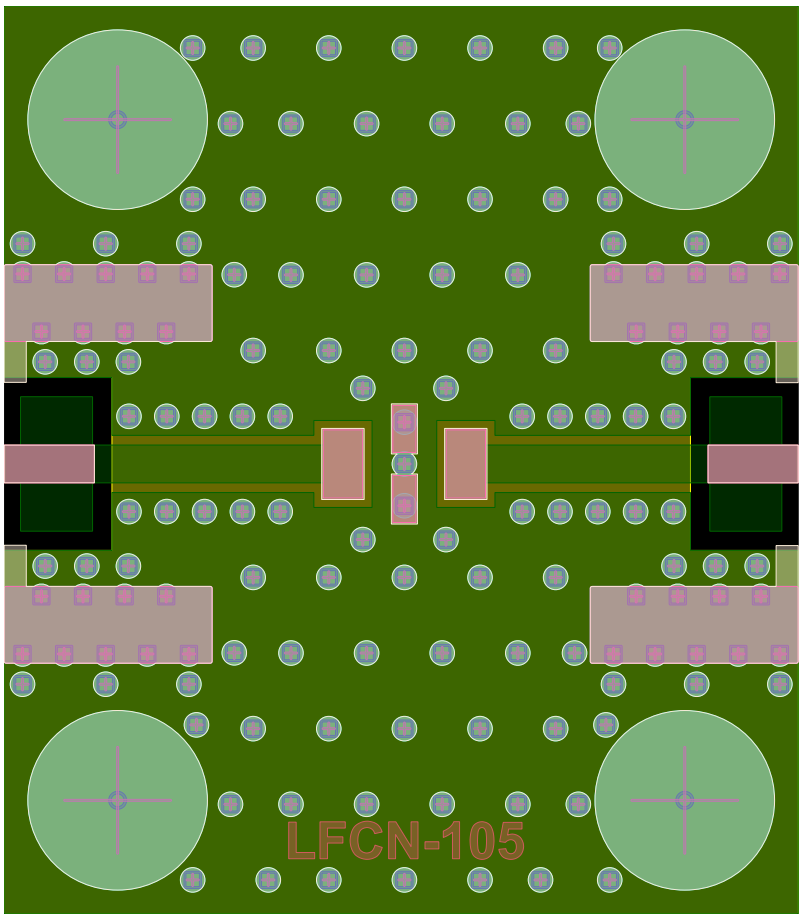

Figure B.10: View of the Gerber files designed for the Low-Pass Filter LFCN-105 board.

B.6 Gain Block

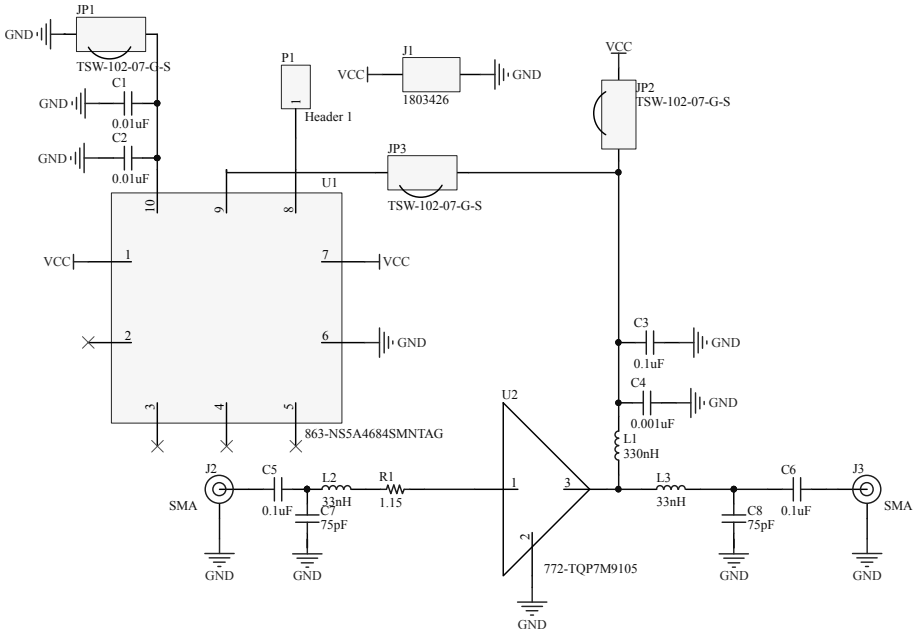

Figure B.11: Schematic for the designed Gain Block TQP7M9105 board.

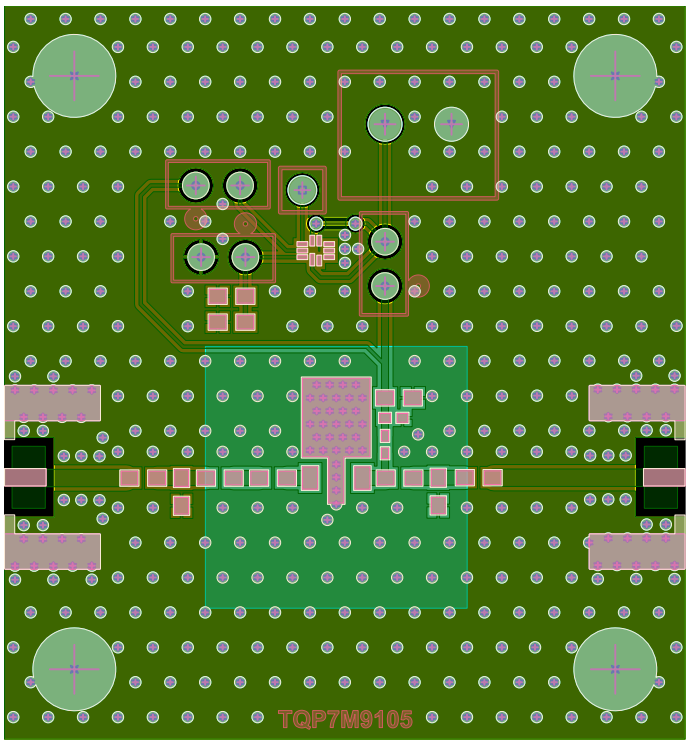

Figure B.12: View of the Gerber files designed for the Gain Block TQP7M9105 board

B.7 Inverter

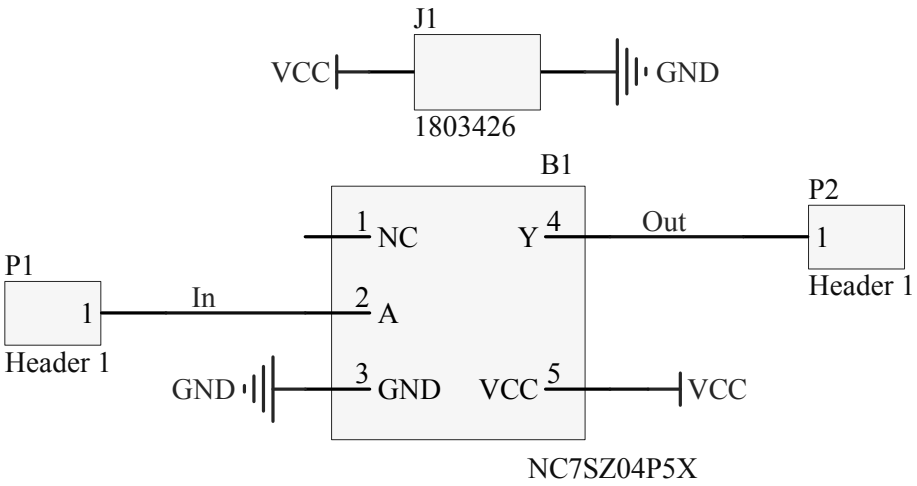

Figure B.13: Schematic for the designed Inverter NC7SZ04P5X board.

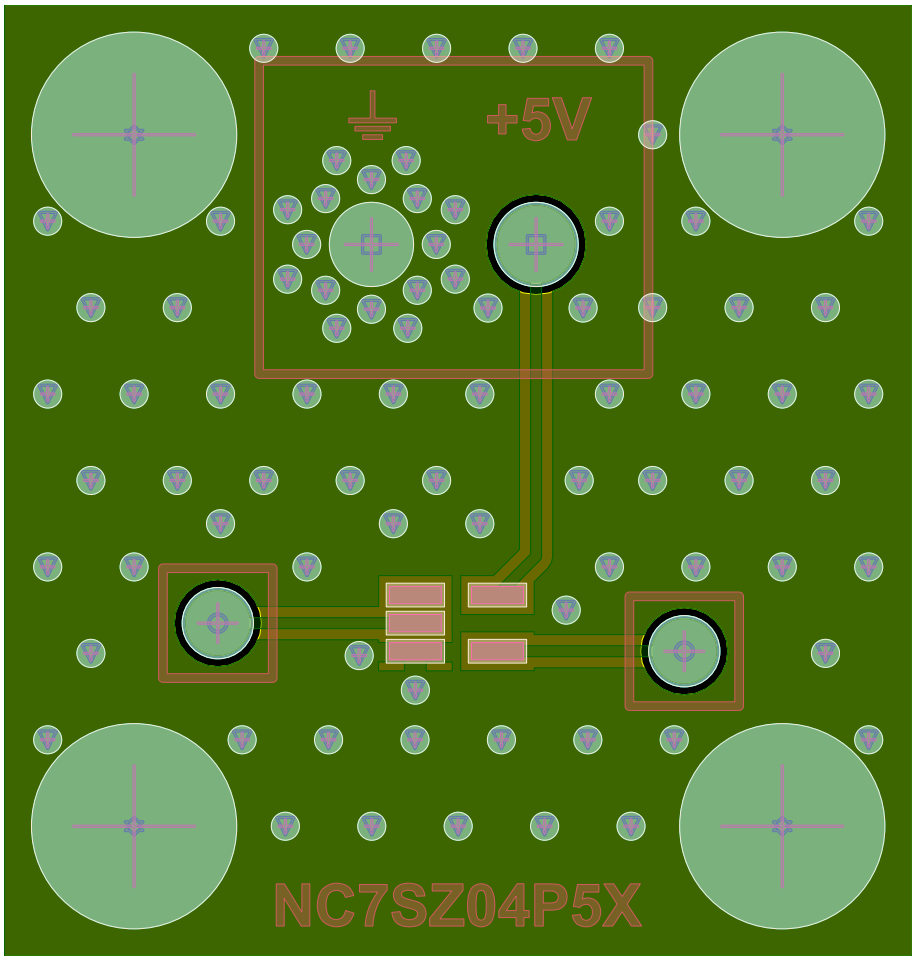

Figure B.14: View of the Gerber files designed for the Inverter NC7SZ04P5X board

B.8 Low Noise Amplifier

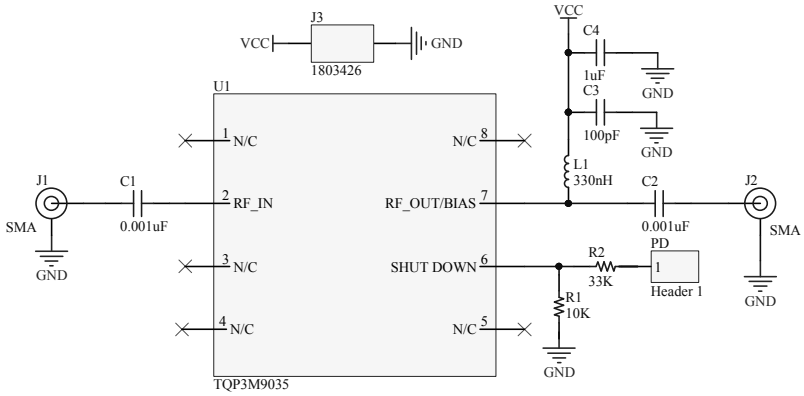

Figure B.15: Schematic for the designed LNA TQP3M9035 board.

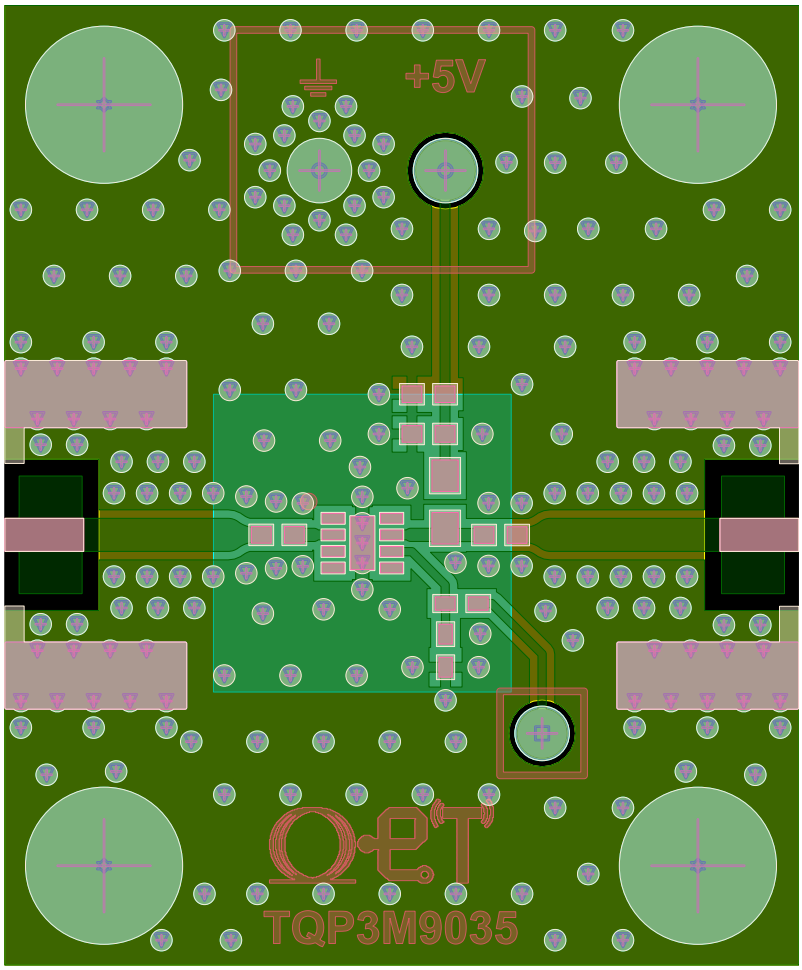

Figure B.16: View of the Gerber files designed for the LNA TQP3M9035 board.

B.9 Mixer

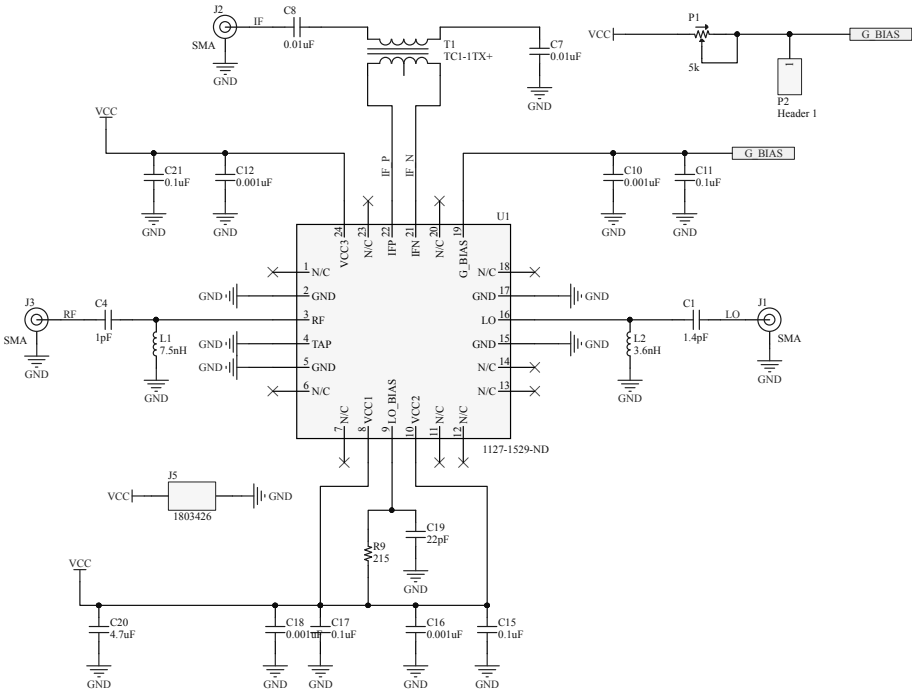

Figure B.17: Schematic for the designed Mixer HMC689 board.

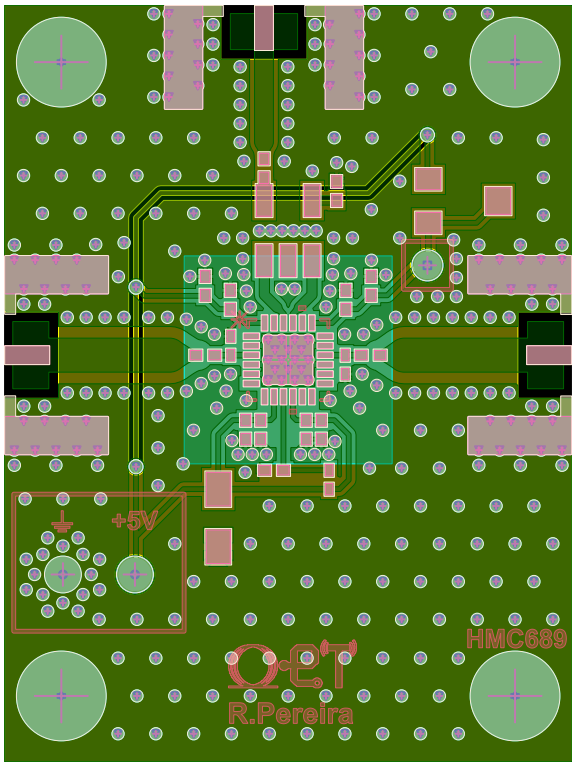

Figure B.18: View of the Gerber files designed for the Mixer HMC689 board.

B.10 PLL

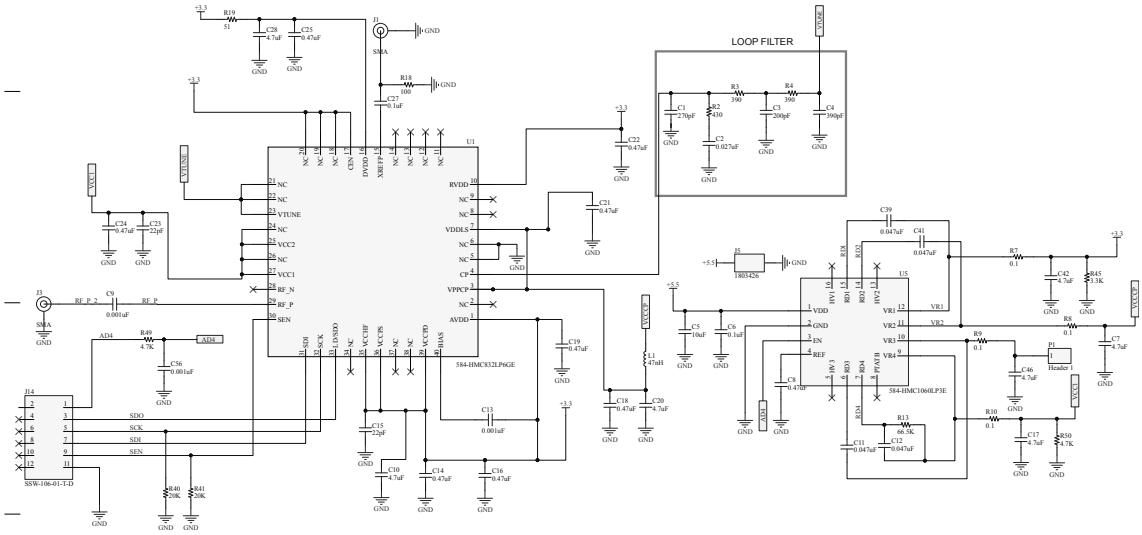

Figure B.19: Schematic for the designed PLL HMC832 board.

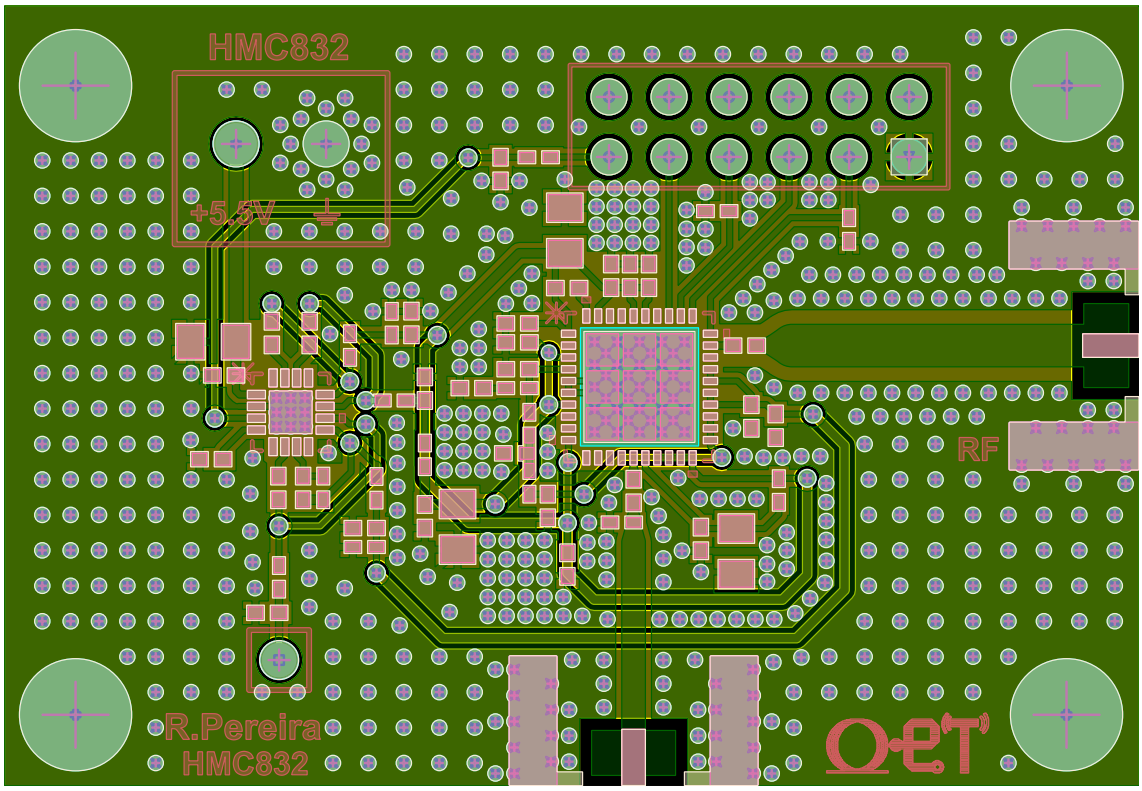

Figure B.20: View of the Gerber files designed for the PLL HMC832 board.

B.11 Switch

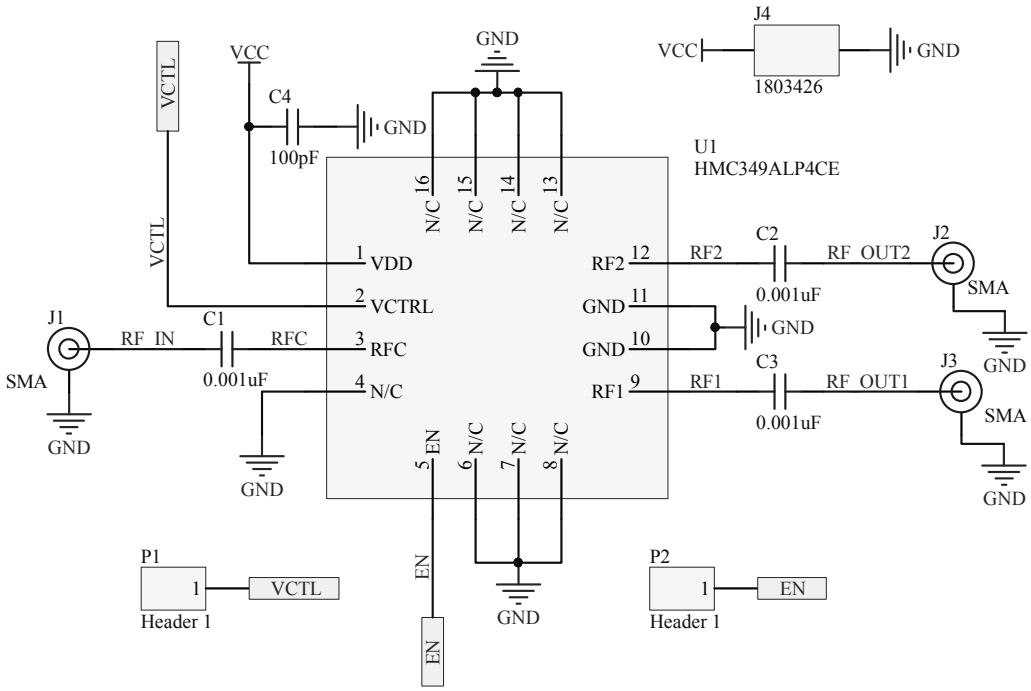

Figure B.21: Schematic for the designed Power Supply HMC349ALP4CE board.

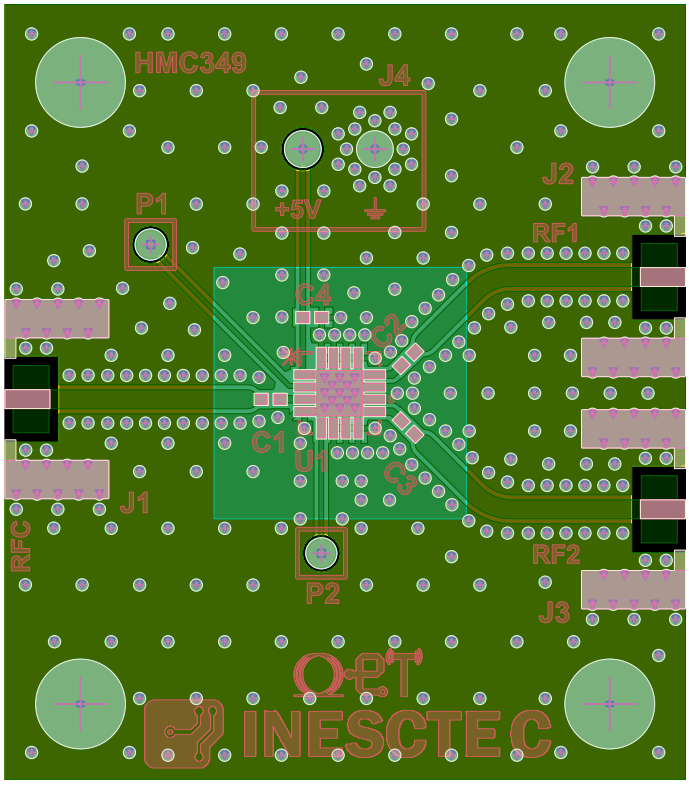

Figure B.22: View of the Gerber files designed for the Switch HMC349ALP4CE board.

B.12 Power Supply

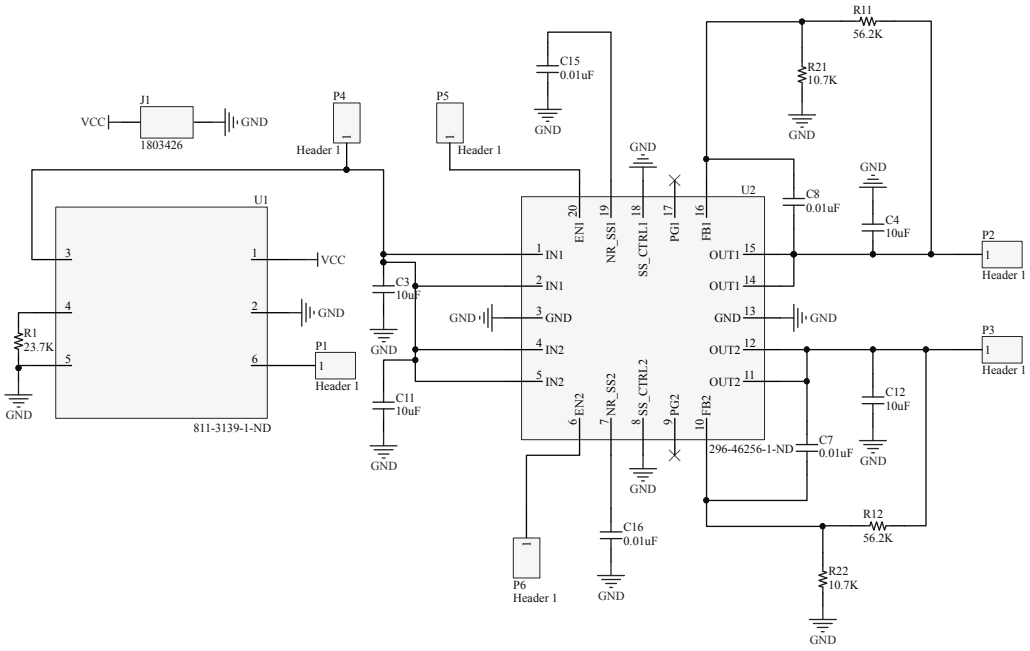

Figure B.23: Schematic for the designed Power Supply TPS7A8901RTJR and UEI15-050-Q12 board.

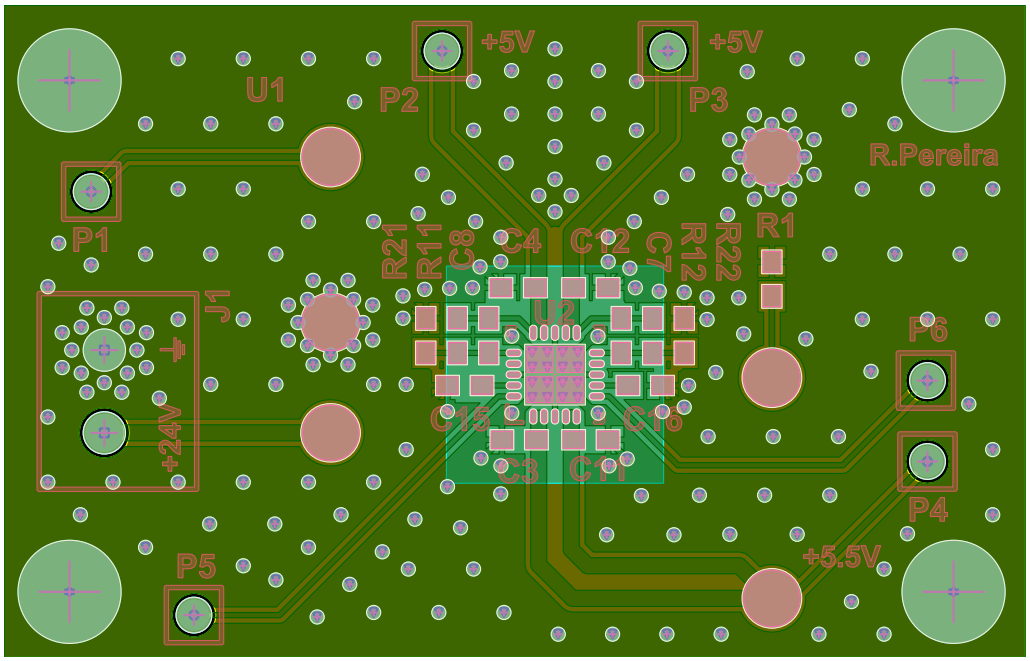

Figure B.24: View of the Gerber files designed for the Power Supply TPS7A8901RTJR and UEI15-050-Q12 board.

Bibliography

[1] F. Marki and C. Marki, "Mixer basics primer," *Marki Microwave, Morgan Hill, USA*, 2010.

[2] J. B. Hasted, *Aqueous dielectrics*. Chapman and Hall, 1973.

[3] "International trade in raw materials - statistics explained." `http://ec.europa.eu/eurostat/statistics-explained/index.php/International_trade_in_raw_materials`. (Accessed on 10/02/2017).

[4] "Raw materials - european commission." `https://ec.europa.eu/programmes/horizon2020/en/area/raw-materials#Article`. (Accessed on 10/03/2017).

[5] "Can deep-sea mining avoid the environmental mistakes of mining on land? | the guardian." `https://www.theguardian.com/sustainable-business/2017/jun/28/deep-sea-mining-environmental-mistakes`. (Accessed on 10/03/2017).

[6] C. Sword, B. Bodo, S. Kapusniak, F. Bosman, J. Rainbird, and E. Silva, "!vamos! (viable alternative mine operating system)-a 'horizon 2020' project," in *EGU General Assembly Conference Abstracts*, vol. 19, p. 348, 2017.

[7] X. Che, I. Wells, G. Dickers, P. Kear, and X. Gong, "Re-evaluation of rf electromagnetic communication in underwater sensor networks," *IEEE Communications Magazine*, vol. 48, no. 12, pp. 143–151, 2010.

[8] A. B. B. DANIEL BK, "The state of art in underwater acoustic telemetry," *IEEE Journal of Oceanic Engineering*, pp. 4–27.

[9] Y. R. Zheng, "Channel estimation and phase-correction for robust underwater acoustic communications," in *Military Communications Conference, 2007. MILCOM 2007. IEEE*, pp. 1–6, IEEE, 2007.

[10] M. Lanzagorta, "Underwater communications," *Synthesis Lectures on Communications*, vol. 5, no. 2, pp. 1–129, 2012.

[11] C. M. Gussen, P. S. Diniz, M. L. Campos, W. A. Martins, F. M. Costa, and J. N. Gois, "A survey of underwater wireless communication technologies," *Journal of Communication and Information Systems*, vol. 31, no. 1, 2016.

[12] H. Kaushal and G. Kaddoum, "Underwater optical wireless communication," *IEEE Access*, vol. 4, pp. 1518–1547, 2016.

[13] R. K. Moore, "Radio communication in the sea," *IEEE spectrum*, vol. 4, no. 11, pp. 42–51, 1967.

[14] F. T. Ulaby, E. Michielssen, U. Ravaioli, W. Hayt, and J. Buck, "Fundamentals of applied electromagnetics, isbn: 978-0-13-213931-1," *Instructor*, vol. 201409, 2014.

[15] G. Hattab, M. El-Tarhuni, M. Al-Ali, T. Joudeh, and N. Qaddoumi, "An underwater wireless sensor network with realistic radio frequency path loss model," *International Journal of Distributed Sensor Networks*, vol. 2013, 2013.

[16] I. Bogie, "Conduction and magnetic signalling in the sea a background review," *Radio and Electronic Engineer*, vol. 42, no. 10, pp. 447–452, 1972.

[17] M. N. Sadiku, *Elements of electromagnetics*. Oxford university press, 2014.

[18] W. Ellison, A. Balana, G. Delbos, K. Lamkaouchi, L. Eymard, C. Guillou, and C. Prigent, "New permittivity measurements of seawater," *Radio science*, vol. 33, no. 3, pp. 639–648, 1998.

[19] S. Jiang and S. Georgakopoulos, "Electromagnetic wave propagation into fresh water," *Journal of Electromagnetic Analysis and Applications*, vol. 3, no. 07, p. 261, 2011.

[20] L. Klein and C. Swift, "An improved model for the dielectric constant of sea water at microwave frequencies," *IEEE Journal of Oceanic Engineering*, vol. 2, no. 1, pp. 104–111, 1977.

[21] "Antenna design." `http://www.antenna-theory.com/design/antenna.php`. (Accessed on 11/10/2017).

[22] C. A. Balanis, *Antenna Theory: Analysis and Design*. John Wiley & Sons, 2016.

[23] A. Garcia Miquel, "Uwb antenna design for underwater communications," 2009.

[24] "Rf design guidelines: Pcb layout and circuit optimization." `https://www.semtech.com/uploads/documents/rf_design_guidelines_semtech.pdf`. (Accessed on 06/07/2018).

[25] "Antenna design and rf layout guidelines." `http://www.cypress.com/file/136236/download`. (Accessed on 06/15/2018).

[26] "General layout guidelines for rf and mixed-signal pcbs - tutorial - maxim." `https://www.maximintegrated.com/en/app-notes/index.mvp/id/5100`. (Accessed on 06/17/2018).

[27] D. M. Pozar, “Microwave engineering,” 2012.

[28] O. Aboderin, L. Pessoa, and H. Salgado, “Analysis of loop antenna with ground plane for underwater communications,” in *OCEANS 2017-Aberdeen*, pp. 1–6, IEEE, 2017.

[29] “Directivity and vswr measurements.” `https://www.markimicrowave.com/assets/appnotes/directivity_and_vswr_measurements.pdf`. (Accessed on 05/18/2018).

[30] “Local oscillator phase noise and its effect on receiver performance.” `http://www.rfcafe.com/references/articles/wj-tech-notes/effect-LO-phase-noise-receiver-sensitivity-v8-6.pdf`. (Accessed on 05/19/2018).